



University of Trento
Department of Physics

Doctoral School in Physics, XXV cycle

Phd Thesis

Silicon Concentrator Solar Cells: Fabrication, Characterization and Development of Innovative Designs.

Candidate:
Giovanni Paternoster

Advisor:
Dr. Lorenza Ferrario

28 March 2013

*“There does not exist a category of science to
which one can give the name applied science.
There are science and the applications of science,
bound together as the fruit of the tree which bears it.”*
Louis Pasteur

Contents

1	Introduction	5
1.1	Thesis motivation	5
1.2	Thesis outline	6
1.3	Overview of silicon concentrator cells	8
2	Basics of concentrator silicon solar cells	11
2.1	Origin of the photovoltaic action	11
2.2	Carriers in semiconductor	12
2.2.1	Semiconductor at equilibrium	12
2.2.2	Semiconductor under light bias	13
2.3	The solar spectrum	15
2.4	Generation and recombination processes in semiconductors	16
2.4.1	Photogeneration	17
2.4.2	Recombination in low-level injection	19
2.4.3	Carrier lifetime and diffusion length	22
2.5	Current-voltage characteristics of a solar cell in low-level injection	24
2.5.1	Basics equations of p-n junction	24
2.5.2	Solar cell in the dark	25
2.5.3	Cell under illumination	25
2.6	Solar cell in high-level injection	26
2.6.1	Recombination under high-level injection	26
2.6.2	Current-Voltage curve under high-injection	29
2.6.3	Cell parameters under concentrated light	30
2.6.4	Mobility and band gap under high-level injection	34

3	Fabrication technology of concentrator solar cells	37
3.1	Device structure and technology	37
3.2	Fabrication process	41
3.3	Lifetime characterization of materials and fabrication process	48
3.3.1	Experimental methods	49
3.3.2	Experimental results	51
3.4	Texturing optimization and characterization	52
3.4.1	Texturing process optimization	53
3.4.2	Passivating properties of textured surfaces	55
3.4.3	Textured solar cell fabrication	56
3.5	Fabrication technology of deep-grooved contacts and holes	58
3.5.1	Silicon deep etch technology	60
4	Modeling and simulation of concentrator Si solar cells	63
4.1	Series resistance in concentrator Si solar cells	64
4.2	Co-optimization of the emitter and of the metal grid using a quasi-analytical approach	68
4.2.1	Co-optimization model	69
4.2.2	Modeling of the resistance losses	73
4.2.3	Conversion efficiency maximization	75
4.2.4	Design rules for the emitter and the metal grid	75
4.2.5	Quantitative analysis of the resistance losses	77
4.3	Electrical and Optical Simulations	78
4.3.1	Simulation process	79
4.3.2	Simulation parameters and models	80
4.3.3	First simulations results	82
4.3.4	Determination of the injection level and of the recombination mechanisms	82
4.4	Simulation trends	84
4.4.1	Finger spacing optimization	85
4.4.2	Back surface field	86
4.4.3	Substrate thickness and doping	89
4.4.4	DEPC solar cells	94
5	Cell testing methods	99
5.1	Preliminary electrical characterization	99
5.2	Packaging for testing	101
5.3	Cell characterization methods under 1 sun	104

5.3.1	Spectral mismatch	105
5.3.2	Measurement errors at 1 sun	105
5.4	Characterization methods under concentrated light	106
5.4.1	Measurement setup	106
5.4.2	Temperature control	108
5.4.3	Efficiency-concentration curves	108
5.4.4	Correction for the sub- and super-linear short circuit current effect	109
5.4.5	Measurement error	111
5.5	Determination of the series resistance	111
5.5.1	Experimental methods	112
6	Experimental characterization	115
6.1	Cell characterization under concentrated light	115
6.2	Front metal grid and surface texturing	117
6.2.1	Metal grid and finger spacing	118
6.2.2	Surface texturing	121
6.3	BSF boron doping	122
6.3.1	Light induced decay	123
6.4	Substrate resistivity	128
6.5	Characterization of DEPC solar cells	131
6.6	23% efficient concentrator solar cells	135
7	Back-contact vertical junction Si solar cells for concentrating pho- tovoltaics	137
7.1	Purpose and scientific relevance	138
7.2	Fabrication process	138
7.3	Cell modeling and Simulations	141
7.4	Experimental results	143
	Conclusions	149
	Bibliography	152

CHAPTER 1

Introduction

1.1 Thesis motivation

Today's photovoltaic (PV) industry is growing at a rapid rate, but the industry would grow even faster if costs for the final products could be further reduced. One strategy for reducing module cost is to reduce the amount of semiconductor material needed, since the cost of the silicon solar cells typically comprises more than one-half of the module cost.

One way of reducing the required amount of semiconductor material and consequently the final cost is to use the light concentration concept. The argument is that in concentrated photovoltaic (CPV) systems the sun collecting area is a cheaper optical element than a solar cell. Therefore, the cost reduction is achieved by a reduction of the area of highly-efficient and quite expensive solar cells using cheap optical elements concentrating the light.

However, there are currently certain barriers making concentrators practically non-existent on the market. The barriers are related to the relative complexity of the concentrating systems, i.e. requirements of accurate alignments, tracking systems, maintenance. Moreover, the cost reduction of the conventional PV flat-panels in the last decade has reduced the interest towards concentrating systems.

Nowadays, the cost of conventional flat-panels is of the order of 0.5\$/Wp. Such a low cost is principally due to the development during the last years of new methods of production, which are relatively simple from the technological point of view and cheaper than the more complex methods commonly used in electronic devices

production. For example, conventional solar cells use laser ablation to open the passivating layer and screen printing technology to define the metal structures. These technologies work poorly in high-efficiency concentrator solar cells, which are fabricated by means of CMOS-like fabrication technology, in which photolithography is used to precisely define the electrical active structures of the cell. These technology solutions led to cell efficiencies much higher than the conventional solar cells. Although the technology required for concentrator solar cells production is more expensive than the one used for conventional solar cells, the latter are only a small part of the cost of the whole concentrating PV system. Therefore, they can afford to be more expensive to be more efficient [1].

In the last years, also the cost of the high-quality fabrication process required for concentrator solar cells has significantly decreased. Nowadays, a cost lower than 0.10 \$/Wp is achievable for mass-production of concentrator solar cell 23% efficient for CPV systems working at 200 suns. This means that the final cost of concentrator systems will be dominated by the optics and tracker costs. If the market will be able to offer cheap and efficient optics and tracking systems, concentrating photovoltaics can still play an important role in PV industry.

1.2 Thesis outline

This work presents the design, realization and characterization of high efficiency Si photovoltaic cells for concentration applications. The main aim of this work is to master the Si PV technology and the underlying physics, in order to be able to optimize the cells for specific concentration levels and to propose and develop new cell concepts.

In order to develop high efficient Si concentrator solar cells two different ways have been followed. The first one aims to optimize the design and the fabrication process of a conventional front-side contacted cell, based on a planar n^+p junction. Although this cell structure is rather simple and cheap to produce, it can reach high conversion efficiency under concentrated light, if its design and the fabrication process are suitably optimized. The second way aims to investigate and propose completely new cell designs which use some “three-dimensional” structures, such as deep-grooved contacts and through-silicon vertical connections. The new cell designs allow to overcome some intrinsic limits of the conventional front-side contacted cells and could be worthwhile to improve the conversion efficiency in future real applications.

Chapter 1 introduces the PV technology and reports the state of the art of

silicon concentrator solar cells.

Chapter 2 is about the physics and theory related to silicon based PV with specific attention to the concentration context. The main focus is set on the recombination mechanism in silicon solar cells under high-injection conditions. The main variables and equations to be known in order to master the technology are presented and analyzed.

Chapter 3 describes the process developed during the thesis work to produce the solar cells. An optimized structure and a reliable fabrication process for front-side contacted cells are outlined. Particular attention is given to the fabrication process of a textured surface. Surface texturing technology was optimized and it resulted to be nearly perfect leading to very low reflection losses, very high light trapping and very high short circuit densities.

Chapter 4 is about simulation and optimization of front-side contacted concentrator solar cells. Analytical and numerical algorithms are presented and used to investigate the physics of the device and perform multi-parameter optimizations addressing the process development. The theory examined in Chapter 2 is here widely recalled. Device modeling techniques have been used to optimize the front metal grid, emitter doping profile, substrate resistivity and cell thickness. Finally, numerical simulations have been exploited to propose a completely new cell design (the DEPC cell) aimed at reducing the resistive losses in the cell base by means of deep-grooved contacts designed on the rear side of the cell.

In **Chapter 5** the experimental methods for cells characterization under concentrated light are described. An innovative concentrator solar simulator for indoor cell characterization is presented. A brief description of the testing system is reported with an analysis of the measurement errors.

Chapter 6 presents the experimental trends of the developed front-side contacted concentrator solar cells with respect to both layout and fabrications variations. In particular, the role of the metal grid, finger pitch, texturing, substrate resistivity and doping method is investigated, and the results are discussed. As a result of this study, a cell 23% efficient at 100 suns has been realized.

In **Chapter 7** an innovative cell concept, based on back-contacted vertical junction is presented. The cell design aims to overcome some intrinsic limits of the conventional front-contacted solar cells: the light-shadow due to the front metal grid and the resistivity losses in the base. Cell modeling and fabrication process of these devices are briefly described, and the first experimental results are outlined. Simulations and first experimental results show that the proposed back-contact vertical junction solar cell is a very promising design for silicon concentrator cells although

further efforts have to be done to exploit the full potential of this design.

1.3 Overview of silicon concentrator cells

The concentration of sunlight onto a solar cell has been used since the middle of 70s, when the first photovoltaic concentrator was developed. A PV concentration system (or CPV) is composed by the following elements:

- Cells: Concentrator solar cells with specific characteristics different from those of non-concentrator PV modules.
- Optics: An optical device that increases the luminous flux on the cells. They may include the primary optics which is the light collector, usually a Fresnel lens or a mirror, and the secondary optics that receives the light from the primary and performs one or more of the following functions: spectral filtering, light homogenization or a change in the light direction.
- Module: One or several cells assembled with the optics and other components that receive non-concentrated light. It must provide current extraction and heat dissipation as well as in some cases encapsulation.
- Tracker: It is a set of structural elements and moving mechanisms that receive and fix the modules and keep them directed towards the sun and the cells in focus. It must provide a tracking control that commands the mechanism of the tracking structure so that the sun is properly focused.

In this thesis the focus is on the cell element. Concentrator solar cells differ from conventional solar cells in the way that they are able to extract more current per unit of area. Many different concentrator cell concepts have been developed over the last 30 years [2]. However, all these cell concepts are optimized with respect to at least one of the following demands:

- Minimized shadowing losses at the front side.
- Low series resistance losses in the grid structure.
- Small resistance losses due to the lateral current flow in the diffused layer between the grid lines, and small resistance losses in the base.
- Good light trapping for the optimal use of the incoming light.

Many concentrator cells have a classic structure, with an extended n - p junction on the front face. One basic cell concept is the *PESC cell* (shown in Figure 1.1) developed by the UNSW [3]. The series resistance is reduced by using a carefully designed grid and the front surface is passivated by means of a dielectric layer. A

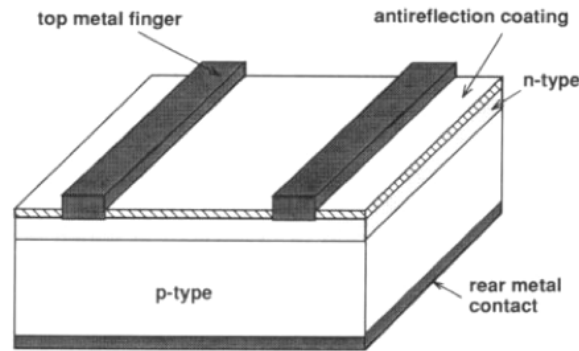


Figure 1.1: PESC silicon cell design developed in the early 1970s which became a standard design for over a decade (picture taken from [4])

Similar cell, but based on n -type silicon substrate is the p^{++} - n - n^{++} cell from the Sandia National Laboratories. Efficiencies of around 20% were reached from 40 to 200 suns [5].

In order to limit the shading due to the front metal grid the *V-groove cell* (Figure 1.2) was proposed [6]. The cell is optimized for reducing the front reflection while keeping the series resistance losses low. The idea of the concept is to use highly reflective metal on one side of the grooves. Due to the structured surface, the light trapping of this cell is increased. Unfortunately, due to the high metal coverage of the surface without any deep diffusion underneath the contact, the recombination at the contacts and the contact resistance are high. A high resistance limits the cell performance under high concentration levels. Due to the contact problems, the best application field for the V-groove cell concept seems to be low-cost concentrator systems with a geometrical concentration ratio in a range from 5 to 40 suns.

Nevertheless, there is a fundamental limitation in cells with a classic structure for the series resistance that is independent of the grid and the cell size: it is the base series resistance. In order to overcome the limitation, Swanson, Sinton and co-workers developed a new type of concentrator silicon cell [7], the *back-junction point-contact silicon solar cell* (see Fig. 1.3). The cell has a slightly doped base of high lifetime and p^+ and n^+ dot-shaped emitters, which are the positive and the negative contact areas of the solar cells respectively, all located closely intercalated at the back face of the cell. In these cells no current flows from the front to the

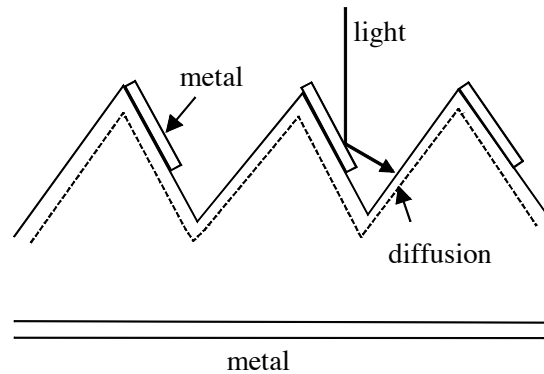


Figure 1.2: A V-groove solar cell which allows all light reflected from the top contact metal to impinge the other side of the grooved surface [6].

back, like in conventional cells, but carriers of both types do, annihilating the overall current. For this reason these cells have no base component of the series resistance. Thus they can operate at higher concentration. The cells do not have any grid on the front face allowing for a better efficiency and all the electric contacts are made on the rear face through interdigitated dense grids. The cell holds the efficiency record of 27.5% at 100 suns.

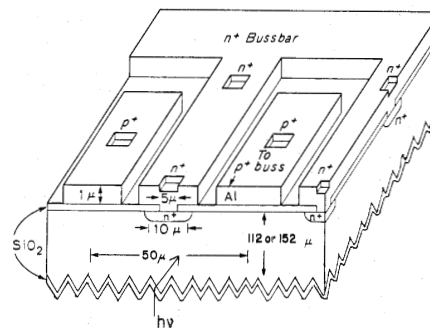


Figure 1.3: A scheme of a textured point-contact solar cell, which has point contacts at the rear side.

However, in these cells, the high concentration efficiency is not limited by series resistance but by the super-linear increase in the Auger recombination at high luminous flux caused by the steep profile of carriers produced by this illumination. This leads to a sub-linear current-light characteristic, which precludes operation at very high concentration. Moreover, this kind of cell requires high-quality materials with long bulk lifetime of about 1 ms and very thin substrates ($< 90 \mu\text{m}$) or even epitaxially grown layers. Both these requirements lead to an increase in cost.

CHAPTER 2

Basics of concentrator silicon solar cells

In this chapter the theoretical basics of solar cells are summarized. The fundamental notions indispensable to understand the working principles of a photovoltaic cell, i.e. the theoretical model, equivalent circuit and electrical characteristics are explained. Moreover, some physical aspects of silicon solar cells working under concentrated light are discussed. The main focus is set on the recombination mechanisms in silicon solar cells under high-level injection conditions. At the end of the chapter the most important parameters of concentrator solar cells are given and discussed.

2.1 Origin of the photovoltaic action

Photovoltaic energy conversion results from a three step process: charge generation, charge separation and charge transport. In semiconductor photovoltaic cells, charge generation is provided by the interaction of light photons with semiconductor: incoming photons are absorbed by the semiconductor and create electron-hole pairs by means of the photoelectric effect. The charge transport instead is due to the drift-diffusion charge mechanisms inside the semiconductor. The remaining stage, charge separation requires some kind of driving force and it is commonly obtained by means of a junction between electronically different materials. The p - n homojunction is the most widely used device structure in photovoltaics. Selective doping of the different sides of a semiconductor wafer p -type and n -type leads to a poten-

tial barrier to charge carrier flow, so that there is a low resistance path for electrons to the n contact and for holes to the p contact, thus providing the asymmetry in resistance which is necessary for photovoltaic conversion.

The solar cells described in this work are made on silicon p -type substrate, on which an n -doping diffusion is performed on the top surface of the cell in order to obtain the p - n junction. The shallow n -doped region is commonly named “*emitter*”. The p - n PV cells can be viewed as wide-area diodes suitably designed and optimized to efficiently absorb and convert light energy from the sun into electrical energy.

2.2 Carriers in semiconductor

2.2.1 Semiconductor at equilibrium

In a semiconductor at equilibrium the total density of electrons and holes is described by the Fermi Dirac Statistics, which describes the average probability that an electron state at energy E will be occupied at some temperature T . Under Boltzmann approximation n and p densities can be evaluated exactly:

$$n = N_c e^{\frac{(E_F - E_c)}{k_B T}} \quad (2.1)$$

$$p = N_v e^{\frac{(E_v - E_F)}{k_B T}} \quad (2.2)$$

where E_F , E_c and E_v are the Fermi level, valence energy and conduction energy level of the semiconductor, and the constants N_c and N_v are called the effective conduction and valence band densities of states respectively, and they are equal to:

$$N_c = 2 \left(\frac{m_c^* k_B T}{2\pi\hbar} \right)^{3/2} \quad \text{and} \quad N_v = 2 \left(\frac{m_v^* k_B T}{2\pi\hbar} \right)^{3/2}$$

The product np is a constant and it is used to define a constant property of the material, the *intrinsic carrier density* n_i :

$$np = n_i^2 = N_c N_v e^{-\frac{E_g}{k_B T}} \quad (2.3)$$

The Boltzmann approximation for n and p hold as long as:

$$\frac{E_c - E_F}{k_B T} \gg 1 \quad \text{and} \quad \frac{E_F - E_v}{k_B T} \gg 1$$

i.e. conditions which are usually true for a semiconductor at equilibrium, but they can not be true if the semiconductor is highly doped. High-doped semiconductor regions are often present in solar cells, for example in the emitter region. In this case, the full form of the Fermi Dirac distribution must be used to evaluate n and p .

2.2.2 Semiconductor under light bias

In a photovoltaic device, light produces a separation of charges. Under light bias, the Fermi level is split in two *quasi Fermi levels*, called E_{Fn} and E_{Fp} for electrons and holes respectively. Under this assumption, and assuming quasi thermal equilibrium, the Boltzmann approximation can still be used, and the electron and hole densities in a semiconductor under bias are given by:

$$n = N_c e^{\frac{(E_{Fn}-E_c)}{k_B T_n}} \quad (2.4)$$

$$p = N_v e^{\frac{(E_v-E_{Fp})}{k_B T_p}} \quad (2.5)$$

where T_n and T_p are the effective electrons and holes temperature. However, in photovoltaic devices it is usually assumed that $T_n = T_p = T$, the ambient temperature. Equations 2.4 and 2.5 are the same as Eqs.2.1 and 2.2, except that the Fermi level E_F is substituted with E_{Fn} and E_{Fp} .

Current in semiconductors under bias

The *photovoltaic action* arises from the driving force separating charges. We analyze it in terms of the contributions to the photocurrent J . The total photocurrent may be described as the sum of electron current J_n and holes current J_p , and using the Boltzmann Transport equation, we obtain the following relation indicating that the current is proportional to the gradient of the quasi Fermi levels at a point

$$J = J_n + J_p = \mu_n n \Delta E_{Fn} + \mu_p p \Delta E_{Fp} \quad (2.6)$$

where $\mu_{p,n}$ is the mobility coefficient for holes and electrons. This is the most compact form to describe the current in the semiconductor. If we differentiate the Eqs. 2.4 and 2.5, the quasi Fermi levels gradients may be calculated as in the following:

$$\nabla E_{Fn} = (\nabla E_c - kT \nabla \ln N_c) + \frac{kT}{n} \nabla n \quad (2.7)$$

$$\nabla E_{Fp} = (\nabla E_v + kT \nabla \ln N_v) - \frac{kT}{p} \nabla p \quad (2.8)$$

With reference to Figure 2.1, the E_c and E_v may be expressed in terms of the electron affinity χ , electric field F , and band gap E_g

$$\nabla E_c = qF - \nabla \chi \quad (2.9)$$

$$\nabla E_v = qF - \nabla \chi - \nabla E_g \quad (2.10)$$

Substituting ∇E_{F_n} and ∇E_{F_p} in Eq. 2.6 we obtain:

$$J_n = \mu_n \frac{kT}{q} \nabla(n - n_0) + \mu_n(n - n_0)(qF - \nabla\chi - kT \nabla \ln N_c), \quad (2.11)$$

$$J_p = \mu_p \frac{kT}{q} \nabla(p - p_0) + \mu_p(p - p_0)(qF - \nabla\chi - \nabla E_g + kT \nabla \ln N_v) \quad (2.12)$$

In either equation, the first term represent *diffusion* due to a concentration gradient and the second represents *drift* under net electric field, which may be due to compositional gradients.

Under illumination, $n > n_0$ and $p > p_0$. Then, if the electric field is not zero, a net current will result.

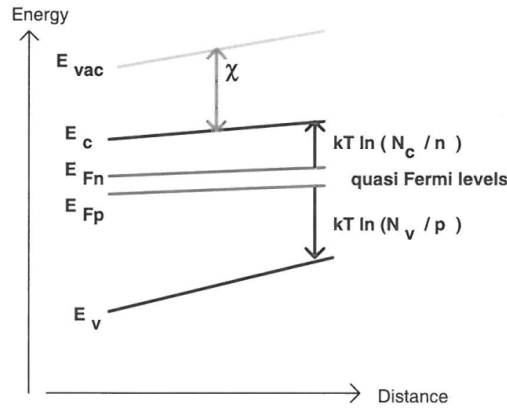


Figure 2.1: Built in field and charge separation in a semiconductor under illumination (taken by [8]).

In summary, with reference to Eqs. 2.11 and 2.12 the various conditions which can give rise to charge separation in a semiconductor are:

1. gradient in the work function (electrostatic field F)
2. gradient in the electron affinity χ
3. gradient in the band gap E_g
4. gradient in the band densities of states

The fields generated by the last three mechanisms (2 – 4) can be fairly limited in crystalline semiconductors. Change in the work function (1) instead, play the principal role in p - n junction solar cells because it can also be achieved simply by varying the doping level in a single semiconductor. This is the widely used method to establish the charge separating field in solar cells.

2.3 The solar spectrum

Development, optimization and characterization of photovoltaic cells involve knowledge of the used energy source: the sun. Sun surface behaves like a black body at about 5800°K with an emission peak situated on a wavelength of 500 nm and a power of about 60 MW/m² [8]. Just above Earth's atmosphere the radiation intensity is about 1.36 kW/m²; on Earth surface instead, this irradiance is attenuated due to different factors: absorption by molecules composing atmosphere, climatic conditions, season and latitude of observation site [9]. As solar radiation passes through the atmosphere, gasses, dust and aerosols absorb the incident photons and modify the solar spectra. The modifications depend on the light path in the atmosphere. The *Air Mass* is the path length which light takes through the atmosphere normalized to the shortest possible path length (i.e., when the sun is at the Zenith). The Air Mass quantifies the reduction in the power of light when it passes through the atmosphere and is absorbed by air and dust. The Air Mass is defined as:

$$AM = \frac{1}{\cos \theta} \quad (2.13)$$

where θ is the angle of incidence ($\theta = 0$ when the sun is at the Zenith). In order to standardize the measurement conditions and compare the performances of photovoltaic cells, the International Standard ISO 9845-1 defines three spectra [10]:

- The **AM0** is the standard spectrum just above the standard atmosphere, used for space applications. It has an integrated power of 1366.1 W/m².

Two standards are defined for terrestrial use:

- The **AM1.5G (Global spectrum)** is designed for flat plate modules and has an integrated power of 1000 W/m² (100 mW/cm²).
- The **AM1.5D (Direct spectrum)** is defined for solar concentrator work. It includes the direct beam from the sun plus the circumsolar component in a disk 2.5 degrees around the sun. The direct plus circumsolar spectrum has an integrated power density of 900 W/m².

The AM1.5G spectrum includes also diffuse and indirect component (due to scattering and reflection in the atmosphere and surrounding landscape) which can account for about 10% of the light incident on a PV cell, while an AM1.5D (direct) does not. The AM0, and AM1.5G and AM1.5D spectra are shown in Figure 2.2.

In CPV field the incident power is commonly indicated in terms of “suns”, where 1 sun is equal to 0.09 W/cm² and 0.1 W/cm², for direct and global AM1.5 spectra respectively.

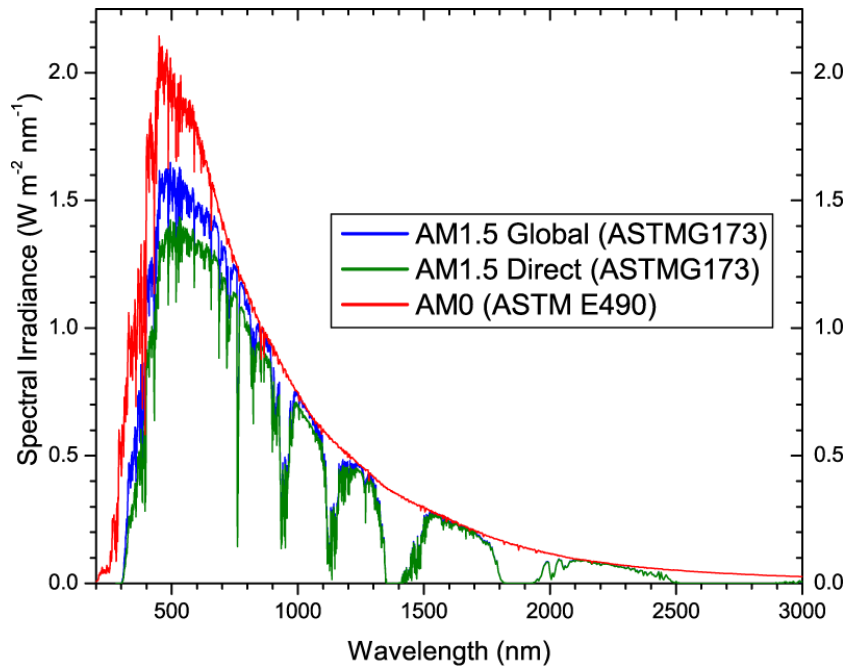


Figure 2.2: A comparison of the spectral irradiance for AM0, AM1.5G and AM1.5D spectra. AM0 (red line) is the spectrum just above Earth’s atmosphere, AM1.5G (blue line) indicates the Global terrestrial spectrum and the AM1.5D (green line) represents the Direct + circumsolar spectrum.

The AM1.5G and AM1.5D spectra differ from each other principally in the UV and blue spectral region. This is due to the fact that the direct radiation cannot exploit the radiation from the blue sky or from reflections of the clouds.

Concentrator solar cells should be suitably designed to work under the direct solar spectrum because the differences between the global and direct solar spectra could introduce some important differences in the cell response with respect to the standard 1 sun cells, which work under the global spectrum. This is especially true for multijunction concentrator solar cells, where the currents generated in each junction must be equal to each other [11] [12]. On the other hand, for one-junction and low-bandgap solar cells (as in the case of silicon), the difference between the direct and global spectrum does not influence the cell performance, therefore in some cases it may be neglected [13].

2.4 Generation and recombination processes in semiconductors

In order to generate a photocurrent, the incident solar radiation is absorbed in the solar cells and photogenerated carriers are created. On the other hand, as compet-

itive mechanism, the generated carriers may be lost via recombination. Therefore, the final output is determined by the balance between light absorption, current generation and charge recombination and it is described by the current continuity equation:

$$\frac{\partial J_n}{\partial x} = -q(G_n - U_n) \quad (2.14)$$

$$\frac{\partial J_p}{\partial x} = q(G_p - U_p) \quad (2.15)$$

where $G_{n,p}$ is the rate of generation of electrons and holes and $U_{n,p}$ is the recombination rate. These equations are general and the particular forms of G and U depend on the material and environment.

2.4.1 Photogeneration

Generation is the promotion of an electron from valence to conduction band, event which increases the number of free carriers available to carry charge. The energy input required to generate the excess of carriers can be provided by the thermal energy (vibrational energy of the lattice) or light. For each generation process there is an equivalent recombination process, which is due to microscopic reversibility. Thus the thermal generation is balanced by the equivalent recombination rate and we can consider only the net generation rate due to the light:

$$G_n = G_n^{total} - G_n^{thermal}$$

The generation process is presented only in a macroscopic way. A microscopic analysis should be treated in terms of quantum mechanics (Fermi gold rule), and a complete tractation can be found in [8]. The macroscopic absorption α describes how the light intensity is attenuated on passing through the material. If we consider a light flux of photons with energy E and intensity I_0 normally incident on a slab of absorbing material, the intensity at a depth x is given by:

$$I(x) = I(0)e^{-\int_0^x \alpha(E)dx'} \quad (2.16)$$

For indirect band materials, as in the case of silicon, $\alpha(E)$ has the form of:

$$\alpha \propto (E - E_g)^2 \quad (2.17)$$

The absorption coefficient and the light intensity attenuation in Silicon are shown in Fig. 2.3 as a function of wavelength.

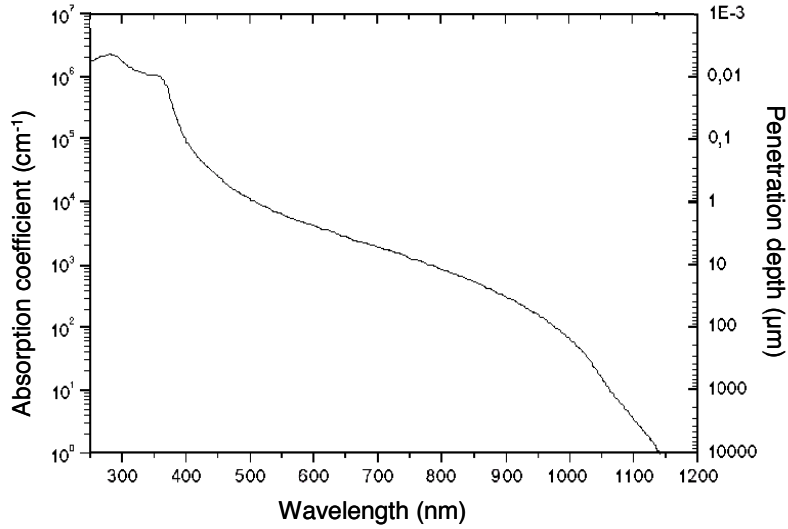


Figure 2.3: Silicon absorption coefficient and photons penetration depth. For wavelength lower than 365 nm, majority of incident photons are absorbed inside first 10 nm of material.

Eq. 2.17 indicates that only photons with energy equal or higher than E_g can be absorbed. Since Silicon has $E_g = 1.11$, only photons with wavelength smaller than 1100 nm can be absorbed. Photons with energy lower than E_g pass through silicon without absorption. Moreover, Eq. 2.17 indicates that energetic photons (UV and blue light) are attenuated more than red and Infra Red (IR) photons. Fig. 2.3 shows the penetration depth (defined as the distance in the material at which the light drops to about 36% of its original intensity) as a function of the wavelength [14]. Light in the blue part of the solar spectrum is absorbed in the first micrometer of silicon, while red light requires more silicon thickness to be completely absorbed.

It should be noted that the generation rate does not depend upon the energy of the absorbed photon, except in that the energy exceed the band gap. When photons with energy higher than E_g are absorbed, they generate carriers with higher kinetic energy, but that energy is quickly lost via *thermalization* and only E_g of energy remains to be collected. This means that the important quantity is the number of photons and not their energy. In fact, each photon can promote to the conduction band only one electron independently from photon energy. It should be noted that the energy loss via thermalization is the principal intrinsic factor limiting the conversion efficiency of a solar cell [15].

If we assume that all absorbed photons generate free carriers, the rate of carrier generation per unit volume at a depth x below the surface is given by:

$$g(E, x) = (1 - R(E))\alpha(E)S(E)e^{-\int_0^x \alpha(E)dx'} \quad (2.18)$$

where $S(E)$ is the spectra of the incident flux and $R(E)$ is the reflectivity of the surface at normally incident light as a function of energy. The total generation rate at x will be equal to:

$$G(x) = \int g(E, x) dE. \quad (2.19)$$

2.4.2 Recombination in low-level injection

Several different recombination mechanisms are involved in photovoltaic devices. They should be divided in two categories: *unavoidable* recombination processes which are due to the essential physics in the material, and *avoidable* processes which are due to the presence of imperfections and contaminations in the material. The unavoidable processes present in a PV cells are the *Radiative recombination* and the *Auger recombination*, while the avoidable recombination processes involve relaxation by way of a localized trap state due to the impurities in the crystal. These are named *Shockley Read Hall recombination (SRH)* and *Surface recombination*, and usually are the dominant mechanisms. We can distinguish two different work conditions of a silicon PV cell, depending on the generated carrier density in the semiconductor with respect to the intrinsic material doping density (N_A for p -doped silicon):

- **Low-level injection**, in which the generated free carriers density is much lower than the doping level $\Delta p \ll N_A$. It is a common condition experienced by solar cells under 1 sun illumination.
- **High-level injection**, in which the generated free carriers density is higher than the doping level $\Delta p \gg N_A$. High-level injection may be reached by concentrator solar cells, due to the high incident power of the concentrated light, which increases the photogenerated carrier density.

The recombination rates of the different mechanisms depend in general on the injection condition. In the following paragraphs we are going to show a description of the recombination mechanisms in silicon solar cells under low-injection, while in Section 2.6 the recombination under high-level injection will be treated.

Radiative recombination

In radiative recombination, an electron from the conduction band combines directly with a hole in the valence band and releases a photon. The emitted photon energy is equal to the band gap, and is therefore only weakly absorbed, so that it can escape

the semiconductor. Under Boltzmann approximation the radiative recombination rate is proportional to the excess carrier densities and is given by:

$$R_{rad} = B_0(pn - n_i^2) \quad (2.20)$$

where B_0 is the radiative rate coefficient, a constant property of the material. Since silicon is an indirect semiconductor this recombination process is improbable and in low injection conditions can be neglected.

Auger recombination

In Auger recombination, a collision between two similar carriers results in the excitation of one carrier to higher kinetic energy, and the recombination of the other across the band gap with a carrier of opposite polarity. The extra kinetic energy given to the other carrier will be lost as heat. The Auger recombination is a three-bodies process: an electron and two holes or a hole and two electrons are involved, consequently the rate is proportional to the densities of all three carriers, so that the net rate is:

$$R_{Aug} = C_n(n^2p - n_0^2p_0) + C_p(np^2 - n_0p_0^2) \quad (2.21)$$

where $C_{n,p}$ are the Auger coefficients, constant and dependent on the material.

Under low-level injection and p -doped semiconductor, the Eq. 2.22 can be approximated with

$$R_{Aug} = C_p N_A^2 (n - n_0) \quad (2.22)$$

SRH Recombination

Recombination through defects, also called Shockley-Read-Hall or SRH recombination, does not occur in a perfectly pure, undefected material, but it is usually the most important recombination processes in a real semiconductor. The defects in the crystal introduce some energy levels between the valence and the conduction bands., which act as trap states. When a free carrier is captured by a trap, the carrier can be subsequently released by thermal activation. Alternatively, if the trap captures a carrier of the opposite polarity before the first carrier is released, the two carriers recombine and the trap has been emptied again. The net recombination rate is:

$$R_{SRH} = \frac{np - n_i^2}{\tau_{n,SRH}(p + p_t) + \tau_{p,SRH}(n + n_t)} \quad (2.23)$$

where n_t and p_t are the the values of the electrons and holes densities, when the Fermi levels are equal to the trap energy level, while $\tau_{n,SRH}$ and $\tau_{p,SRH}$ are the

lifetime relative to SRH recombination for electrons and holes respectively. The concept of lifetime will be discussed in the following section.

For p -type doped semiconductors (provided that $\tau_n \gg \tau_p n_t$ and $N_a \gg p_t$) and under the low-level injection assumption, Eq.2.23 simplifies, and the recombination rate becomes proportional to the excess minority carriers:

$$R_{SRH} = \frac{n - n_o}{\tau_{n,SRH}} \quad (2.24)$$

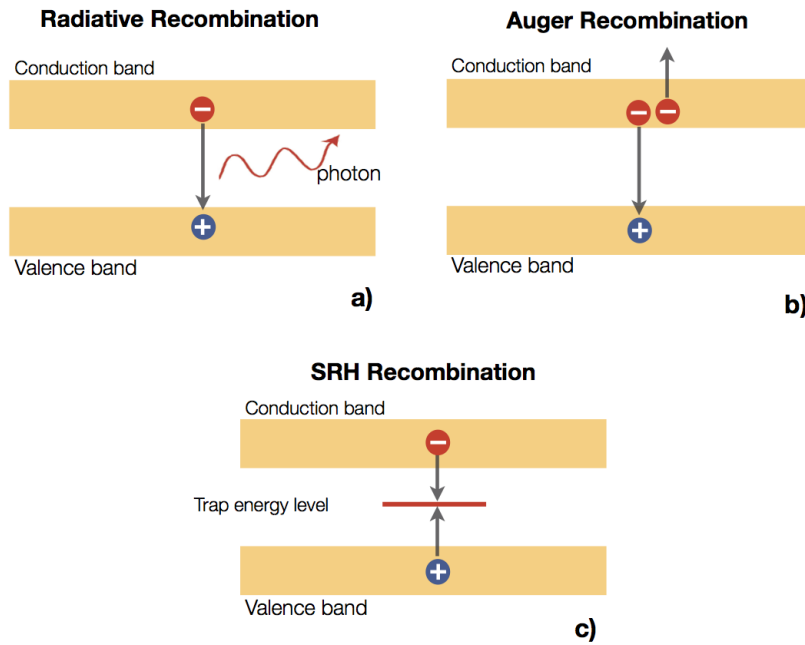


Figure 2.4: Schematization of different recombination mechanisms present in a solar cell. The radiative recombination (a) is negligible in silicon devices, while Auger (b) and SRH (c) are the dominant recombination mechanisms.

Surface recombination

In real materials, defects are much more likely to occur at the surface and the interfaces between different crystal regions. Localised trap states at surfaces include both crystal defects due to broken bonds and impurities which are deposited from the external environment, or which are concentrated at interfaces during growth. Due to the nature of the surface defects, the recombination rate can be derived in the similar way used for SRH recombination rate. With reference to Eq.2.24, in p -type materials the surface recombination rate under low-level injection conditions can be expressed as

$$R_{Surf} = S_n(n - n_0) \quad (2.25)$$

where S_n is used in place of τ_n , due to the fact that the trap states responsible for recombination are concentrated in a two-dimensional rather than three-dimensional space and its more meaningful to express the recombination in terms of *Surface Recombination Velocity (SRV or $S_{n,p}$)* (cm/s), rather than in terms of lifetime.

Commonly in PV cells the SRV should be kept as low as possible in order to avoid efficiency losses. The values of S_n and S_p depend on the passivation properties of the front and back cell surfaces. Surfaces passivated with thermal oxide show very low SRV, while non-passivated surfaces or metal-semiconductor interfaces show higher values. In the last years many passivating techniques have been developed to obtain low SRV. In particular, cell passivation with thermal oxide and PECVD Silicon Nitride show good performance in terms of surface recombination [16].

2.4.3 Carrier lifetime and diffusion length

A critical parameter in a solar cell is the rate at which recombination occurs. Above we have derived the recombination rate for each recombination mechanism. Two parameters commonly used to represent the magnitude of the recombination rate are the *minority carrier lifetime* (τ) and the *minority carrier diffusion length* (L).

The minority carrier lifetime of a material is the average time which a carrier can spend in an excited state before it recombines. It is often referred to as the “lifetime”. Stating that “a silicon wafer has a long lifetime” usually means minority carriers generated in the bulk of the wafer by light or other means will persist for a long time before recombining. Depending on the structure, solar cells made from wafers with long minority carrier lifetimes will usually be more efficient than cells made from wafers with short minority carrier lifetimes. The terms “long lifetime” and “high lifetime” will be used interchangeably in this work.

The lifetime is related to the recombination rate by:

$$\tau = \frac{\Delta n}{R} \quad (2.26)$$

We can now calculate the minority carriers lifetime for each recombination process by using the definition 2.26 and the Eqs. 2.20-2.25. For a p -type semiconductor in

low-injection we obtain the following expressions:

$$\tau_{Radiative} = \frac{1}{B_0 N_A} \quad (2.27)$$

$$\tau_{Auger} = \frac{1}{C_p N_A^2} \quad (2.28)$$

$$\tau_{SRH} = \frac{1}{B_n N_t} \quad (2.29)$$

$$\tau_{Surface} = \frac{W}{2S_n} \quad (2.30)$$

where N_t is the density of the trap states, $B_n = constant$ and W is the semiconductor thickness.

Total recombination in the semiconductor may be described by the *effective lifetime*, which contains the sum of the recombinations mechanisms all together

$$\frac{1}{\tau_{eff}} = \frac{1}{\tau_{Rad}} + \frac{1}{\tau_{Aug}} + \frac{1}{\tau_{SRH}} + \frac{1}{\tau_{Surf}} \quad (2.31)$$

$$\frac{1}{\tau_{eff}} = B_0 N_A + C_p N_A^2 + B_n N_t + \frac{2S_n}{W} \quad (2.32)$$

Since in low-level injection condition the approximated recombination rates explained earlier are linear with respect to the minority carriers density, the total effective lifetime is a constant parameter and depends only on the material quality, thickness, doping and surface passivation. In particular, the lifetime will depend on the number of defects N_t present in the material and on the doping level N_A . Commonly, since doping increases defects in the material, doping will also increase the rate of SRH recombination. In addition, since the Auger recombination rates is higher in heavily doped material, the recombination process is itself enhanced as the doping increases. For these reasons, high-doped semiconductors commonly show lower lifetime with respect to low-doped semiconductors.

In a more general way, if the recombination rates are not linear with respect to the carrier density, like in the case of high-level injection, the lifetime becomes carrier density dependent $\tau(\Delta n)$. The case will be treated in Section 2.6.

The second parameter related to the recombination rate, i.e. the *minority carrier diffusion length* L_D , is the average distance that a carrier can make from the point of generation until it recombines. The diffusion length of electrons in p -type semiconductor is related to the carrier lifetime by the diffusivity according to the following formula:

$$L = \sqrt{D_n \tau} \quad (2.33)$$

where D_n is the diffusivity in $[\text{cm}^2/\text{s}]$.

2.5 Current-voltage characteristics of a solar cell in low-level injection

When an p - n junction is formed, holes diffuse from the p -type region into the n -type and, similarly, electrons from the n -type material diffuse into the p -type. This happens in order to compensate the concentration difference of holes and electrons between the two types of semiconductors. As the carriers diffuse, the charged impurities (ionized acceptors in the p -type material and ionized donors in the n -type material) remain uncovered because no longer screened by the majority carriers. The transition region between the n -type and the p -type semiconductors is called the “*space-charge region*” (*SCR*) or “*depletion region*”, since it is depleted of both free holes and electrons, while the remainder areas are called *neutral regions*.

2.5.1 Basics equations of p - n junction

A common way to analyze the current behavior of silicon solar cells is to apply the current density, the drift plus diffusion and the continuity equation. It is an efficient approach to understand the transport processes in the pn -junction of a device. The applied basics of semiconductors and silicon solar cells can be found in [8] [17] [9] [18]. For modeling the steady-state carrier transport in silicon, the standard equations are:

- **The current transport equations.** In the SCR region an electric field is present in addition to the concentration gradient leading to drift current and diffusion current flows:

$$J_e = q\mu_e n \bar{E} + qD_e \nabla n \quad (2.34)$$

$$J_h = q\mu_h p \bar{E} + qD_p \nabla p \quad (2.35)$$

where \bar{E} is the electric field, $\mu_{e,h}$ are the mobilities of the carriers, $D_{e,h}$ are the diffusion coefficients and n, p are the hole and electron densities showed in Eqs. 2.1 and 2.2 The total current density is the sum of Eqs. 2.34 and 2.35.

- **The continuity equations.** The number of carriers flowing in a volume minus the carriers which recombine and plus the carriers which are generated in this volume equals the number of carriers flowing out of the volume:

$$\nabla J_e = -q(R_{rec} - G_l) \quad (2.36)$$

$$\nabla J_h = q(R_{rec} - G_l) \quad (2.37)$$

where R_{rec} and G_l are the recombination and generation rates.

- **The Poisson equation.** The space charge distribution and the electrostatic potential in the *SCR* region are given by the Poisson equation:

$$\nabla\Phi^2 = -\frac{1}{\varepsilon}(p + N_D - n - N_A) \quad (2.38)$$

2.5.2 Solar cell in the dark

In the dark, the generation current G is equal to zero. The previous equations can be analytically solved and the current-voltage characteristic curve can be calculated:

$$J(V) = J_{dark}(V) = J_0(e^{\frac{qV}{k_B T}} - 1) \quad (2.39)$$

where V is the bias voltage and J_0 is the reverse saturation current due to diffusion. This is the well-known *Shockley* or *ideal diode* equation and is often quoted for the dark current of a solar cell. [8]

2.5.3 Cell under illumination

Under illumination $G \neq 0$ and Eq. 2.39 is modified to take into account the photogenerated current:

$$J(V) = -J_{SC} + J_{dark}(V) = -J_{SC} + J_0(e^{\frac{qV}{k_B T}} - 1) \quad (2.40)$$

where J_{SC} is the current under *Short Circuit Conditions*. Commonly the current sign in the Eq. 2.40 is inverted and the J_{SC} is considered positive.

This equation is derived under two approximations:

- First, we assume that the SCR region around the junction contains no free carriers so that the potential step is completely taken up by the fixed space charge of the doped materials near the junction. This is the *depletion approximation*. In this approximation the electric field vanishes in the neutral regions.
- The second approximation is that the recombination rates in the neutrality regions are linear in the minority carrier density.

Under high-level injection these two hypothesis have to be relaxed and the cell equivalent model reviewed. In the following section we derive a new generalized model suitable for cell under high-power incident light.

2.6 Solar cell in high-level injection

When a solar cell is illuminated by high incident power densities, like in the case of PV cells under concentrated light, the generated carriers density increases and becomes higher than the doping density level. In this case the cell is defined to be in high-level injection. In this condition the following approximations can be considered:

- The generated free carriers exceed the base doping concentration: $\Delta n \gg N_D$ and $\Delta p \gg N_A$.
- The concentration of free electrons equals the concentration of free holes ($\Delta n = \Delta p$), which implies that:

$$pn = n^2 = n_i^2 e^{\frac{qV}{kT}} \Rightarrow n = n_i e^{\frac{qV}{2kT}} \quad (2.41)$$

- The number of light-generated free carriers n is much larger than the number of thermal generated carriers n_0 , so that

$$n - n_0 \approx n. \quad (2.42)$$

Under these assumptions the approximations used for the one-diode model and for the recombination rates estimation should be revisited and as a result a new model for concentrator solar cells in high-level injection is derived.

2.6.1 Recombination under high-level injection

Recombination in Depleted Region

In low-level injection the p - n junction model described earlier does not take into account the recombination in the depleted region, since the under the *depletion approximation*, no free carriers are present in the SCR region, therefore the recombination rate is null.

Under high-injection condition the assumption is not valid any more due to the high-density of generated carriers. A more accurate, though not self-consistent, approximation is to calculate p and n densities by the Fermi levels (Eq. 2.4 and Eq. 2.5), and to use the general form of SRH recombination Rate in Eq. 2.23 to calculate the recombination current [8]. It has the approximated form:

$$J_{scr}(V) = J_{scr,0} e^{qV/2k_B T} \quad (2.43)$$

where

$$J_{scr,0} = \frac{qN_iW_{scr}}{\sqrt{\tau_n\tau_p}} \quad (2.44)$$

It should be noted that the SCR recombination term has a *diode ideality factor* equal to 2, differently from the J_0 current, in which the ideality factor is 1.

SRH recombination in doped regions

The SRH recombination rate under high-level injection is derived by the Eq. 2.23 with the high-injection hypothesis in Eq. 2.42. In p-type semiconductors it is equal to:

$$R_{SRH} = \frac{n}{\tau_{SRH}} \quad (2.45)$$

The recombination current due to the SRH recombination can be calculated by using Eqs. 2.41 and 2.45:

$$J_{SRH} = q \int_V R_{SRH} \cdot dV = \frac{W}{\tau_{SRH}} n_i e^{qV/2kT} \quad (2.46)$$

where W is the cell thickness. Thus, the ideality factor for the SRH recombination under high-level injection conditions is also equal to 2 .

When the intrinsic doping level of the semiconductor is very high, SRH recombination in this region can be treated as SRH recombination in the semiconductor under low-level injection. This is due to the fact that the highly doped regions are under low-level injection even for very high irradiation, hence the ideality factor of the recombination in the highly doped regions is always 1.

High-doped regions are commonly present in the front surface of solar cells (*emitter* region) and on the back (*Back surface field* region). Recombination rate in high-doped semiconductors is not simple to calculate in an analytical form. Fermi-Dirac statistics should be used to calculate the carrier densities, and other effects like band gap narrowing and degeneration effects have to be taken into account [19]. In this work, the emitter saturation current is indicated with J_{0e} and the ideality factor is assumed to be 1.

Surface Recombination

For the surface recombination two cases must be distinguished, depending on the local carrier concentrations. If the surface borders with a high-doped region, the dopant concentration is larger than the concentration of the generated carriers and the surface is under low-level injection even for high concentration levels. This leads to an ideality factor of 1 independently of the concentration.

On the other hand, surfaces of low-doped regions, are considered under high-level injection and from Eqs. 2.25 and 2.42 the recombination rate is calculated:

$$R_{surf} = S_n \cdot n \quad (2.47)$$

The recombination current is:

$$J_{surf} = qS \int_{A_{surf}} n \cdot dA = qS n_i \cdot e^{qV/2kT} \quad (2.48)$$

Therefore, the ideality factor of the surface recombination for low-doped regions is 2.

Auger Recombination

The Auger recombination rate in Eq. 2.21 can be approximated under high-level injection as:

$$R_{Auger} = (C_n + C_p)n^3 \quad (2.49)$$

Using Eq. 2.41 the Auger recombination current is equal to:

$$J_{Aug}(V) = qW(C_p + C_n)n_i^3 e^{\frac{3}{2}qV/kT} \quad (2.50)$$

Thus, the ideality factor for the Auger recombination is 2/3 under high-level injection.

Summary of recombination at high-injection conditions

The ideality factors of different recombination mechanism in a solar cell in high injection condition are summarized in Tab. 2.1.

Table 2.1: Ideality factors of recombination mechanisms under high-level injection.

Recombination	Ideality Factor
SRH in depleted region	2
SRH in doped region (base)	2
SRH in high-doped region (emitter)	1
Auger	2/3
Surface of doped region	2
Surface of high-doped region	1

Due to the characteristic dependence of the recombination mechanisms, it should be noted that with the increase of the carrier density the Auger recombination will dominate other recombination mechanisms. This is due to the dependence of

the Auger recombination with the n^3 , as shown in Eq. 2.49. Figure 2.5 shows a comparison of the different recombination mechanisms as a function of the incident power density, in a lightly doped concentrator cell as determined by R. Sinton [20]). In this cell the influence of the Auger recombination in the base becomes dominant over 200 suns.

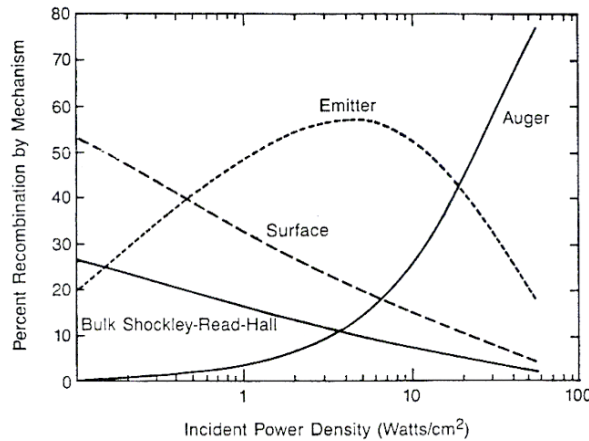


Figure 2.5: The different recombination mechanism versus concentration (taken from [20]), whereas 1 sun correspond to 0.1 W/cm^2 . Under very high-injection conditions the recombination is dominated by the Auger mechanism

2.6.2 Current-Voltage curve under high-injection

Since the recombination currents of a cell in high-level injection correspond to different diode ideality factors, a multi-diode scheme should be used. In particular, a three-diode equivalent circuit represented in Fig. 2.6 is a correct model to represent the different recombination mechanisms.

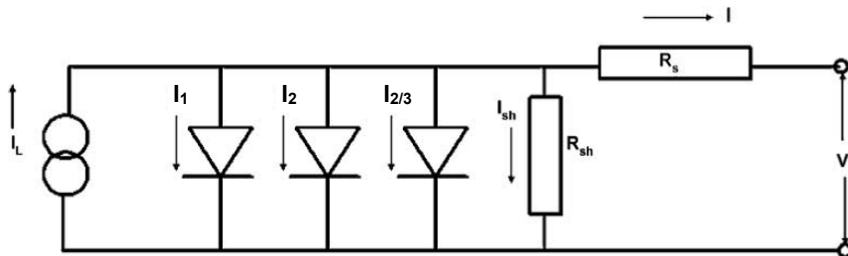


Figure 2.6: Three-diode equivalent circuit which represents a cell in high-injection conditions. Each diode has a different ideality factor. Two lumped resistance are added to the circuit in order to represent the resistive losses in the solar cell.

The corresponding current-voltage characteristic becomes equal to:

$$J(V) = J_{ph} - J_1 e^{qV/kT} - J_2 e^{qV/2kT} - J_{2/3} e^{3qV/2kT} \quad (2.51)$$

where J_1 , J_2 and $J_{2/3}$ are the saturation currents relative to the recombination with 1, 2 and 2/3 diode ideality factors respectively, and J_{ph} is the *photogenerated current density*. Considering Eqs. 2.43 to 2.50, they are equal to:

$$J_1 = J_{0e} + qSA_{surf} \frac{n_i^2}{N_A} \quad (2.52)$$

$$J_2 = \frac{qWn_i}{\tau_{SRH}} + \frac{qN_iW_{scr}}{\sqrt{\tau_n\tau_p}} \quad (2.53)$$

$$J_{2/3} = qW(C_p + C_n)n_i^3 \quad (2.54)$$

In the equivalent circuit shown in Fig.2.6, two lumped resistances (“*shunt*” and “*series*” resistance) are included in order to take into account the parasitic resistance losses in the cell. Parasitic losses play a very important role in concentrator solar cells and they will be treated in depth in Chapter 4.

2.6.3 Cell parameters under concentrated light

In order to deliver a simple insight of the cell performance under concentration, some of the most important cell parameters as the *Short Circuit Current* (J_{SC}), *Quantum Efficiency* (QE), *Open Circuit Voltage* (V_{OC}), *Efficiency* (η) and *Fill Factor* (FF) are summarized below. These parameters are useful to characterize a solar cell in terms of its energy power production capability.

Short Circuit Current

As the first approximation, the J_{SC} can be considered equal to the photogenerated current density J_{ph} , which is linearly dependent from the concentration factor C . Under this assumption:

$$J_{SC}(C) = C \cdot J_{ph,1sun} = C \cdot J_{SC,1sun} \quad (2.55)$$

In a more general way, the J_{SC} is not equal to the J_{ph} but the recombination current under short circuit should be taken into account

$$J_{SC}(C) = C \cdot J_{ph,1-sun} - J_{lost}(C) \quad (2.56)$$

where J_{lost} is the sum of all the recombination mechanisms previously described under short circuit conditions. Generally, the total recombination current is a function of the carrier density, and consequently of the concentration factor.

Quantum efficiency

The recombination under short circuit condition could be quantified and analyzed by means of the *Quantum Efficiency* (QE), which reflects the cell ability to collect the incoming photons under short circuit as a function of the incoming photon wavelength. In other terms, the QE represents the percentage of photons that are converted to electric current when the cell is operated under short circuit. From the experimental point of view, two types of QE can be defined. The *Internal Quantum Efficiency* or *IQE*, reflects the material quality and cell design and it refers to the conversion efficiency of photons that are not reflected or transmitted out of the cell. The second type, the *External Quantum Efficiency* includes also the effect of optical losses such as transmission and reflection. The IQE and the EQE differ only by the *Reflection coefficient* (R) of the solar cell, and are defined as following:

$$IQE(\lambda) = \frac{J_{SC}(\lambda) \cdot h \cdot c}{q \cdot S(\lambda) \cdot \lambda} \quad (2.57)$$

$$EQE(\lambda) = \frac{J_{SC}(\lambda) \cdot h \cdot c \cdot R(\lambda)}{q \cdot S(\lambda) \cdot \lambda} \quad (2.58)$$

where $W(\lambda)$ is the power spectrum of the incident light ($\text{W}/\text{m}^2/\text{nm}$) and $\frac{hc}{\lambda}$ is the photon energy.

Figure 2.7 shows the IQE and EQE of a typical silicon solar cell. It should be noted that for ideal devices the IQE is equal to 1 for wavelength shorter than the band gap. In real solar cells the surface recombination leads to a reduction in the short wavelength region, while the response in the long wavelength region may be reduced by the recombination in the bulk (SRH and Auger) and at the rear surface.

Open Circuit Voltage

Under low concentration, the *one-diode model* (Eq. 2.40) could be used to represent the cell. With this assumption, if J is set equal to 0 in the Eq. 2.40, the V_{OC} is equal to

$$V_{OC}(C) = \frac{kT}{q} \log \left(\frac{C \cdot J_{SC,1-sun}}{J_0} \right) \quad (2.59)$$

The equation means that the V_{OC} grows logarithmically with the concentration.

As shown in Fig. 2.5, at very high concentration level, the Auger is the dominant recombination mechanism, therefore in the diode model the Auger combination current J_{Aug} should be used to represent the inverse saturation current. In this condition, the cell is *Auger limited* and by using the Eq. 2.50, the V_{OC} is equal to:

$$V_{OC}(C) = \frac{2}{3} \frac{kT}{q} \log \left(\frac{C \cdot J_{SC,1-sun}}{qW(C_p + C_n)n_i^3} \right) \quad (2.60)$$

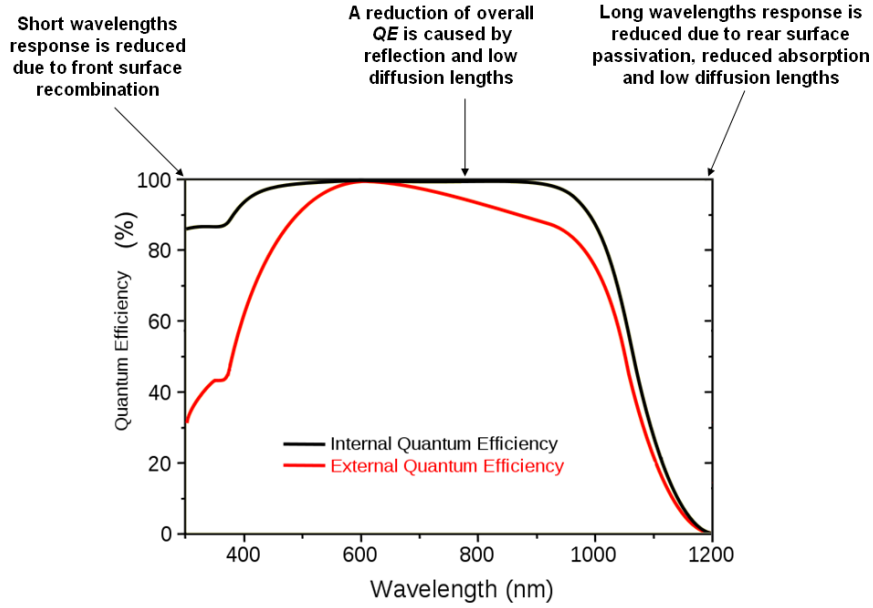


Figure 2.7: Typical IQE (black line) and EQE (red line) of a silicon solar cells. The short wavelength response is controlled by the surface recombination, while the response in the long wavelength region may be reduced by the recombination in the bulk (SRH and Auger) and at the rear surface.

In the Auger limit the V_{OC} still depends logarithmically on the concentration factor, but the coefficient is reduced from 1 to $2/3$.

In conclusion, the behaviors of the V_{OC} with respect to the concentration factor depend on the dominant recombination mechanisms. This may be a simple and useful experimental method to investigate the different recombination mechanisms in concentrator solar cells.

Fill Factor

The fill factor FF is defined as:

$$FF = \frac{J_{mp} \cdot V_{mp}}{V_{OC} J_{SC}} \quad (2.61)$$

where J_{mp} and V_{mp} are the current density and the voltage relative to the maximum power point of the I-V curve. The FF depends on the lumped and the shunt resistances. In fact, high series resistance leads to low fill factors. The FF can be expressed as a function of the concentration factor with the approximated formula [21]:

$$FF(C) \approx (FF_{1-sun} + 0.0035 \ln C) \cdot \left(1 - \frac{C J_{SC,1-sun} R_s}{V_{OC}(C)}\right) \quad (2.62)$$

where R_s is the lumped series resistance. The FF decreases with the concentration factor increasing.

Conversion efficiency

The conversion efficiency η is the maximum output power divided by the incoming irradiance P_{inc} (W/m²):

$$\eta = \frac{J_{mp} V_{mp}}{P_{inc} A_{cell}} \quad (2.63)$$

In order to show the dependence from the concentration factor, the efficiency can also be expressed as a function of the V_{OC} and FF:

$$\eta = \frac{J_{SC}(C) V_{OC}(C) FF(C)}{C P_{inc,1-sun} A_{cell}} = \frac{J_{SC,1-sun} V_{OC}(C) FF(C)}{P_{inc,1-sun} A_{cell}} \quad (2.64)$$

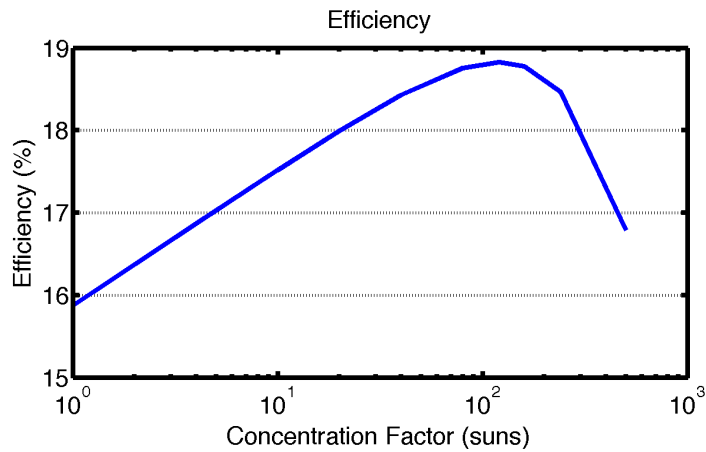


Figure 2.8: Conversion efficiency as a function of the concentration factor of a typical concentrator silicon cell. The efficiency of the solar cell increases with increasing concentration up to reach a maximum, then it is limited by the series resistance losses.

V_{OC} increases logarithmically with the current and thus with the luminous flux. As a consequence, the solar cell efficiency increases with the concentration until the moment that the ohmic drops cause a reduction, as seen in Figure 2.8. The figure shows a typical efficiency-concentration curve of a silicon solar cell. The efficiency increases with increasing concentration due to the increase of the V_{OC} , but in the high-concentration region is limited by the decreasing of the fill factor, which is determined principally by the series resistance R_s . The concentration level, at which the cell efficiency peaks, depends strongly on the series resistance:

$$C_{max}(\eta_{max}) = \frac{q/kT}{J_{SC,1-sun} R_s} \quad (2.65)$$

For $J_{SC,1-sun} = 40 \text{ mA/cm}^2$ and R_s values smaller than $6.6 \times 10^{-3} \Omega \text{ cm}^2$, the maximum efficiency can be reached at about 100 suns.

2.6.4 Mobility and band gap under high-level injection

Under high-level injection condition, the high carriers concentration leads to modifications in the semiconductor band gap value and in the carrier mobility [22]. These two aspects are not negligible in concentrated solar cells and are briefly reviewed in the following.

Band gap narrowing

Due to the high density of generated carriers in high-level injection, the interaction between free electrons and holes and between free carriers and dopants are not negligible. These effects comport an apparent reduction of the band gap of the semiconductor. This is the so called “*band gap narrowing*” (*BGN*) effect. In order to take into account this effect, the intrinsic carrier density n_i should be replaced in Eq. 2.3 by the effective carrier density $n_{i,eff}$:

$$n_{i,eff} = n_i e^{\Delta E_g / kT} \quad (2.66)$$

where ΔE_g is the decrease of the band gap due to the BGN. The BGN comports an effective increase of the intrinsic carrier density [23].

Mobility in high-level injection

The carriers mobility in semiconductors at low-level injection is limited by scattering effects with phonons and impurities. The impurities concentration principally depends on the doping concentration. Therefore an increase in doping concentration leads to a decrease of the carriers mobility. The e/h-mobilities dependence on the doping level is fully predicted by the Masetti model [24].

On the other hand if the solar cell is in high-level injection, the above mentioned scattering effects are unimportant, because, due to the high concentration of both carrier types, the main effect is the carrier-carrier scattering. In this case, the interaction between holes and an electrons depends not only on the concentration but also on the relative direction of motion of both carrier types [25]. For example in rear-contacted concentrator cells most of the carriers are generated at the front side of the solar cell and must diffuse from the front to the rear side of the cell. Therefore, electrons and holes diffuse in the same direction. On the other hand in front n -contact and back p -contact solar cells, electrons and holes diffuse in

opposite directions, as a result of which the carrier-carrier scattering is increased and the mobility reduced.

In this work the *Philips unified mobility model* was used to model the carrier mobility [26] in numerical simulations. The model describes the mobility degradation due to both impurity scattering and carrier-carrier scattering mechanisms.

CHAPTER 3

Fabrication technology of concentrator solar cells

In this chapter the fundamental technology and the fabrication process of the developed front-side contacted small-size Si solar cells are presented. The cells were fabricated by using a CMOS compatible fabrication process. The contact and metal structures are defined by means of photolithography, which is able to define very small structures on the cell front side. The applied fabrication process is here briefly reviewed and described, then a characterization of both materials and process quality in terms of carrier lifetime and surface passivation is presented. Moreover, the fabrication process of an optimized surface texturing process is presented. Surface texturing has proved to be a very important point in our high-efficiency solar cells, since it leads to an increase of the J_{SC} of 10% with respect to the non-textured cells.

3.1 Device structure and technology

The first cell structure developed in this work is a n front-contact and p back-contact solar cell. This cell structure is commonly indicated as *PESC* solar cell (Passivated Emitter Solar Cell) [3]. This kind of cell can be fabricated with only three lithographic steps in a cost-effective processing procedure. Moreover this cell is able to reach high conversion efficiency, over 20%, under concentrated light

[27] [28]. Both characteristics enable high performance/cost ratio and cost-effective power generation.

A schematic cross-section and front view of the solar cell developed in the frame of this work are shown in Figure 3.1. The cell is designed to be applied in the innovative small-size mirrors based concentrator system, described in Ref. [29]. In order to meet the requirement of the concentration system, the cell has an active area of $4 \times 4 \text{ mm}^2$, and it is designed to work under a concentration factor of about 160 Suns.

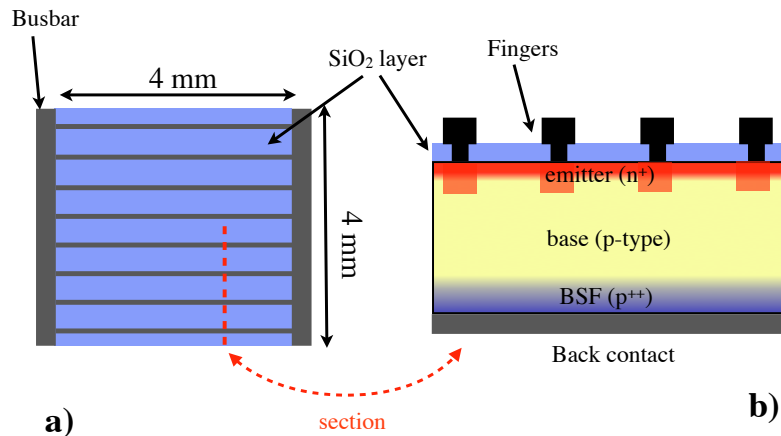


Figure 3.1: Schematic top view (a) and cross section (b) of the basic front n -contact solar cell. Not in scale.

Silicon substrate

The cells were fabricated from both p -type float-zone (FZ) and Czochralski (Cz) silicon wafers. The thickness of the finished solar cells is $280 \mu\text{m}$. Specific base resistivities of 0.5 and $10 \Omega\text{cm}$ were chosen. The chosen specific base resistance range is believed to be an optimum between two effects: maximization of the carrier lifetime in the bulk and reduction of the series resistance losses introduced by the base material. On one hand, the carrier lifetime, which needs to be high in order to enable good collection of the minority carriers at the junction, decreases with increased base doping level and reduced specific base resistance of the base material. On the other hand, the high specific base resistivity results in increased series resistance in the base material, which leads to significant efficiency losses.

Two types of Silicon wafers were used:

- the FZ silicon is high-quality silicon which provides high carrier lifetime also with low-resistance substrate,

- Cz silicon wafers have lower lifetime but they are historically 2 – 3 times lower in cost than corresponding FZ wafers, therefore they are more suitable for mass-production.

The optimum efficiency for such cells is obtained by using silicon with a resistivity in the range 0.2 – 0.5 Ωcm [3]. However, at these low resistivities, the cells show a degradation after light exposure (well known as *LID* effect) [30]. The LID is due to the high oxygen content in CZ wafers and it reduces the conversion efficiency of about 10%. Therefore, low-resistivity Cz silicon is unsuitable for solar cells [31]. On the other hand, solar cells fabricated with Fz silicon do not show any LID effect. For these reasons Fz silicon wafers with resistivity of 0.5 Ωcm and Cz wafers with resistivity of 10 Ωcm were chosen for the high-efficiency solar cells production.

Front side passivation

The cell front side is passivated with a lightly doped and shallow diffused phosphorus emitter. The sheet resistance of the emitter is in the range of 60 - 80 Ω/sq . The emitter diffusion profile was optimized in order to minimize the surface recombination velocity, the contact resistance and the sheet resistance of the doped surface. More details about the emitter junction optimization are reported in the next chapter.

The front surface passivation is further improved by a thin thermally grown silicon dioxide layer. Thereby, the open dangling bonds of the silicon crystal at the surfaces can be saturated and the density of the recombination centers are strongly decreased. The surface recombination velocity of a planar surface can then be reduced from 10^6 cm/s (the value for not-passivated emitters) to 120 cm/s, as demonstrated in Section 3.3.

Antireflection coating

The SiO_2 layer acts as both passivating layer and *Antireflection Coating (ARC)*, due to the low reflectivity of the SiO_2 layer. The SiO_2 layer thickness is optimized to reduce the reflectivity in the whole AM1.5G spectrum. Passivation and Optical properties of the applied oxide layer are investigated in section 3.3.

Surface texturing

With the aim to further reduce the reflection losses, we developed and optimized a surface texturing process. Texturing consists of increasing the “roughening” of the surface with micro-pyramids random distributed. Due to the multiple reflection of

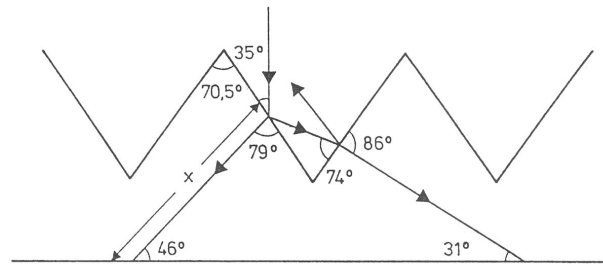


Figure 3.2: Raytracing of the incoming light through a textured surface (taken from [21])

the light at the textured front side of the cell, the probability of coupling light in the cell is increased. Also the optical path through the base of the refracted light is increased and so, the probability of absorption is improved (see Fig.3.2). Figure 3.3 shows the cross section of front-textured solar cells. The texturing was obtained by means of an anisotropic WET etch based on TMAH. Since this texturing process has shown very good results in terms of reflectivity and passivation quality, a more detailed description of the fabrication process and a characterization in terms of total hemispherical reflectance are reported in Section 3.4.

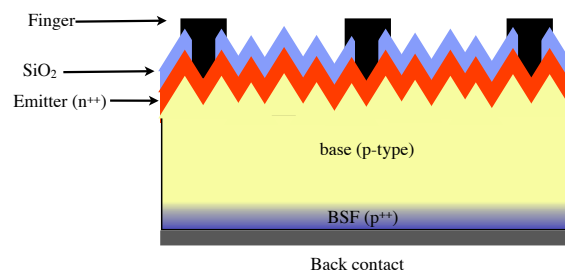


Figure 3.3: Schematic cross section (not in scale) of the front textured solar cell.

Back surface field

The back surface of the cell is doped with Boron and deeply diffused in order to obtain a *Back Surface Field (BSF)*. The presence of the BSF reduces the concentration of the minority carriers at the physical semiconductor surface and thus improves the back surface passivation. Furthermore, the doped back surface reduce the contact resistance between the silicon and the back metal. During the processing two different *p*-type doping techniques to obtain the BSF are tested: the first one is by means of Boron solid source diffusion, the second one is by means of B11 Ion Implantation.

Front contacts and metal grid

The front contacts and the front metal grid are defined by means of two photolithographic steps. The first lithographic step is used to open $6\ \mu\text{m}$ wide contacts on the front SiO_2 layer. The second photolithographic step is used to define the front metal grid (or *fingers*), which are $6 - 7\ \mu\text{m}$ wide and go along the whole cell width.

The front metal prevents a small amount of sunlight from reaching active parts of the cell, reducing conversion efficiency. To minimize this shadowing effect, the fingers must be made as narrow as possible. However, they also need to be as tall as possible in order to preserve a sufficient cross-sectional area keeping low the resistance losses.

Commonly, in solar cells production the front metal is defined by means of screen printing technique. However this technique has the main limit to produce fingers with a minimum width of about $50\ \mu\text{m}$ and low aspect ratio. These characteristics do not match with the requirement for high efficiency small-size concentrator cells.

In this work, the front metal is deposited onto the cell by means of sputtering technique, then the metal fingers are defined by photolithography. This technique, differently from screen printing, allows to obtain very small structures with dimension of few microns and high aspect ratio approaching 1, thus it is very useful to design optimized metal grid for small-size concentrator cells.

Mask splits

Different designs of the front metal grid and of the busbar have been tested. In particular cells with different metallization geometry, and different finger spacing (or finger pitch), have been fabricated and characterized. We focused on two kinds of metal grid, both shown in Figure 3.4: the first grid (the *rectangular grid*) is composed by two busbars and perpendicular fingers, while the second one (the *square grid*) has four busbars and the fingers are displaced as in Fig. 3.4b. Different finger spacings, varying from 100 to $350\ \mu\text{m}$ were tested. Further details about the finger pitch optimization are reported in chapter 4.

3.2 Fabrication process

The cells presented in this work are fabricated in the Microtechnologies Laboratory (MTLab) of the Fondazione Bruno Kessler (Trento, Italy), where a CMOS pilot line is available. In order to get an overview of the process sequence, a scheme of the basic process flow of the front-side contacted cells is summarized in Figure 3.5

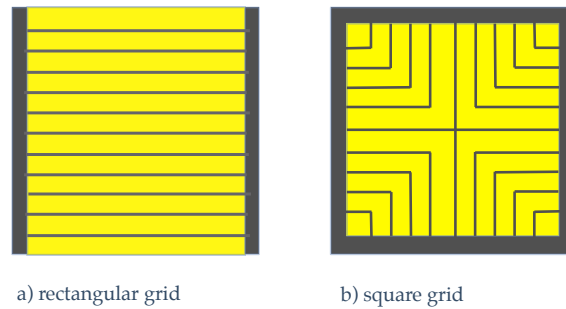


Figure 3.4: Two tested cell geometries: rectangular metallization grid (a) and square metallization grid (b).

and Figure 3.6.

Cleaning and initial oxidation

The process of producing high-efficiency solar cells starts with cleanings steps. Much attention is required for the cleaning of the processed samples. The introduction of contaminated samples into the high temperature diffusion or oxidation process would be fatal to the sample lifetime. Therefore, the so-called *initial cleaning* procedure was applied. This procedure consists of a wet chemical etch by means of hot sulfuric acid followed by a further three-step cleaning procedure, the so-called *RCA Cleaning*. This cleaning is suited to remove both organic and metal particles from the wafer surface.

After the cleaning a silicon dioxide layer on the front and back sides is fabricated by a thermal oxidation at 925°C in N_2 and H_2O atmosphere. The SiO_2 layer is used as a masking layer for the following doping diffusion processes.

Back boron doping

In order to form the BSF, the back cell surface has to be *p*-doped. To perform the doping, first of all the back oxide is stripped by means of a wet SiO_2 etchant. In the whole fabrication process only wet etching are used to open passivating layer. An alternative method which could be used is the *Reactive Ion Etching (RIE)*. The latter however could create damages on silicon surface due to the hitting of high-energetic ions on the cell surface making the passivating properties of the SiO_2 film worse. After the back oxide strip, the surface is boron doped. Two different techniques for boron doping have been tested: the first one uses boron nitride (BN) *solid-source diffusion*, while the second one is performed by means of *ion implantation* of B_{11} isotope. The solid-source diffusion doping is a low-cost

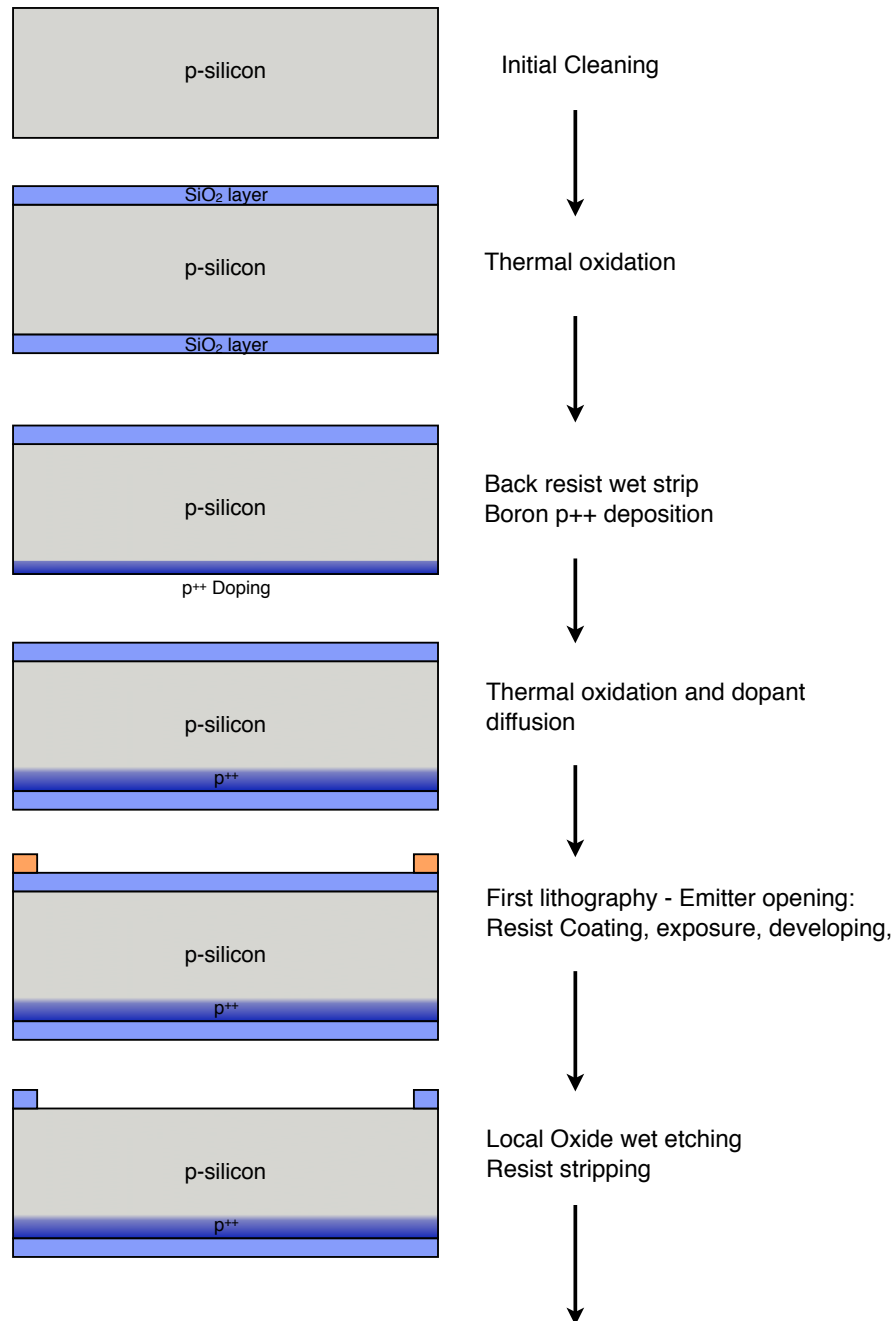


Figure 3.5: Detailed processing steps, from the initial cleaning to front emitter definition

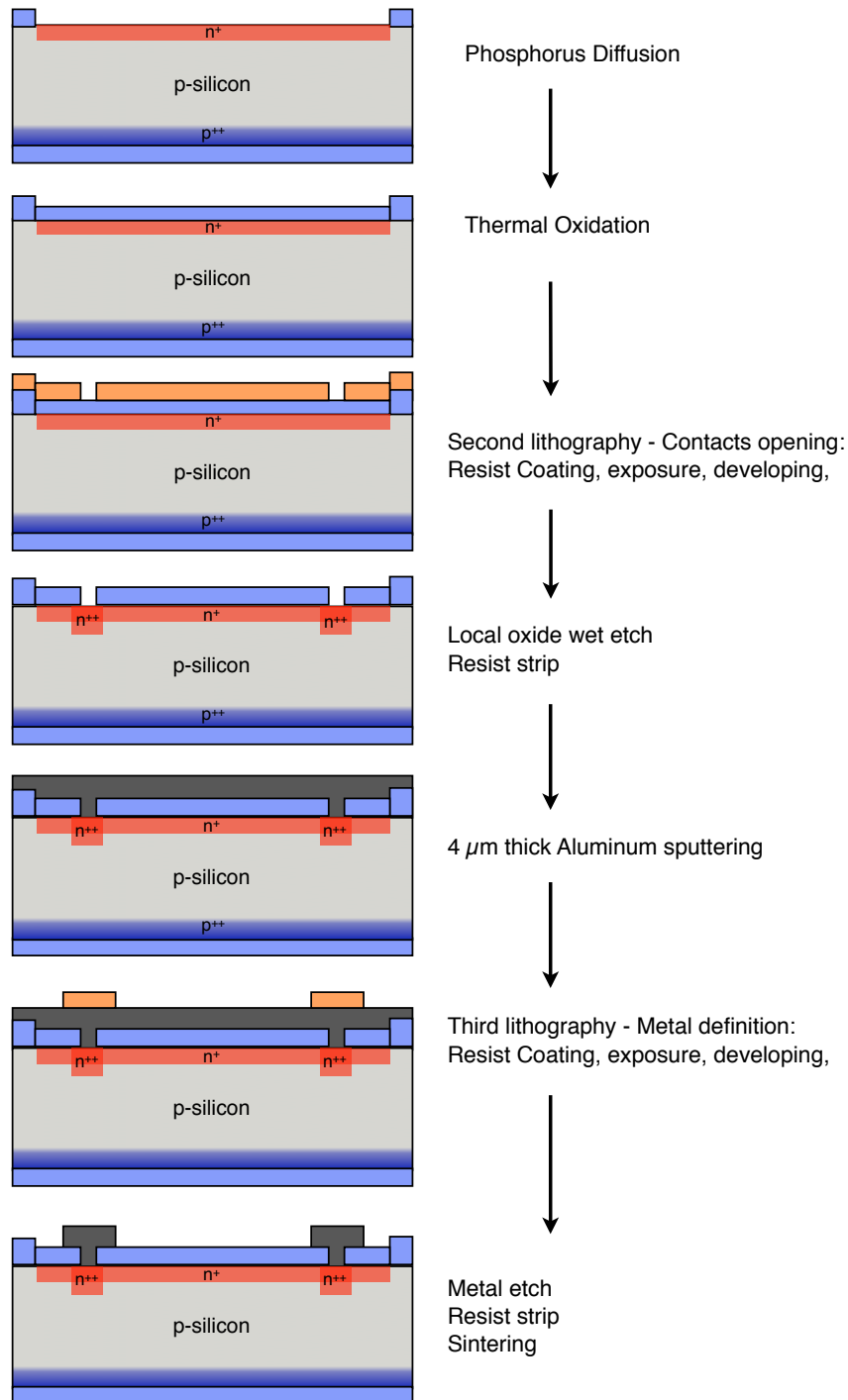


Figure 3.6: Detailed processing steps for the emitter doping, contacts opening and metal structuring.

technique to perform silicon doping. This process is made out of three steps:

- In the first step the back surface of the wafer is placed into the furnace boat-load very close to the BN solid source, then the wafers stack goes under a high temperature thermal treatment. During this treatment a layer of B_2O_3 glass is deposited onto the exposed wafer surface, then the dopant glass which is uniformly coating the silicon wafers undergoes a reduction reaction in the ambient which results in the formation of a thin layer of silicon-boride, Si-B, at the silicon surface.
- Deglaze: After the Si wafers are unloaded from the furnace and the excess un-reacted dopant glass is removed by a HF based wet etcher.
- A further thermal treatment in H_2O ambient is performed to drive in the dopant and to grow a new thin layer of masking oxide. After the drive-in the sheet resistance of the BSF is about $150 \Omega/\text{sq}$.

The second method to perform boron doping uses the ion implantation technique. In order to obtain a sheet resistance of the doped region similar to the one obtained with solid-source doping, we set ion energy at 120 keV with a dose of about $5 \cdot 10^{15}$ ions/cm². Also in this case, after the implant, the wafers are thermal oxidized in order to drive in the dopant. Figure 3.7 shows the Boron doping profile after the implant and thermal diffusion. This profile was measured by means of a SIMS (Secondary Ions Mass Spectroscopy) technique. The peak concentration at the back surface is about 10^{19} cm^{-3} , while the junction depth is at about $1.5 \mu\text{m}$ from the back surface.

Emitter doping and ARC formation

The passivating layer on the front surface is locally open by means of photolithography. The open region defines the active area of the cell. Phosphorus is diffused inside the silicon by means of solid source doping, in the same way which is used for boron doping. During the Phosphorus deposition a thin layer of P-Glass is formed on the cell surface. This layer is removed by means of a chemical wet etch, then a thermal oxidation is performed in order to cover the top surface with a layer 108 nm thick of SiO_2 , which will form the ARC. During the thermal treatment at high temperature the Phosphorus is diffused more deeply inside the silicon and the target sheet resistance of about $70 - 80 \Omega/\text{sq}$ is reached. The final doping profile is strongly influenced by the diffusion of dopant atoms during the thermal treatment. As discussed in Chapter 4.2, the final cell performance strongly dependent on the

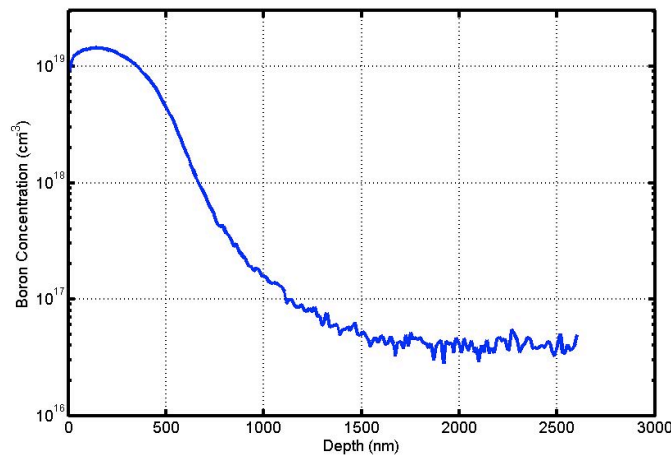


Figure 3.7: Boron doping profile measured with SIMS. The 0 in the x axis corresponds to the back surface. The measured sheet resistance is $150 \Omega/\text{sq}$

emitter doping profile, and shallow emitters are the best for concentrator cells. In order to avoid an excessive emitter depth, the temperature and the time of the thermal oxidation was carefully calibrated. Actually the wafers are processed at 925°C for 20 minutes. This combination allows to obtain both an oxide layer of the right thickness and keeps the junction depth at about $0.8 \mu\text{m}$ from the cell surface. This value is very close to the optimum one, as calculated in Section 4.2. Figure 3.8 shows the SIMS measure of the final and optimized Phosphorous emitter doping profile. The concentration peak is at about $4 \cdot 10^{19} \text{ cm}^{-3}$. An exact knowledge of the real emitter doping profile is fundamental for the cell modeling and simulation.

Contacts opening and selective emitter formation

In order to open the front contact through the passivating layer, a second lithography is performed. The contacts, $6 \mu\text{m}$ wide, are long as the whole cell size. Subsequently a second phosphorus doping is performed in order to form a n^{++} region below the contacts. This high-doped region reduces the contact resistance between the silicon and the metal finger without modifying the optimized emitter junction profile in the optically exposed part of the cell. This method of reducing the contact resistance is known as *selective emitter*. The measured sheet resistance of the n^{++} layer is $45 \Omega/\text{sq}$, about the half of the emitter's.

In standard solar cells with homogenous emitters, the dopant concentration of the emitter is always a compromise. A high n -dopant concentration is required to minimize the resistivity between semiconductor and metal contacts. However, the carriers collecting capability decreases with rising phosphorous concentration,

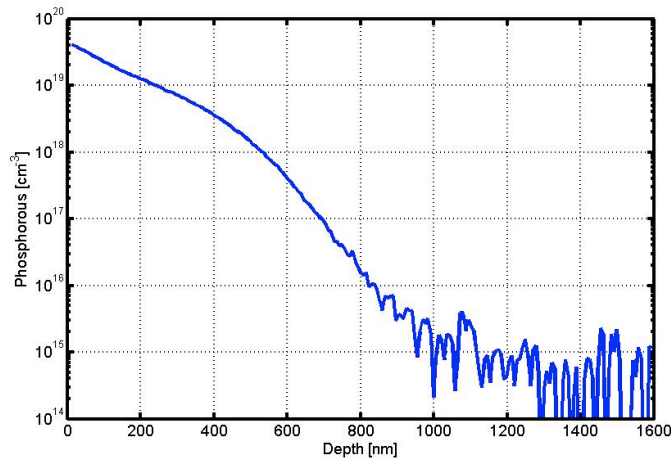


Figure 3.8: Phosphorus doping profile measured with SIMS. The 0 in the x axis correspond to the front cell surface. The emitter sheet resistance is about $70 \Omega/\text{sq}$.

affecting the final performance of the solar cell. Thanks to selective emitter technology, the phosphorous concentration in the emitter can be designed so that only the area of the front side metal grid has a high phosphorous concentration and therefore a low emitter resistivity. The rest of the surface is lower doped so that a large part of the cell can be used for carriers generation and collection. This combines an improved carrier collection performance with very good ohmic contact.

Front metal definition

After the selective emitter formation, a metal layer is deposited onto the cell top surface by means of sputtering. As first, a 20nm thick layer of titanium is sputtered, then a layer of aluminum, 2 or 4 μm thick is deposited. The Ti layer is required to reduce the contact resistance between Al and Si.

The last photolithography defines the metal finger. In the photolithographic mask the finger are 10 μm wide. Due to the high-thickness of the metal layer the finger definition cannot be performed by only chemical wet etching. This is due to the fact that the *under etch effect* during the wet process could strip totally the metal finger as shown in Fig. 3.9.

In order to preserve the fingers, the metal etching is performed in two distinct phases. In the first stage a RIE process is used to thin the metal layer by etching the first 3 μm of metal, then a wet etch complete the Al removal from the cell optical window. Since the last etching process is the wet chemical one, this technique avoids to expose the cell surface to RIE process. After the etch process the final finger

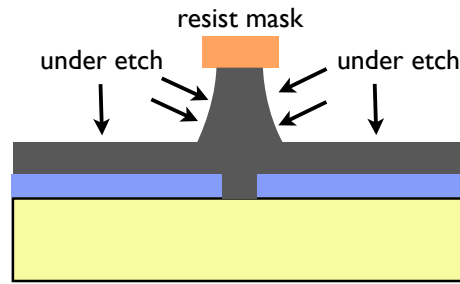


Figure 3.9: Chemical wet etching is isotropic, so the etching progresses in all the direction with the same rate. Consequently the finger is partially etched also at the lateral sides. In this way, since the finger has a high aspect ratio, it can be totally stripped out.

width is about $6 - 7 \mu\text{m}$. A picture of the cell at the end of the process is shown in fig. 3.10.



Figure 3.10: Picture at the optical microscope ($50\times$ magnification) of the cell at the end of the fabrication process.

3.3 Lifetime characterization of materials and fabrication process

As discussed in Section 2.6, the minority carrier lifetime and the surface recombination velocity are the main parameters which determine the performance of a solar cell in terms of conversion efficiency. The lifetime and the surface recombination velocity depend both on the substrate material and on the quality of the fabrication process. In fact, some contaminations introduced during the fabrication process or poor passivated surfaces could strongly affect the lifetime and the surface recombination velocity.

With the aim to characterize the fabrication process and the material quality, the bulk lifetime and the surface recombination velocity have been experimentally measured and the results are presented in this section.

The passivating properties of a passivated n^+ surface are commonly expressed in terms of the emitter saturation current (J_{0e}) [32], which represents the inverse current due to recombination in the whole emitter region. This quantity is an implicit measure of the surface recombination velocity S . The measurement of both the bulk lifetime and the saturation current density of the applied diffusion profile is especially required in Chapter 4 for the optimization of the n^+ front surface diffusion profile. A direct measurement of the surface recombination velocity or of the emitter saturation current density is not possible. It is, however, possible to measure the so-called effective lifetime τ_{eff} of minority carriers, which include both the recombination mechanisms at the surfaces as well as within the bulk. The method presented below is used to determine both the bulk lifetime and the surface saturation current density and it is based on the *photoconductance decay technique* (PCD).

3.3.1 Experimental methods

In order to measure the bulk lifetime and the emitter saturation current density we used the *slope method* technique developed by Kane and Swanson in Ref. [33]. In this technique the effective lifetime of a symmetrical n^+pn^+ test structure is measured. The effective lifetime τ_{eff} introduced in Eqs. 2.31 is the sum of the recombination effects both in the bulk and at the surfaces of the sample. The slope method allow to separate the contributions on the effective lifetime due to the bulk lifetime and to the recombination in the emitter respectively.

We processed a test wafer with both surfaces phosphorus-doped with the same doping recipe as used for the cell production. After the doping the wafer was oxidized in order to grow the SiO_2 ARC layer. A scheme of the test structure is reported in Figure 3.11.

The effective lifetime of the test sample was measured using the photoconductance tool WTC-120 from Sinton Consulting [34]. In this experimental setup, the measured silicon wafer is illuminated by a Xenon flash lamp, which has its spectrum distributed mainly at the wavelengths of 800 to 1000 nm. This near infrared light source allows for a fairly uniform profile of the excess carrier density Δn along the wafer thickness. During the lamp flash, the photoconductance of the measured wafer $\Delta\sigma$ is measured contactlessly by using inductive coupling. At the same time, the light intensity is measured using a reference solar cell, which is placed very

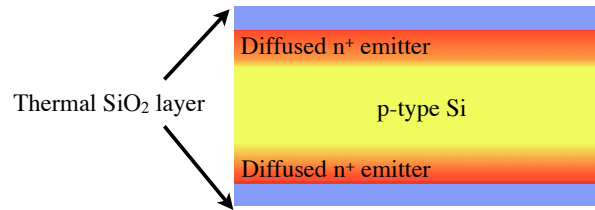


Figure 3.11: Symmetrical n^+pn^+ test structure for bulk lifetime and emitter saturation current density determination. The doping and passivation process was the same used for the cell production.

close to the measured sample. The excess carrier density in the sample is calculated from the measured $\Delta\sigma$ as described in [35]. Knowing the optical properties of the measured sample allows for the determination of the photogeneration rate within the sample measuring the illumination intensity with a monitor solar cell. After determination of both Δn and photogeneration, τ_{eff} can be calculated as a function of Δn . This is possible by applying the quasi-steady-state evaluation method introduced by Sinton et al. [35]. Figure 3.12 shows the measured effective lifetime τ_{eff} as a function of Δn for the tested structure.

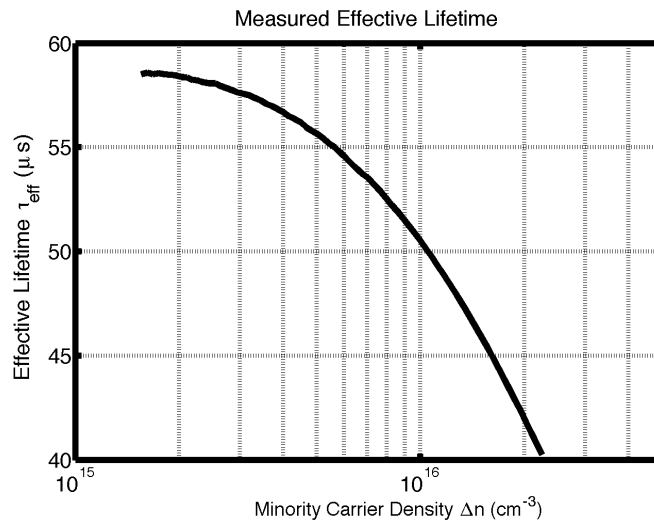


Figure 3.12: Effective lifetime as a function of the minority carrier density measured on the n^+pn^+ test wafer by means of the photoconductance tool WTC-120

From Eqs. 2.31 and 2.31, if the radiative recombination is neglected, the effective lifetime can be expressed as:

$$\frac{1}{\tau_{eff}} = \frac{1}{\tau_{Aug}} + \frac{1}{\tau_{SRH}} + \frac{2S}{W} \quad (3.1)$$

The surface recombination velocity S can be expressed in terms of the emitter saturation current density J_{0e} , by the following equation:

$$S = J_{0e} \frac{\Delta n}{qn_i^2} \quad (3.2)$$

as proposed by Kane and Swanson in [33]. The slope of the inverse lifetime corrected for the Auger recombination is then proportional to $2 \cdot J_{0e}$ according to the equation:

$$\frac{1}{\tau_{eff}} - (C_p + C_n)n^2 = \frac{1}{\tau_{SRH}} + 2J_{0e} \frac{n}{qn_i^2 W} \quad (3.3)$$

where the τ_{Aug} definition of Eq. 2.28 is used.

3.3.2 Experimental results

When $[(1/\tau_{eff}) - (C_p + C_n)n^2]$ is plotted versus n , a straight line results which has a slope proportional to J_{0e} and intercept proportional to τ_{SRH} in the bulk. Thus this method yields a direct measurement of J_{0e} and bulk lifetime starting by an experimental measurement of the effective lifetime τ_{eff} .

Fig. 3.13 reports the fitting procedure for our test sample, while Table 3.1 summarize the measured values of J_{0e} , S and bulk τ_{SRH} of the test sample. The sample temperature during the measurements was set to 24°C. For the calculation of recombination parameters, the intrinsic carrier concentration value n_i is considered equal to $1.0 \times 10^{10} \text{ cm}^{-3}$ and the ambipolar Auger coefficient $C_A = (C_p + C_n) = 1.66 \times 10^{-30}$ was used.

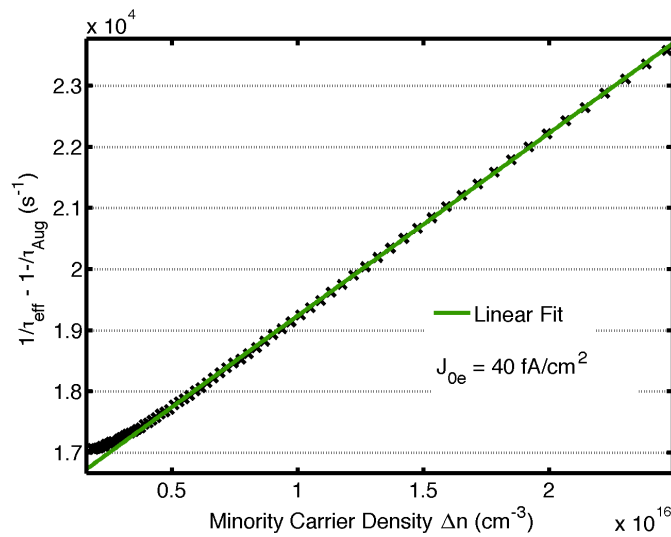


Figure 3.13: Fitting procedure for the determination of τ_{SRH} and J_{0e} on the test sample.

Table 3.1: Experimental values of J_{0e} and bulk lifetime.

Measured Quantity	Symbol	Value
Bulk Lifetime	τ_{SRH}	62 μ s
Emitter Saturation Current Density	J_{0e}	40 fA/cm ²
Surface Recombination Velocity (at $\Delta n = N_A$)	S	120 cm/s

The experimental J_{0e} of the SiO₂ passivated emitter is 40 fA/cm². In general the J_{0e} depends on both the surface passivation and on the emitter doping profile. In particular, increasing the emitter thickness or the surface doping concentration $N_{0,surf}$ tends to increase the J_{0e} , as SRH recombination in the emitter dominates over surface recombination [36]. J_{0e} is lowest for shallow, lightly doped emitters, and it remains small even for emitters with very low $N_{0,surf}$. The measured J_{0e} value is perfectly in line with the values reported in literature for similar devices junction profiles. Typical values of 10 – 100 fA/cm² are commonly reported for oxide passivated emitter with sheet resistance of about 80 Ω /sq [16] [37].

3.4 Texturing optimization and characterization

The surface “texturing” is a process to made the Si surface more “rough”. In this way the surface reflects less the light. In what follows this technique is detailed as well as the way it positively impacts on the cell efficiency. In particular, it is shown that the morphological properties of the textured surface have to be suitably optimized in order to maximize the positive impact of the texturing on the cell efficiency.

In general, the surface texturing can be realized by different techniques: plasma etching, mechanical engraving, and chemical etching. The last one is actually a good compromise between cost and efficiency. Photovoltaic production widely uses potassium hydroxide (KOH) or sodium hydroxide (NaOH) as aqueous texturing solutions. These alkaline solutions etch the silicon anisotropically and form small pyramids on the silicon surface. Hence, light collection is increased by multiple reflections. The technique is based on the dependence of etch rate on the crystallographic orientation with (100) plane as the faster etching plane. KOH and NaOH etching solutions are cost and time efficient but, on the other hand they are highly toxic, pollutants and the potassium and sodium contaminations are detrimental for microelectronic devices. In this work, we optimized a chemical wet texturing process based on tetramethyl ammonium hydroxide ((CH₃)₄NOH, TMAH) to be

efficiently used as antireflective layer in solar cell [38]. The solution combines high etching rate and a good anisotropic etching with a full compatibility with microelectronic technologies. Moreover, TMAH is clean room compatible, nontoxic and easy to handle [39]. TMAH solution also exhibits excellent selectivity towards silicon oxide masks, allowing to use oxide masking to perform selective texturing. Silicon texturing with TMAH solution was proposed for the first time by You [40], In this work we use the recipe proposed by Papet in [41]. He proposed a method based on a solution of TMAH and isopropyl alcohol (IPA) as surfactant.

We studied the influence of the temperature and duration of the etching in order to obtain uniform and reliable pyramidal texturization, optimized for solar cells use. Moreover we verified that the surface passivation is not affected by the texturing process.

3.4.1 Texturing process optimization

Texturing solutions were prepared with deionized water, 2% of TMAH solution and 8% of standard IPA. All etching experiments were carried out using [100]-oriented, *p*-doped (0.5Ωcm) silicon wafers.

We realized a trials set at different temperatures and etching times. The etching time varied from 20 to 50 minutes and the temperature from 70°C to 85°C. During texturing, hydrogen bubbles stuck to the silicon surface and cause a “pseudo-mask” phenomenon. Stuck bubbles suppress the chemical reaction between the etching solution and the silicon in order to create pyramids. The temperature of the solution controls the bubble dimensions and consequently the pyramid dimensions.

We measured the total *hemispherical reflectivity* of the textured surface by means of a spectrophotometer coupled with an integrating sphere. This system is able to measure the reflectivity of not specular reflectors, as in the case of textured surfaces. It is worth to note that the simply normal incidence reflectance is not a reliable parameter to check the effectiveness of the etching process, because a low efficient etching process can strongly decrease the normal incidence reflectance, leaving the total hemispherical reflectance almost unchanged.

The *weighted reflectance (WR)* was calculated normalizing the hemispherical reflectance spectrum (300 – 1100 nm) by the AM1.5G spectrum. In Table 3.2 the WR of the trials are listed, while in Fig. 3.14 the hemispherical reflectance of textured samples versus temperature at an etching time of 30 minutes are reported.

The lowest WR was obtained at 80°C for 30 minutes, and it is equal to 11.1%. This is a very good value compared to the best result reported in literature (13% in [41]). Fig. 3.15 shows two SEM images of textured surfaces obtained respectively

Table 3.2: WR reflectance of Si textured samples versus temperature and etch time

		Temperature (°C)			
		70	75	80	85
Time	20 min.	11.8%	11.8%	11.9%	12.3%
	30 min.	11.8%	11.4%	11.1%	12.3%
	40 min.	12.0%	11.6%	11.5%	12.0%
	50 min.	12.0%	11.6%	11.6%	12.0%

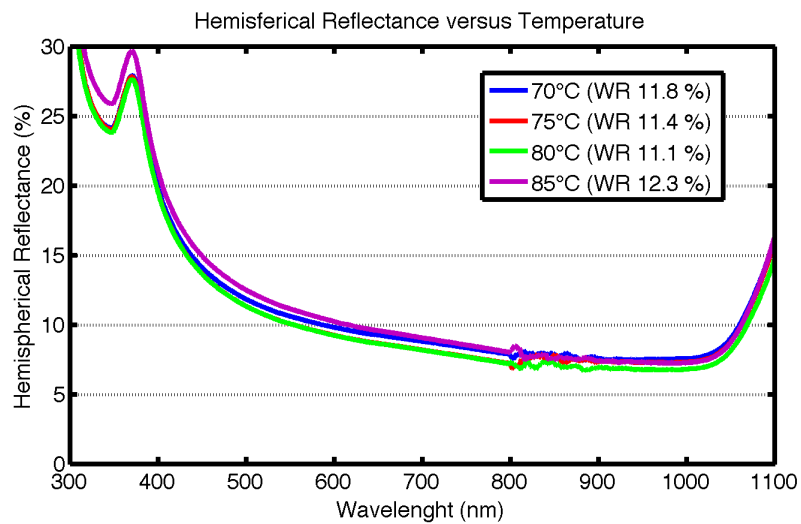


Figure 3.14: Hemispherical reflectance of textured Si wafer. The temperature of the etching process varied from 70°C to 85°C, while the duration was 30 minutes. The best sample was obtained at 80°C where the measured WR is equal to 11.1%.

with the minimum and maximum values of process temperature and duration. It should be noted that when the temperature increases the pyramids dimension also increases.

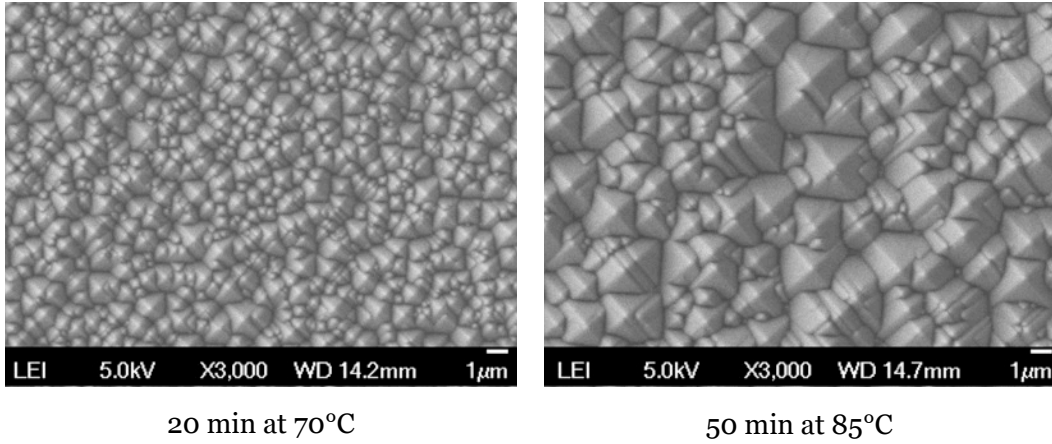


Figure 3.15: SEM images of textured surfaces obtained with different temperature and etch duration. Temperature and time influence the pyramids dimension. In particular, high temperature and high etching time increase the pyramid size.

In order to further reduce the reflectance, the textured surface was oxidized and a SiO_2 layer 108 nm thick was grown. After the SiO_2 ARC growth, the WR of the planar wafer is reduced from 38.0% to 16.8% while the best textured samples with ARC shows a WR of 6.8%. This is a very impressive low result. Figure 3.16 reports the hemispherical reflectance of blank Si wafers with and without texturization compared with the same samples after the SiO_2 ARC growth. In conclusion our texturing process is able to reduce the WR of the cell front surface with SiO_2 ARC from 16.8% to only 6.8%.

3.4.2 Passivating properties of textured surfaces

An antireflective coating should maximize the optical transmission into the solar cell, but it must also act on passivating layer in order to reduce the surface recombination at the n^+ -diffused surface. In order to analyze the passivation properties of our texturing process, we characterized our samples with the *slope method* described in Section 3.3 and the J_{0e} of the n^+ doped textured surface was determined. A symmetrical n^+pn^+ test wafer with both textured surfaces was fabricated in the same way as used for planar sample. Figure 3.17 reports the the effective lifetime corrected for the Auger recombination $((1/\tau_{eff}) - (C_p + C_n)n^2)$ plotted versus the minority carrier density Δn , together with the fit results. The extrapolated value

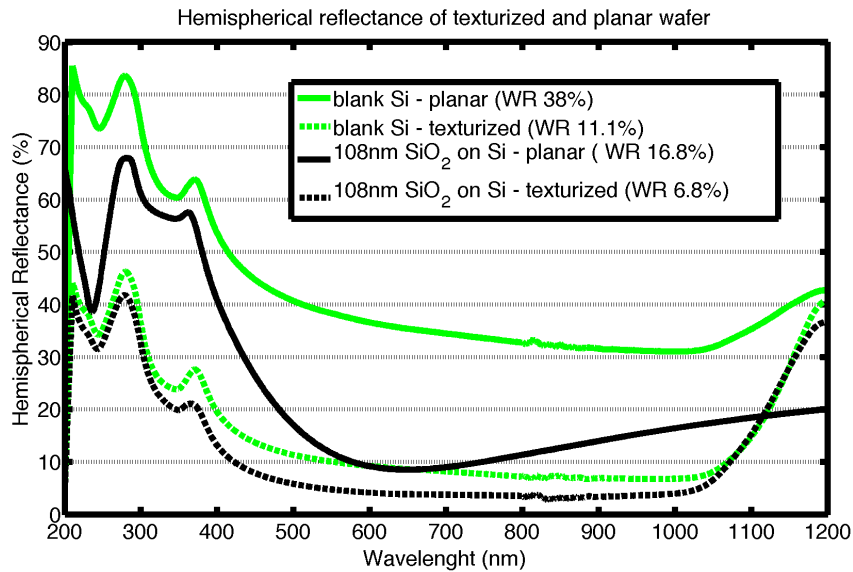


Figure 3.16: Hemispherical reflectance of Si wafers both planar (solid lines) and textured (dotted line), before (solid lines) and after (dotted lines) the SiO_2 ARC growth.

of the J_{0e} is equal to 47 fA/cm^2 comparable with the value of 40 fA/cm^2 obtained for the planar sample.

In conclusion, an effective texturing process based on TMAH wet etch was optimized and characterized. Textured surfaces, coupled with a SiO_2 passivating layer, show both optimal optical properties (WR 6.8%) and good passivating characteristics.

3.4.3 Textured solar cell fabrication

The texturing process was integrated in the fabrication process of the solar cells in order to obtain solar cells with textured front surface. The texturing was performed after the first lithographic mask (the last step in Fig. 3.5), just before the emitter Phosphorus doping. In this way, only the active cell area was textured, while the surface below the busbars remains planar. Using this method no further lithography masks are added to the process. However, due to roughness of the silicon surface, when the metal finger were fabricated on the front surface, a bad adherence of the metal finger to the textured surface was observed. This is due to the fact that the finger thickness is comparable with the pyramids height. The adherence problems carried to fingers detachment and braking, as shown in Fig. 3.18.

In order to preserve the finger continuity, a *Selective texturing* was introduced in the fabrication process: a new lithographic mask was used, which allows to texture

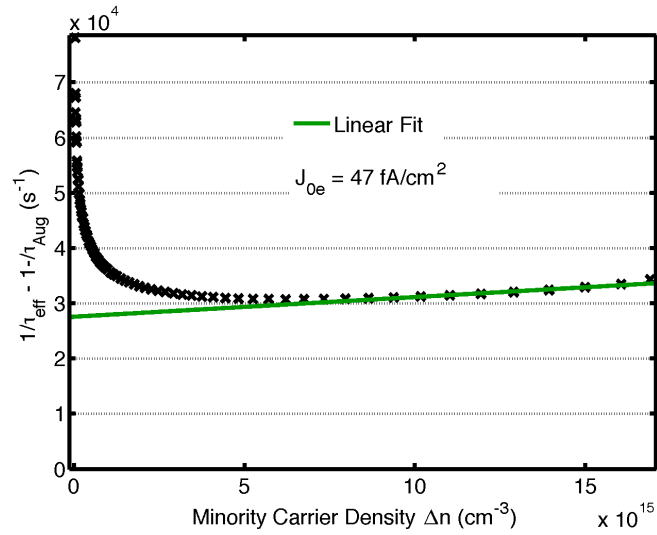


Figure 3.17: Fitting procedure for the determination of τ_{SRH} and J_{0e} of the textured symmetrical test sample.

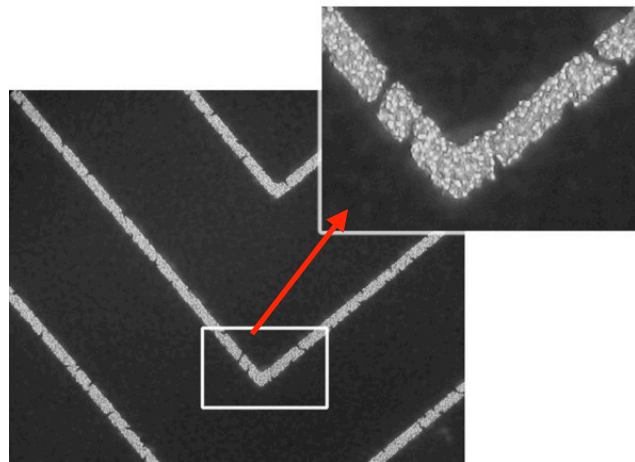


Figure 3.18: Interrupted metal fingers onto textured surface.

only the cell surface between the metal fingers, while the silicon surface below metal structures remains planar as shown in the cell scheme of Fig. 3.19. In this way both the low optical reflectivity of texturing and finger integrity are preserved. Figure 3.20 shows a particular of a cell with selective texturing: after the texturing (a) and at the end of the fabrication process (b).

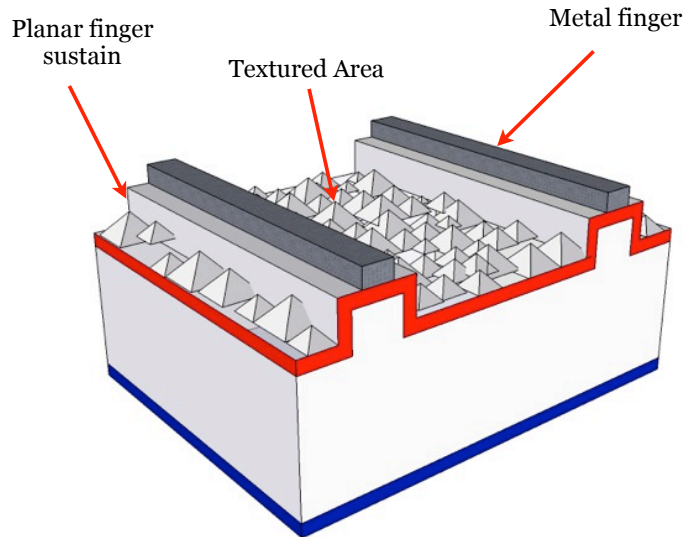


Figure 3.19: Scheme of solar cell with selective texturing (not in scale). The only area being textured is the area between the metal fingers, while under the finger the surface is planar.

3.5 Fabrication technology of deep-grooved contacts and holes

The conventional front-side contacted cell, discussed earlier, can be considered a two-dimensional device, because all the structures are defined on the plane of the cell front surface. Therefore, a conventional “planar fabrication process” can be used for the cell production.

In this work, in addition to a front-side contacted cell design, two innovative cell concepts are proposed. Both the concepts are provided with “three-dimensional” structures, such as deep-grooved holes, which make the cell similar to a MEMS device.

The first concept is based on the design of a conventional front-side contacted cells, in which deep-grooved holes are developed on the back side of the cell and doped with boron. The cell concept is named *DEPC* (Deep-Etched P-type Con-

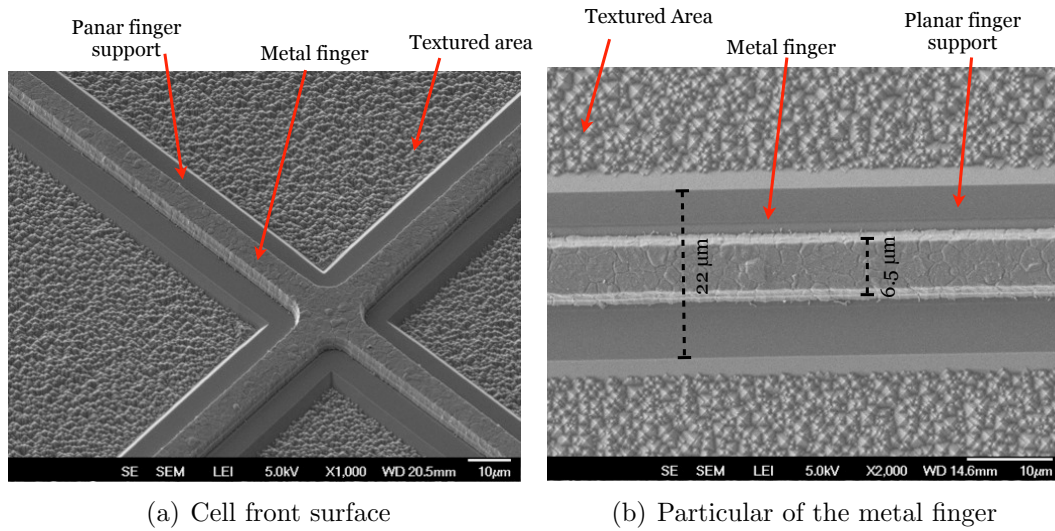


Figure 3.20: Two SEM pictures of solar cells with selective texturing at the end of the fabrication process

tacts) cell and it is represented in Fig. 3.21(a). In Section 4.4.4, it is shown that this design is effective in reducing the resistance losses in the base and in increasing the short circuit current produced by the cell, leading to higher conversion efficiency under concentrated light.

From the technological point of view, the deep-grooved contacts consist of a hole matrix, which is deeply-etched in the silicon substrate starting from the back surface. Subsequently, the internal side of the holes is boron-doped by means of solid-source diffusion.

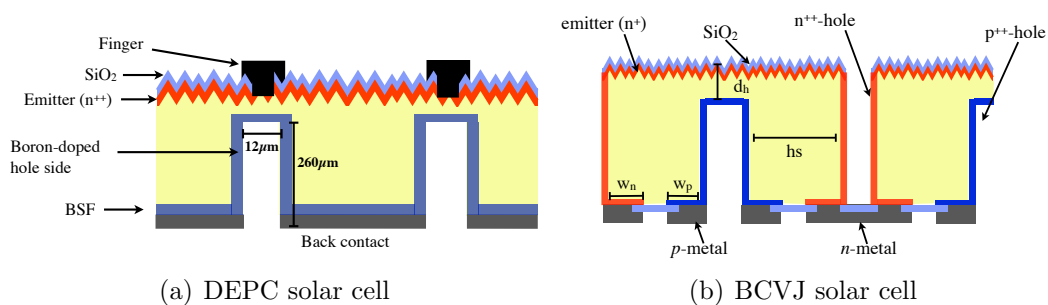


Figure 3.21: The two innovative cell designs proposed in this work. Both the cells are provided with “three-dimensional” structures, which consist in deep-grooved holes that pass-through the silicon substrate.

The second cell concept is named BCVJ cell (Back-Contacted Vertical-Junction) and it is introduced and deeply discussed in Chapter 7. The BCVJ cell is a back-contacted cell, which is also provided with deep-grooved holes like the DEPC cell.

However, differently from the latter, the BCVJ cell has deep-etched holes alternately doped with boron and phosphorus (see Fig. 3.21b). The n -doped holes pass through the silicon substrate and wrap the front cell surface to contacts on the back surface, while the p -doped holes stop at $20\ \mu\text{m}$ from the cell top surface and are contacted to the back contacts. In this way a radial vertical junction is formed between the p -hole and the n -hole.

Both the new cell concepts are provided with deep-grooved holes. These structures should have very high aspect ratio, since the depth should be comparable with the cell thickness ($\sim 280\ \mu\text{m}$) and the diameter should be kept as small as possible.

3.5.1 Silicon deep etch technology

From the technological point of view, the holes are fabricated by means of a *deep reactive-ion etching process (DRIE)*. DRIE is a highly anisotropic etch process used to create deep penetration, steep-sided holes and trenches in silicon wafers, typically with high aspect ratios. It was developed for MEMS device fabrication, which require these features, but is also used for creating through silicon via's (TSV) in advanced 3D wafer level packaging technology [42].

The used technology is based on the so-called *Bosch process* [43], which alternates repeatedly between two modes to achieve nearly vertical structures:

1. A standard, nearly isotropic plasma etch. The plasma contains some ions, which attack the wafer from a nearly vertical direction, and a chemical silicon etchant (SF_6).
2. Deposition of a chemically inert passivation layer (C_4F_8), which yields a substance similar to teflon.

Each phase lasts for several seconds. The passivation layer protects the entire substrate from further chemical attack and prevents further etching. However, during the etching phase, the directional ions that bombard the substrate attack the passivation layer at the bottom of the trench (but not along the sides). They collide with it and sputter it off, exposing the substrate to the chemical etchant. These etch/deposit steps are repeated many times over resulting in a large number of very small isotropic etch steps taking place only at the bottom of the etched structure. The two-phase process causes the sidewalls to undulate with an amplitude of about $100 - 500\ \text{nm}$. The cycle time can be adjusted: short cycles yield smoother walls, and long cycles yield a higher etch rate. For deep etches thick photoresist and thick silicon dioxide films must be used for masking. Since the resist is etched during

the process (although with smaller etching rate than silicon) there is a limit in the achievable hole depth.

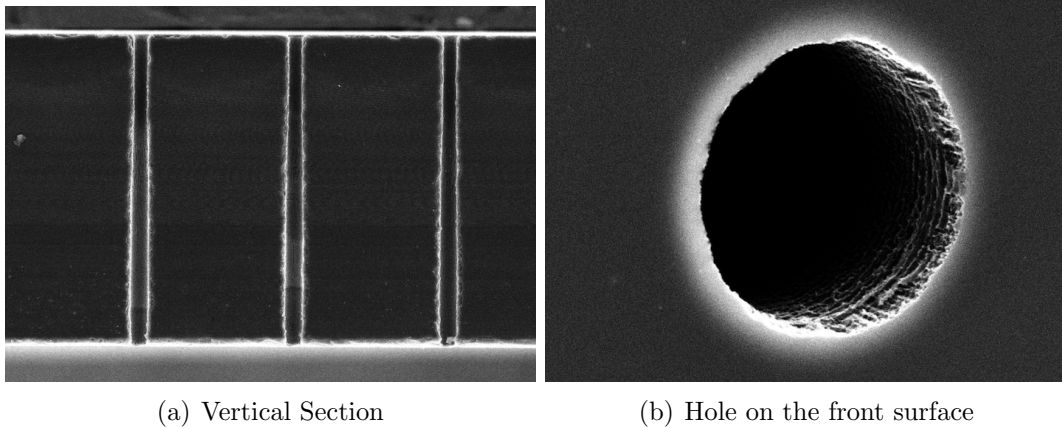


Figure 3.22: SEM pictures of silicon pass-through holes fabricated by means of DRIE process. Vertical section (a) and view of the front wafer surface (b). The holes are $12\ \mu\text{m}$ in diameter and $280\ \mu\text{m}$ deep.

Figure 3.22(a) shows the section of a hole that pass-through a $280\ \mu\text{m}$ thick wafer, while in Fig. 3.22(b) the undulating internal sidewall of the etched holes is visible. The diameter of the deep-etched holes fabricate in this work is equal to $12\ \mu\text{m}$. This is the lowest value achievable with this technique, without reducing the hole depth.

CHAPTER 4

Modeling and simulation of concentrator Si solar cells

In this chapter an exhaustive modeling of solar cells is presented with the aim to investigate the dominating physical effects of the concentrator silicon solar cells developed in this work. Two different methods have been used to carry out the modeling. As first approach, an analytical model, describing the cell under concentrated light, was developed. In such a model, the effects of the resistive losses and of the recombination mechanisms in a silicon cell have been investigated. By means of this model, a co-optimization of the front metal grid and of the emitter doping profile was performed. The co-optimization procedure led to determine a set of design rules in terms of emitter doping and metal grid geometry, which optimize the solar cell conversion efficiency under concentrated light. The analytical model has the advantage to allow a deep understanding of the physics of the device and at the same time it requires a small computational effort, yet with several approximations, which limit the modeling of the cell under high-concentrated light. These approximations have been overcome in the second approach, where electrical and optical numerical simulations of the device were used in order to investigate some high-level injection effects in the cell substrate. The short circuit current in high-level injection conditions resulted non-linear with the incident irradiance. The non-linearity effect was deeply investigated and the numerical simulations were exploited to investigate the cell performance trends with respect to the substrate resistivity and thickness, showing that the efficiency of

the front-contacted solar cell under concentrated light is maximized by using thin and low-resistivity substrates. Finally a new solar cell concept, based on deep-grooved contacts on the rear side of the cell (DEPC cells) is presented and discussed.

4.1 Series resistance in concentrator Si solar cells

The main effects limiting the efficiency of 1-sun silicon solar cells are the recombination currents which occur in the device. In CPV devices, apart from the recombination losses, the intrinsic series resistance affects the cell performance. In fact, cells under concentrated light are high-current and low-voltage electrical power generators. It should be noted that under 100 suns a cell produces a current density of about 3–4 Ampere/cm². Therefore, the high current density could lead to more important efficiency losses with respect to the case of 1-sun solar cells. For this reason some cell parameters, such as the metal-grid geometry, the emitter doping profile and base resistivity, play a key role in developing concentrator cell design.

In the multi-diode equivalent circuit, shown in Fig. 2.6, the series resistance losses are represented by a lumped series resistance R_s . It is a very useful first-order approximation which can be used to approach the cell design optimization.

The total series resistance R_s consists of the summation of many components: the series resistance of the base, the emitter, the metal and at the contacts region, as shown in Figure 4.1. In this section the analytical expressions for the series resistance components of the front-side contacted cell are given.

Resistance in the base

In front-side contacted cells the majority carriers must diffuse from the front side, where most of the photons are absorbed, to the rear side in order to be collected by the rear contact. Therefore, the specific base resistivity introduces losses in the carrier transport. The resulting series resistance is:

$$R_b = \rho \frac{W_b}{A_c} \quad (4.1)$$

where ρ is the specific resistance of the base, W_b is the thickness of the cell and A_c is the active area of the cell. The series resistance weighted by the active cell area r_b is given in $\Omega \text{ cm}^2$ and it is equal to:

$$r_b = \rho W_b \quad (4.2)$$

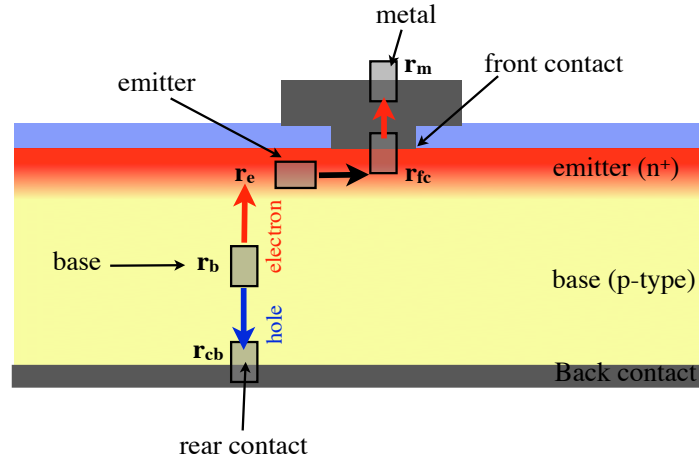


Figure 4.1: The different components of the total lumped series resistance used to model the resistance losses in the solar cell.

In order to minimize the base resistance, both the thickness and the wafer resistivity should be kept low.

Resistance of the emitter

In the emitter, the carriers flow from the front surface into the metal finger. The series resistance of the emitter (n^+ -diffusion on the front side), can be calculated by considering a distributed resistance model. With reference to Figure 4.2 the “reference cell” used for the calculation is colored in red, the finger spacing is indicated with S_f and L represents the finger width (i.e. the cell length). The lateral current, flowing in the emitter, is constant along the x axis and it is 0 at $y = 0$. The current can be expressed as a function of y as:

$$I(y) = J_{ph} \frac{L}{2} y \quad (4.3)$$

The resistance in the infinitesimal region dy along the emitter is equal to:

$$dR_e = r_{sh,e} \frac{2}{L} dy \quad (4.4)$$

where uniform photogenerated current J_{ph} is assumed and $r_{sh,e}$ is the emitter sheet resistance. The ohmic loss P_e in the emitter is determined by the integral:

$$\begin{aligned} P_e &= 2 \int_0^{\frac{S_f}{2}} I^2(y) dR_e = 2 \int_0^{\frac{S_f}{2}} J_{ph}^2 \frac{L^2}{4} y^2 r_{sh,e} \frac{2}{L} dy \\ &= \frac{1}{24} J_{ph}^2 r_{sh,e} L S_f^3 \end{aligned} \quad (4.5)$$

Therefore the lumped emitter resistance can be determined by considering the total current in the reference cell $2I(\frac{S_f}{2})$:

$$R_e = \frac{P_e}{(2I(\frac{S_f}{2}))^2} = \frac{1}{6} r_{sh,e} \frac{S_f}{L} \quad (4.6)$$

and the emitter series resistance weighted for the area is given by:

$$r_e = \frac{1}{12} r_{sh,e} S_f^2 \quad (4.7)$$

It should be noted that the emitter resistance increases with the square of the finger spacing S_f , therefore the metal grid should be accurately designed to minimize the resistance losses.

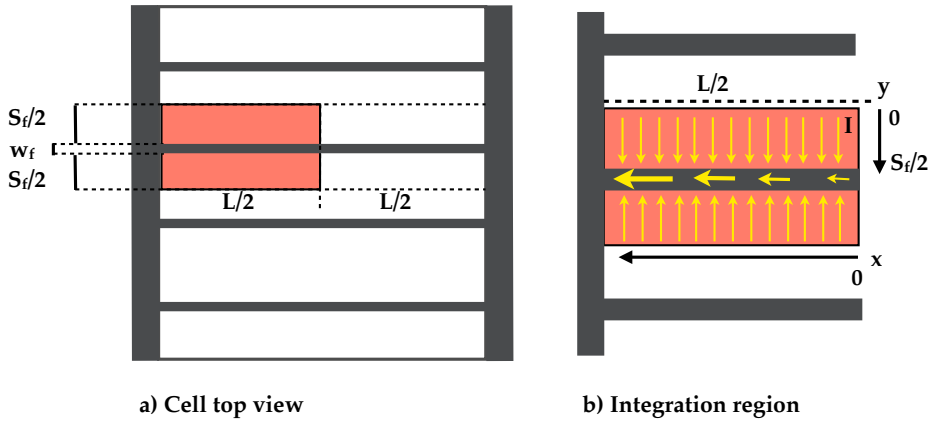


Figure 4.2: Scheme for emitter resistance estimation. In a) the top view of the cell with rectangular metal grid is sketched. The area highlighted in red is the integration region used for the calculation. In b) the current flowing through the emitter into the metal finger is represented.

Resistance of the metal grid

The ohmic losses due to the metal fingers can be analytically described by using the same method as used before for the sheet resistance analysis. With reference to Figure 4.2, the current in the finger is equal to zero at $\frac{L}{2}$, while along the finger the current $I(x)$ is equal to:

$$I(x) = J_{ph} S_f x \quad (4.8)$$

The resistance of the infinitesimal region dx along the finger and the total ohmic power losses P_m are equal respectively to

$$dR_m = \frac{\rho_m}{w_f h_f} dx \quad (4.9)$$

$$\begin{aligned}
P_m &= \int_0^{\frac{L}{2}} I^2(x) dR_m = \int_0^{\frac{L}{2}} J_{ph}^2 S_f^2 x^2 \frac{\rho_m}{w_f h_f} dx \\
&= \frac{1}{24} J_{ph}^2 S_f^2 \frac{\rho_m}{w_f h_f} L^3
\end{aligned} \tag{4.10}$$

Finally, the metal resistance R_m and the metal resistance weighted for the area r_m are given respectively by:

$$R_m = \frac{1}{6} \frac{\rho_m L}{w_f h_f}, \tag{4.11}$$

$$r_m = \frac{1}{12} \frac{\rho_m L^2 S_f}{w_f h_f}. \tag{4.12}$$

Contact resistance

The specific contact resistance ρ_c between the semiconductor and the metal is a function of the dopant concentration at the surface of the semiconductor $N_{0,surf}$. In particular, as the doping concentration increase the contact resistance ρ_c decreases. The latter can not be calculated analytically. However, the contact resistance between n -doped silicon and titanium has been measured by Swirhun as a function of phosphorus concentration in Ref.[44] and is approximately described by the following equation:

$$\rho_{ce} = \exp \left\{ a_0 + a_1 \ln \left(\frac{N_{0,surf}}{10^{18}} \right) + a_2 \left[\ln \left(\frac{N_{0,surf}}{10^{18}} \right) \right]^2 \right\} \tag{4.13}$$

where $a_0 = -1.96197$, $a_1 = -3.41859$, $a_2 = 0.187692$ and ρ_{ce} is given in Ωcm^2 . A plot of this function is given in Figure 4.3.

The contact resistance is obtained by dividing ρ_{ce} with the contact area (assumed equal to the finger area). Finally, the front contact resistance weighted for the area is given by

$$r_{ce} = \frac{\rho_{ce} S_f}{w_f}. \tag{4.14}$$

The contact resistance depends linearly on the finger spacing.

The total resistance of the solar cell is finally described by the sum of all the series resistance components:

$$\begin{aligned}
r_{total} &= r_b + r_{cb} + r_{ce} + r_e + r_m \\
r_{total} &= \rho W_b + \rho_{cb} + \frac{\rho_{ce} S_f}{w_f} + \frac{1}{12} r_{sh,e} S_f^2 + \frac{1}{12} \frac{\rho_m L^2 S_f}{w_f h_f}
\end{aligned} \tag{4.15}$$

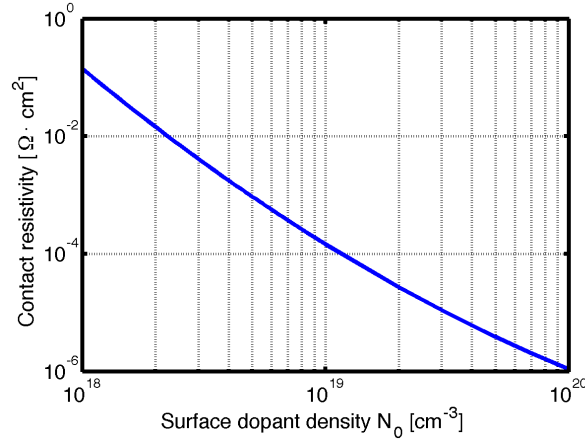


Figure 4.3: Contact resistance (in Ωcm^2) between silicon and titanium as a function of the surface phosphorus concentration density $N_{0,surf}$.

4.2 Co-optimization of the emitter and of the metal grid using a quasi-analytical approach

In order to optimize the design of the front-side contacted solar cells, the total resistance should be reduced at the minimum value. As shown in Eqs. 4.7, 4.12 and 4.14, the emitter resistance, the contact resistance and the metal grid resistance depend on the finger spacing S_f . This could indicate that S_f should be reduced to the minimum. However, low S_f comports high metal-covered area on the cell front surface and, as a consequence, increases the light shadowing.

At the same time, the emitter sheet resistance should be minimized in order to reduce both the emitter and the contact resistance, which depend on $N_{0,surf}$. However, also in this case, high emitter doping has the drawback to increase the recombination rate in the emitter region.

For these reasons a compromise between metal shadowing, series resistance and recombination current must be found in order to maximize the conversion efficiency, by optimizing simultaneously the emitter doping profile and the metal grid design.

The optimization of the emitter and the metal grid should not be done in isolation, since they are intimately related to each others, in fact:

- the finger spacing S_f and the emitter doping influence both the emitter and the metal grid resistances;
- the finger spacing S_f and the emitter doping concentration both participate to determine the recombination current into the emitter. In particular, high-doped emitter and high metallization area (narrow finger spacing)

both increase the recombination current. The latter effect is due because high-recombination occur at the metal-contact regions.

In order to take into account these correlation effects, a simultaneously co-optimization of the emitter doping profile and of the metal grid must be performed. In this section a quasi-analytical method is presented with the aim to carry out the co-optimization and to determine the optimum design parameter of both emitter doping profile and finger spacing.

In the past years several studies have been published about the optimization of the emitter doping profile and of the front metal grid of silicon solar cells working under 1 sun [45] [46]. These studies indicate that thick emitters with dopant surface density in the range $(10^{18} - 10^{19}) \text{ cm}^{-3}$ are the best choice for devices with passivated emitters. However, these values are strictly valid under 1-sun illumination conditions. In this work this procedure is extended to silicon solar cells working under concentrated light from 1 to 150 suns. This new procedure allows to obtain design rules for maximizing the conversion efficiency for a given concentration factor. Moreover, the model can be easily extended to evaluate the effects on the conversion efficiency of different metal grids or emitter structures.

4.2.1 Co-optimization model

In the proposed model the solar cell under concentrated light is described by using a lumped equivalent network with a single diode, a parasitic series resistance and a shunt conductance as in the following:

$$J = C(J_{ph} - J_{lost}) - J_0 \left(e^{\frac{qV_j}{kT}} - 1 \right) + \frac{V_j}{r_{sh}} \quad (4.16)$$

$$V_j = V + Jr_s(F) \quad (4.17)$$

where C is the concentration factor and V_j is the voltage at the junction. The saturation current density J_0 reflects the losses when the device is forward biased, while J_{lost} , introduced by King in [36] represents the loss of photogenerated current under short-circuit conditions, which means, the difference between the number of electron-hole pairs photogenerated within the emitter and the actual number of minority carriers collected at the pn junction.

For simplicity, in Eq. 4.16, the dark current is assumed to be defined by a single exponential with ideality factor equal to 1, which corresponds to low-level injection condition. This assumption is well justified in this emitter optimization procedure because the high doped emitter is anyway in low injection condition, also under concentrated light. In fact, as shown in table 2.1 both the SRH and the

surface recombinations under high-level injection have ideality factor equal to 1 in the emitter region.

The model aims to estimate the cell conversion efficiency as a function of the independent variables: concentration factor C ; finger spacing S_f and emitter doping profile. In order to calculate I-V curve of the cell as a function of these independent variable, two more assumption are made:

- The doping concentration density as a function of the depth is described by means of the *complementary error function* ($erfc$). This function fits very well the doping profile in the emitter, when it is doped by means of solid source diffusion. Figure 4.4 shows the experimental emitter doping profile fitted by means of the $erfc$ function. With this assumption, the emitter profile is completely described, for a given substrate, by two parameters: the *emitter thickness* (or junction depth) E_t and the *surface doping concentration* ($N_{0,surf}$).

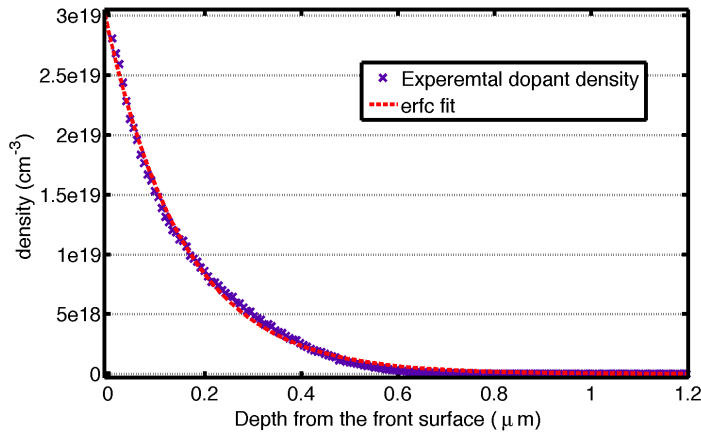


Figure 4.4: Emitter doping profile experimental measured (blue cruces) and the $erfc$ function used to fit the doping profile (red dotted line).

- The cell is represented by the superposition of two regions: one with passivated surface and the other on with metal-contacted surface (see Fig. 4.5). Therefore, the photogenerated current and the recombination current are assumed to be a combination of the contributions from the passivated and non-passivated metal-covered fractions of the cell. The ratio between the passivated and non-passivated fraction of the cell is indicated by means of the *transparency factor* F , which indicates the percentage of the front surface area not covered by metal and it is related to the finger spacing and finger

width by means of:

$$F = 1 - \frac{w_f}{S_f} \quad (4.18)$$

whit w_f and S_f defined in Fig. 4.2.

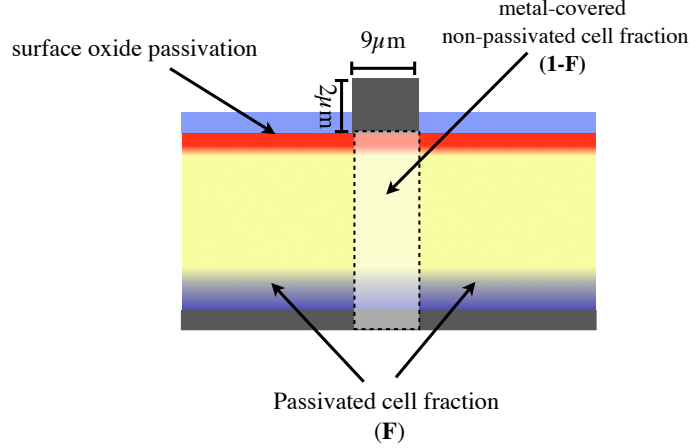


Figure 4.5: In the model the cell is divided in two regions. The first one represents the light exposed fraction of the cell area with oxide passivated front surface, the second one represents the metal-covered area without surface passivation.

According to the above assumptions the saturation currents J_0 and the lost photogenerated current J_{lost} in Eq. 4.16 can be expressed as the sum of the contributions from the passivated and non-passivated surfaces:

$$J_0(F) = F J_0^{pas} + (1 - F) J_0^{n-pas} \quad (4.19)$$

$$J_{lost}(F) = F J_{lost}^{pas} + (1 - F) J_{lost}^{n-pas} \quad (4.20)$$

where J_0^{pas} and J_0^{n-pas} are the dark saturation currents for the passivated and the non-passivated surface, respectively.

In this way the current-voltage characteristics of the solar cell in Eq. 4.16 can be expressed as a function of the concentration factor C and the design parameters F , E_t and $N_{0,surf}$ as in the following:

$$J = C \left(J_{ph} - [F J_{lost}^{pas} + (1 - F) J_{lost}^{n-pas}] \right) F - \left(F J_0^{pas} + (1 - F) J_0^{n-pas} \right) \left(e^{\frac{qV_j}{kT}} - 1 \right) + \frac{V_j}{r_{sh}} \quad (4.21)$$

The characteristics recombination current densities J_0^{pas} and J_{lost} for both passivated and non-passivated surfaces depend also upon the doping profile of the emitter. An

analytical estimation of the recombination currents as functions of $N_{0,surf}$ and E_t is not possible, therefore we used numerical simulations of one-dimensional electrons and holes transport to estimate them.

Numerical Evaluation of J_0 and J_{lost}

In order to take into account the dependence of the current densities J_0^{pas} , J_0^{n-pas} , J_{lost}^{pas} and J_{lost}^{n-pas} on E_t and $N_{0,surf}$, we used the analysis program *PC-1D*, which allows for an analysis of thousands of emitter profiles in a small computational time [47].

The current densities have been calculated in a simulation domain of E_t (in the range $0.1 - 2 \mu\text{ m}$) and $N_{0,surf}$ (in the range $10^{18} - 10^{20} \text{ cm}^{-3}$). A self-consistent set of parameters for energy band-gap narrowing, lifetime, mobility and surface recombination velocity [19] has also been included into the analysis:

- Illumination: the global AM1.5G spectrum is used to calculate J_{ph} , and J_{lost} current densities.
- Front surface recombination velocity. The front surface recombination velocity in the emitter region is a function of the surface doping concentration. The experimental values for a thermally grown silicon dioxide were used for the passivated area [37], while the kinetic limit was used for the fractional areas with an ohmic metal contact:

$$S_{pass} = N_{0,surf} \times 10^{-16} \text{ cm/s} \quad (4.22)$$

$$S_{n-pass} = 3 \times 10^6 \text{ cm/s} \quad (4.23)$$

- Apparent electrical band gap narrowing [37][48]:

$$\Delta E_g^{app}(N_D) = 14\text{mV} \ln \left(\frac{N_D}{1.4 \cdot 10^{17}} \right) \quad (4.24)$$

and ΔE_g^{app} is 0 for $N_D < 1.4 \cdot 10^{17}$.

- Intrinsic carrier density $n_i = 8.66 \cdot 10^9 \text{ cm}^{-3}$ at 300°C [36] [49].
- A minority-carrier mobility model including the dependence with respect to the doping concentration was used [50].

Other cell parameters like the surface coating, bulk lifetime, resistivity and thickness should be tuned depending on the specific investigated cell. In this optimization we

Table 4.1: Cell parameters used in the model and in numerical simulations

Parameter	Value
Cell area	$4 \times 4 \text{ mm}^2$
Cell thickness	$280 \text{ }\mu\text{m}$
Substrate resistivity	$0.5 \text{ }\Omega\text{cm}$
Metal finger width	$10 \text{ }\mu\text{m}$
Metal finger thickness	$2 \text{ }\mu\text{m}$

used the parameters shown in Table 4.1 in order to describe the front-side contacted solar cells developed in our laboratories.

The contour plots of J_0^{pas} and J_0^{n-pas} as a function of the surface dopant density $N_{0,surf}$ and the emitter thickness E_t , are given in Figure 4.6. It should be noted that the J_0 has opposite trends for passivated and unpassivated surfaces. In the first case J_0^{pas} increases with the increasing of doping density and emitter thickness, while in the latter, J_0^{n-pas} decreases with doping concentration increasing. The result is in accord with previous studies [46] [51].

A rule of thumb to optimize the emitter region is to make the saturation current densities as small as possible, but it cannot be applied straightforwardly because the surface of the solar cells consists of both passivated and non-passivated regions. The plot of the total J_0 that corresponds to a fractional unpassivated area of 10% ($F = 0.9$) is shown in Fig. 4.6 (c), and it has a unique and defined maximum.

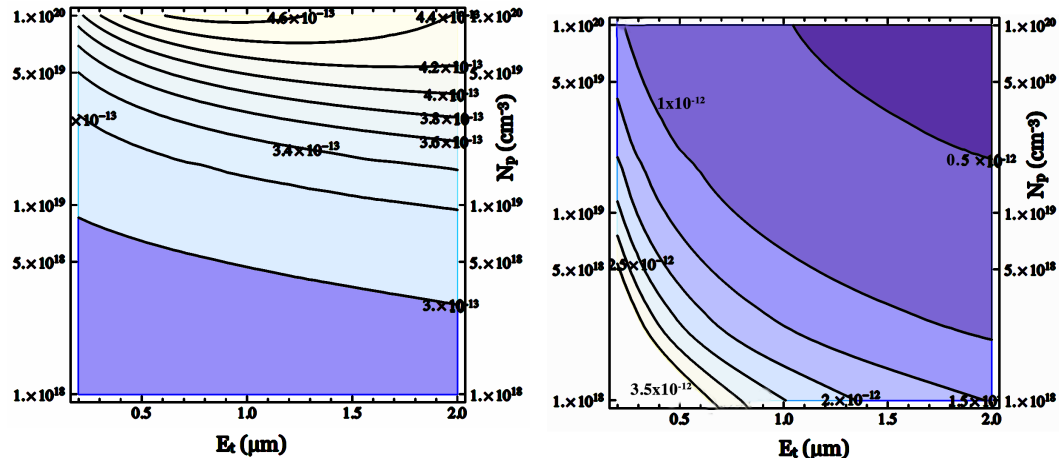
4.2.2 Modeling of the resistance losses

In order to complete the model, the characteristic total series resistance r_s , calculated in the Eq. 4.15, must also be expressed as a function of the design parameters $N_{0,surf}$, E_t and F by means of the Eq. 4.18

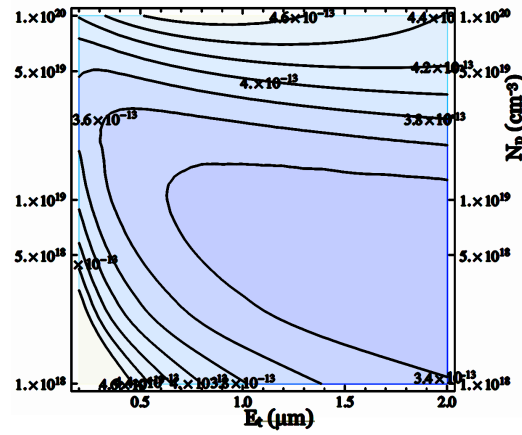
$$r_s(F, N_{0,surf}, E_t) = r_{cb} + \rho w_b + \frac{r_{cf}(N_{0,surf}) + \frac{\rho_m L^2}{12h}}{1 - F} + \frac{r_{sh,e}(N_{0,surf}, E_t) w_f^2}{12(1 - F)^2} \quad (4.25)$$

where the functional dependence of the specific contact resistance r_{cf} with respect $N_{0,surf}$ was described in Eq.4.13. The width of the metal fingers, w_f and its thickness h_f are set by the grid pattern technology. Here we fixed them at $9 \text{ }\mu\text{m}$ and $2 \text{ }\mu\text{m}$ respectively.

The emitter sheet resistance r_{ee} as a function of $N_{0,surf}$ and E_t was calculated in the simulation domain for different values of $N_{0,surf}$ and E_t and shown in Fig 4.7.



(a) Passivated current density recombination J_0^{pas} (b) Metal-contacted current density recombination J_0^{n-pas}



(c) Total recombination calculated with $F = 0.9$

Figure 4.6: Recombination current densities versus surface doping concentration $N_{0,surf}$ and emitter thickness E_t , for passivated (a) and not passivated (b) cell regions. In (c) the total recombination current $[FJ_0^{pas} + (1 - F)J_0^{n-pas}]$ is plotted assuming a transparency factor equal to 0.9.

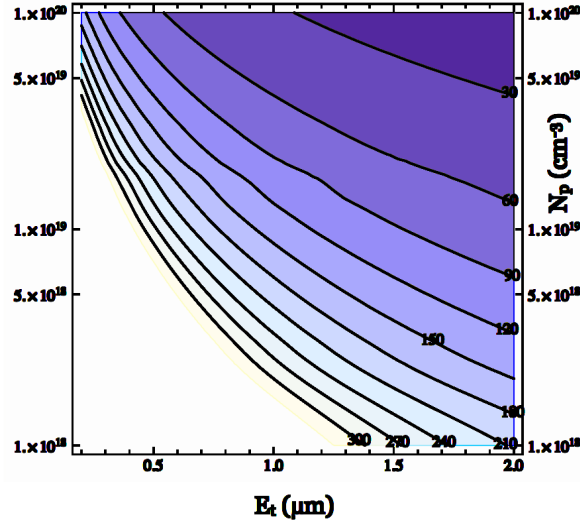


Figure 4.7: Contours of emitter sheet resistance ($r_{sh,e}$) versus surface doping concentration $N_{0,surf}$ and emitter thickness E_t , for emitters with the *erfc* phosphorus profile. The contours are labeled with corresponding values in Ω/sq .

4.2.3 Conversion efficiency maximization

The current-voltage characteristic curve of the solar cells in Eq. 4.21 is now completely defined as a function of C and design parameters F , E_t and $N_{0,surf}$, therefore, the energy conversion factor Γ can be calculated as:

$$\Gamma(V_j, C, F, E_t, N_{0,surf}) = \frac{JV}{P_{inc}C} \quad (4.26)$$

where P_{inc} is the power of the solar radiation per unit area.

Γ is evaluated as a function of the independent variables V_j , C , F , $N_{0,surf}$ and E_t . The conversion efficiency η as a function of c and design parameters is finally calculated by means of the numerical maximization of Γ with respect to V_j :

$$\eta(C, F, E_t, N_{0,surf}) = \Gamma(V_{j,max}, C, F, E_t, N_{0,surf}) = \frac{J(V_{max})V_{max}}{P_{inc}C} \quad (4.27)$$

A further simultaneously maximization of η , by means of an iterative procedure, with respect to the parameters F , E_t and $N_{0,surf}$ allows to calculate the optimum design values of the metal-grid transparency factor, emitter thickness and surface doping density for different light concentration factors.

4.2.4 Design rules for the emitter and the metal grid

The optimum estimation of parameters has been calculated for different concentration factors and summarized in Table 4.2. For the clarity the finger spacing (related to the transparency factor by Eq. 4.18) is also indicated in the table.

Table 4.2: Optimum design parameters of front-side contacted cells for different concentration factors.

Conc. Factor (Suns)	Transparency factor [Finger Spacing (μm)]	Emitter Thickness (μm)	Surface Doping Conc. (cm^{-3})
1 Sun	0.987 [750]	0.9	$7 \cdot 10^{18}$
10 Suns	0.977 [435]	0.9	$1.1 \cdot 10^{19}$
40 Suns	0.958 [240]	0.7	$1.6 \cdot 10^{19}$
100 Suns	0.941 [170]	0.7	$1.6 \cdot 10^{19}$
150 Suns	0.935 [140]	0.7	$1.8 \cdot 10^{19}$

Fig. 4.8 shows the optimum finger spacing and the optimum surface dopant density as a function of the concentration factor. It can be noted that the optimum finger spacing and metal design parameters under concentrated light are strongly different from the parameters calculated at 1 sun condition. In particular, the optimum finger spacing rapidly decreases with the concentration factor increase, then after 40 suns the slope becomes less steep. The emitter surface doping density shows the same behavior: it increases logarithmically at low concentration factors, then it grows linearly. It means that, when increasing the light concentration, a high-doped emitter surface is the best solution for the concomitant minimization of the emitter sheet resistance, the contact resistance and the recombination losses at the surface. We found that the optimal emitter thickness, for this kind of cells, is almost independent of the concentration factor as it can be seen in Tab. 4.2.

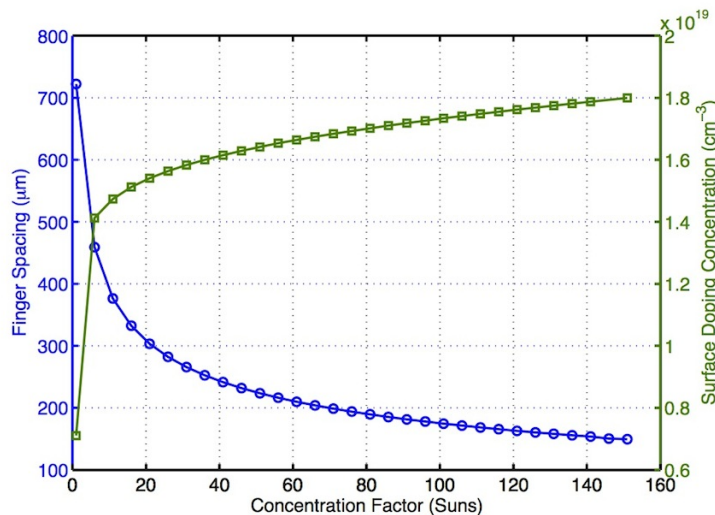
**Figure 4.8:** Optimized values of finger spacing and surface dopant concentration as a function of the concentration factor. The width and the height of the finger are fixed to $9\mu\text{m}$ and $2\mu\text{m}$ respectively.

Fig. 4.9 shows the contour plots of the simulated cell efficiency as a function of the emitter thickness and surface doping density, for four different concentration factors (1, 10, 40 and 100 Suns). Each graph is calculated considering the optimum finger spacing its that specific concentration. It can be noted that the efficiency plateau region is smaller for the cell under concentrated light in comparison with the cell under 1 sun illumination. It means that concentrator solar cells are more sensitive to the emitter doping design than the 1-sun cells, therefore the design of the emitter is a crucial point to maximize the cell efficiency.

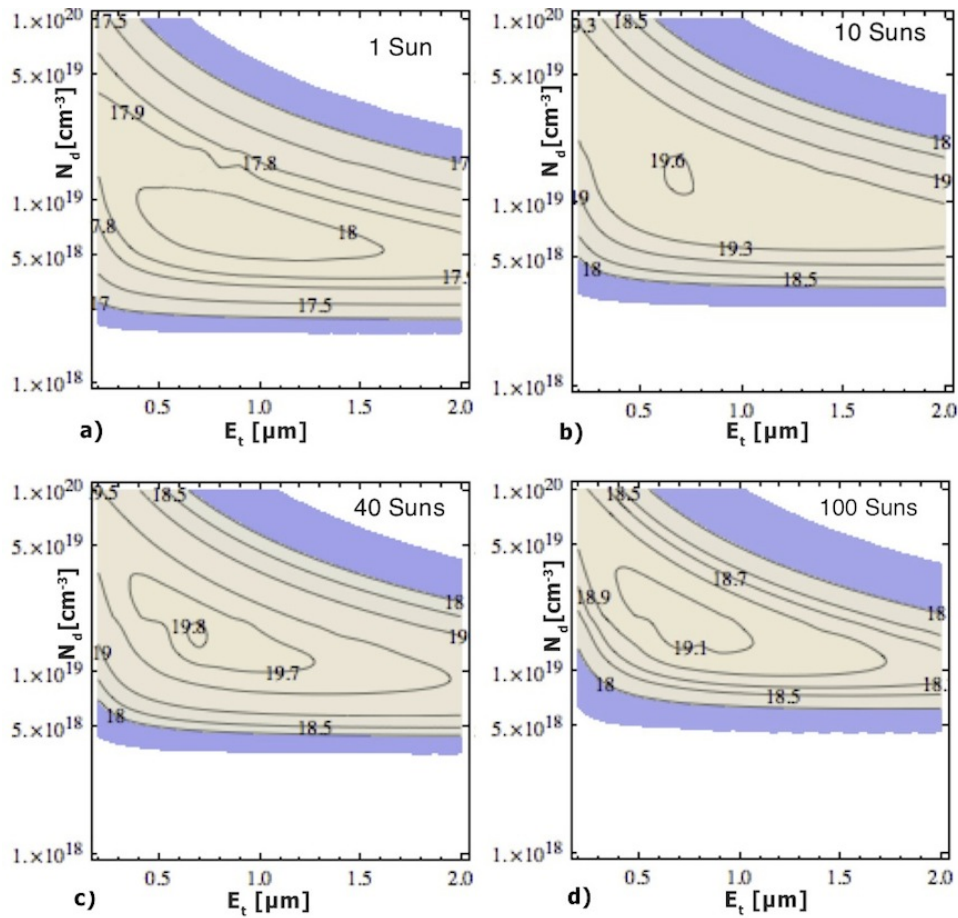


Figure 4.9: Contour Plots of the conversion efficiency for the simulated solar cell as a function of the surface doping concentration N_d and of the emitter thickness E_t , for four different concentration factors.

4.2.5 Quantitative analysis of the resistance losses

In order to quantitatively analyze the resistance losses of the optimized solar cell under concentrated light, the different losses mechanism have been quantified by means of the Eq. 4.25. Table 4.3 shows the different contributions to the total series

resistance calculated for solar cells under 1, 10 and 100 suns. For each concentration factor, the optimum calculated design parameters relative to that concentration level have been used. The total resistance decreases with the concentration factor as expected, and at high concentration factors it is dominated by the base resistance in the semiconductor.

Table 4.3: Contribution to the total series resistance for cells optimized to work under different concentration factor. All the values are in Ωcm^2 .

Component	1 sun	10 suns	100 suns
base (r_b)	0.014 (10%)	0.014 (29%)	0.014 (64%)
front contact (r_{fc})	0.028 (21%)	$5 \cdot 10^{-3}$ (10%)	$8 \cdot 10^{-4}$ (4%)
emitter (r_e)	0.07 (54%)	0.018 (37%)	$2.5 \cdot 10^{-3}$ (11%)
metal (r_m)	0.02 (15%)	0.012 (10%)	$4.5 \cdot 10^{-3}$ (21%)
total	0.137	0.048	0.022

Obviously high-injection conditions are not taken into account in this model. Under high-injection conditions the mobility is expected to increase since the photogenerated carries also contribute to the total conductivity. Therefore, the bulk resistance is expected to decrease for high concentration factors. In order to analyze these high-injections effects, in the next section we use two-dimensional numerical simulations to further investigate the cell characteristics under concentrated sunlight and to refine the design optimization.

4.3 Electrical and Optical Simulations

The co-optimization model presented previously allows a flexible and time-saving calculation of the design parameters of concentrator solar cells. However, many assumptions were made in the model. For example, the recombination currents are considered independent of the carrier density and the high-injection effects on the recombination and on the carrier mobility were not taken into account. These assumptions are not restrictive for optimizing the emitter and the metal grid, since the emitter is always in low-injection also for high concentrations. On the other hand, high-level injection effects become important into the low-doped substrate. Therefore to investigate the role of some substrate characteristic parameters (like resistivity, thickness and lifetime) a more general model should be used.

Here, coupled two-dimensional electrical and optical simulations are used to model the cell and to exactly predict its performance under concentrated light.

The substrate thickness and doping level were varied to find the optimum value maximizing the efficiency under concentrated light. Afterwards the role of the Back Surface Field (BSF) was investigated and finally numerical simulations are used to validate the emitter and the metal grid co-optimization model previously described.

4.3.1 Simulation process

As the first step in the simulation process, the complete solar cell is divided in the so-called “symmetry elements” (see Figure 4.10). A symmetry element reaches from the middle of a n-contact to the middle of the finger spacing. In simulating one symmetry element, a redundant simulation of the same symmetry elements can be avoided. In the next step a discretisation grid (or *mesh*) is applied to the symmetry element, in order to solve the semiconductor equations at the nodes of the grid. The discretisation grid is not uniform across the whole structure. As a general rule, the grid should be denser in the regions where high gradient of the carrier density, doping or electric field are expected: emitter region, back surface doped region and in the contact region close to the finger (Fig. 4.10).

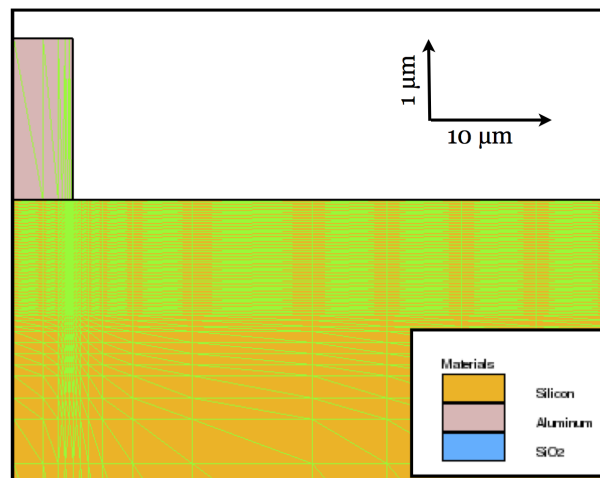


Figure 4.10: Symmetry element used in the numerical simulations with the generated non-uniform mesh-grid (in green).

At the nodes of the discretization grid the poisson equation (Equation 2.38) and the transport equations (Equation 2.34 and Equation 2.36) are solved by using a numerical simulation tool, and the current density in all the device is calculated (see Fig. 4.11). The results shown in the following have been obtained by using two different tools. The first is Sentaurus [52], while the second is Atlas [53]. The calibration of the simulator tool, the design of the device and the definition of

the physical models were carried out in collaboration with ARCES, University of Bologna, Italy [54].

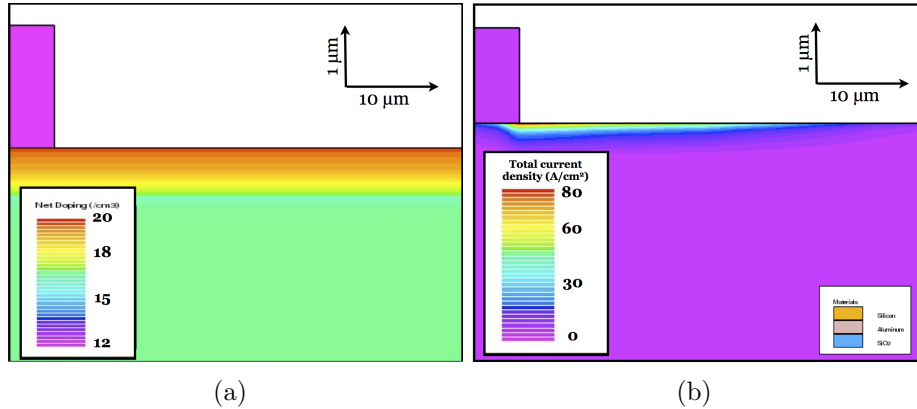


Figure 4.11

As result of the numerical simulations the IV-curves of the symmetry element, calculated for different incident irradiances, are given. The numerical simulations does not take into account the resistance losses in the metal grid. This effect is accounted in the post-processing, where the lumped metal grid resistance (calculated in Section 4.1) is used to obtain the final cell output.

4.3.2 Simulation parameters and models

Numerical simulations were calibrated and optimized to take into account the carrier recombination and mobility in high-injection condition. The following physical models have been used in the simulation tool:

- The Fermi-Dirac statistic was used. In the high-doping regime the common used Maxwell-Boltzmann statistics differs significantly from the more realistic Fermi statistics. Therefore Fermi statistics becomes important for high values of carrier densities, as for example in the high-doped emitter region, where $n > 1 \cdot 10^{19} \text{ cm}^{-3}$ is commonly reached.
- Full model for Auger and surface recombination suitably modified to be self-consistent with Fermi statistics.
- Doping-dependent SRH recombination. In this model the minority lifetimes τ_n and τ_p are modeled as a function of the dopant density by means of the *Scharfetter relation* [55] [56] [57]. This doping-dependent model is necessary to correctly model the SRH recombination in the high-doped emitter and BSF.

- The Schenk bandgap narrowing (BGN) model has been used. Commonly, constant or doping-dependent BGN models are used in simulating solar cells. However, in this way, BGN dependence on the the free-carrier concentration is not taken into account. For concentrator solar cells this effect could be very important, since high carrier concentration are produced by the high-power incident light. The Schenk BGN model, described in [58], also takes into account the carrier concentration induced narrowing effect in silicon.
- The *Philips unified mobility model* was used to describe the carrier mobility [26]. This model describes the mobility degradation due to both impurity scattering and carrier-carrier scattering mechanisms (due to free carriers, and ionized donors and acceptors). The model allows to take into account the mobility of carriers in both the high-doped emitter and in the high-injection base, where the free carriers density is higher than the ionized acceptors density.

With regard to the characteristics parameters in the simulations, we used the experimentally measured doping profiles for phosphorus and boron shown in Fig 3.7 and 3.8 respectively. The experimental value of the SRH bulk lifetime, as calculated in Section 3.3, was used. The surface recombination velocities of the passivated and of the non-passivated surfaces were calculated as a function of the emitter doping as described in Eqs. 4.22 and 4.23. Unless otherwise specified, the cell parameters used in numerical simulations are considered equal to the ones summarized in Table 4.4.

Table 4.4: Cell parameters used in the model and in numerical simulations

Parameter	Value
Physical cell parameters	
Cell area	$4 \times 4 \text{ mm}^2$
Cell thickness	$280 \text{ }\mu\text{m}$
Substrate resistivity	$0.5 \text{ }\Omega\text{cm}$
Metal finger width	$10 \text{ }\mu\text{m}$
Metal finger thickness	$2 \text{ }\mu\text{m}$
Recombination parameters	
Bulk minority carrier lifetime	$60 \text{ }\mu\text{s}$
Front surface (passivated) recombination velocity	10^3 cm/s
Recombination velocity at the metal-silicon interface	$3 \cdot 10^6 \text{ cm/s}$

4.3.3 First simulations results

The cell current output was simulated by sweeping both the bias voltage and the illumination power. Therefore the IV curves were calculated for different concentration factors in the range of 1 - 500 suns. In this way I_{SC} , V_{OC} , FF and η can be calculated as a function of concentration factor C . Figure 4.12 shows the simulated $V_{OC}(C)$ and $\eta(C)$ for a cell with finger spacing $S_f = 100 \mu\text{m}$ and non-textured surface. The results for cells with $0.5 \Omega\text{cm}$ and $10 \Omega\text{cm}$ base resistivity are plotted.

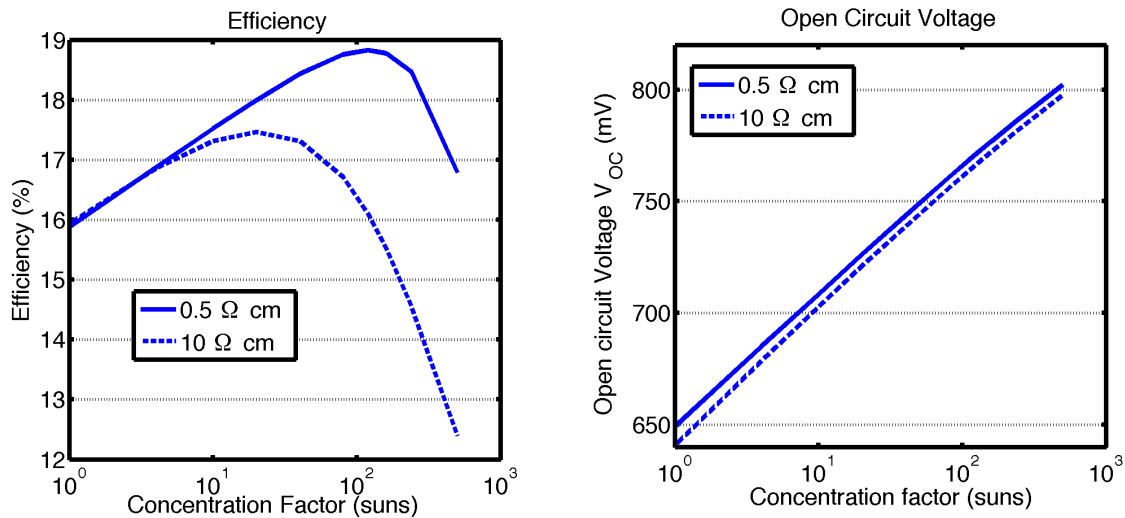


Figure 4.12: Simulated V_{OC} and efficiency of cells with different base doping concentrations.

4.3.4 Determination of the injection level and of the recombination mechanisms

Using two-dimensional numerical simulations, the density of the generated carriers can be determined in dependence on the incident light intensity. The simulated carriers densities in the solar cell allow the estimation of the injection condition in the cell substrate (low- or high-level injection) in dependence on the concentration level. Figure 4.13 shows the profiles of the electron density (red curves) along the cell thickness, for a $0.5 \Omega\text{cm}$ cell (a) and a $10 \Omega\text{cm}$ cell (b). The intrinsic doping levels of the substrates are indicated with solid blue lines. The cells were simulated in the maximum power point condition.

In the case of the low-resistivity cell, the excess carrier density is always lower than the base doping level also under high illumination power, therefore the cell is anyhow in low-injection conditions up to 500 suns. On the other hand, the high-

resistivity cell is in high-injection condition for concentration factors higher than 10 suns.

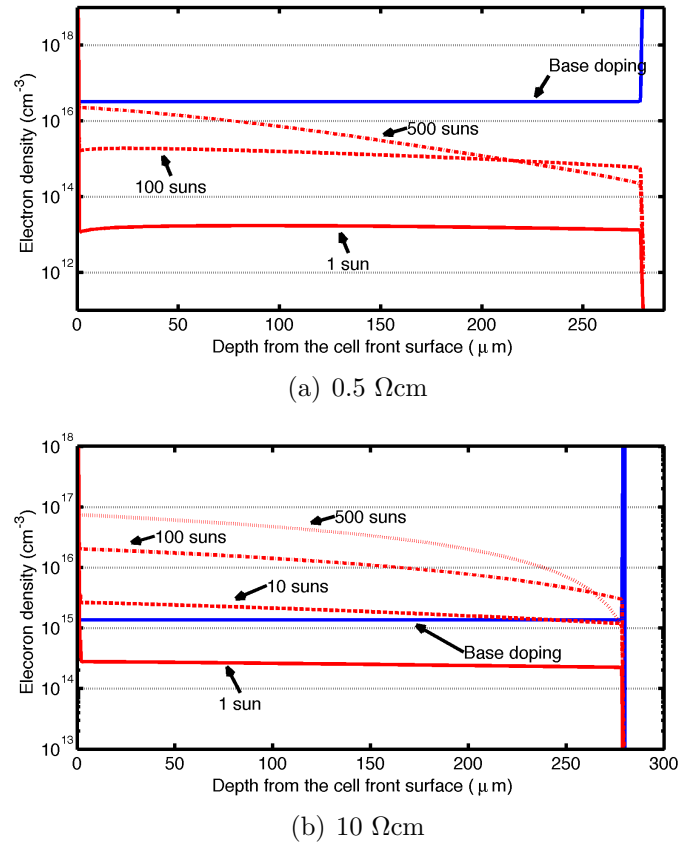


Figure 4.13: Electron density profile along cell thickness at the maximum power point calculated for different concentration factors. The blue line represents the base doping level for the $0.5 \Omega\text{cm}$ (a) and the $10 \Omega\text{cm}$ (b) solar cells. The low-resistivity cell is anyhow in low-injection conditions, while the high-resistivity cell is in high-injection for $C > 10$ suns.

The asymmetrical behavior of the carrier concentration density shown in Fig. 4.13 is due to the asymmetrical generation rate, since the peak generation rate occurs at the cell surface and attenuates rapidly into the bulk.

In order to investigate the recombination mechanisms in high-level injected solar cells, the V_{OC} dependence on the concentration factor was analyzed. Using the one-diode IV characteristic, it results a logarithmic dependence of the V_{OC} with the concentration factor C , as shown in Eq. 2.59 in Chapter 2. Thus, the diode ideality factors n can be determined by plotting the open-circuit voltage V_{OC} as a function of the logarithm of the concentration. From the ideality factor estimation, the dominating recombination mechanisms in the cell under concentrated light can

be investigated.

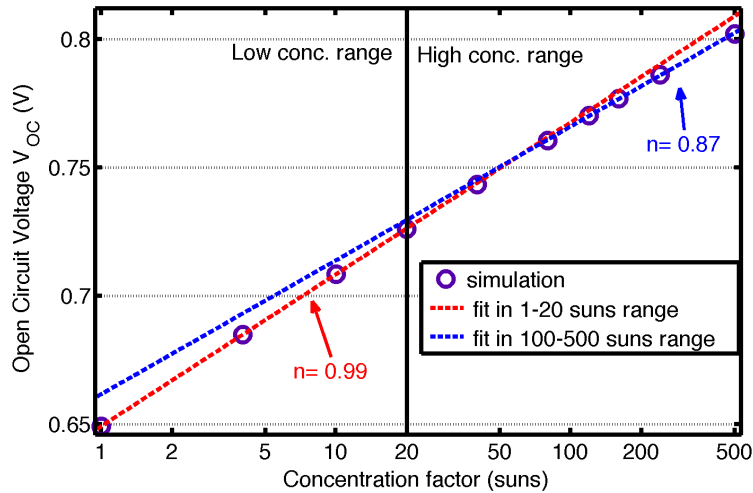


Figure 4.14: Simulated open circuit voltages versus concentration for the 0.5 Ωcm solar cell. The ideality factors in low- and high-concentration ranges are determined by using logarithmic fits of the simulated V_{OC} curves. The red curve fits the cell in low-concentration range while the blue line represents the fit in the high-concentration range.

Figure 4.14 shows the simulated open circuit voltage versus the concentration factor for the 0.5 Ωcm cell. The ideality factor was determined in the low-concentration (1 – 20 suns) and high-concentration (100 – 500 suns) ranges by using a logarithmic fit of the simulated V_{OC} curves. The estimated ideality factor in the low-concentration range is 0.99 while in the high-concentration range it is equal to 0.87. The ideality factor is around 1 for concentration levels under 20 suns as predicted by the ideal current voltage characteristics of a cell in low-injection conditions (see Equation 2.59). Over 100 suns the ideality factor decreases under 1. An ideality factor smaller than 1 is a sign for Auger recombination, which is the only recombination mechanism with an ideality factor smaller than one as shown in Table 2.1.

4.4 Simulation trends

In this section numerical simulations are exploited to investigate the effect of the substrate thickness, doping level and BSF-doping on the final cell efficiency. Moreover, in the following the finger spacing optimization is performed by means of electrical numerical simulations with the aim to validate the results obtained by the analytical method presented in Section 4.2.

4.4.1 Finger spacing optimization

Numerical simulations were exploited to optimize the front metal grid of the solar cell that at large concentration levels may seriously limit the conversion efficiency through parasitic series resistance. The optimum finger spacing, as a trade-off between metal-shadowing, metal-contact interface recombination and series resistance, depends on the concentration factor under which the cell operates as discussed in the previous section. The optimization was performed at 20 suns and 160 suns by using the optimum emitter profiles as calculated in Section 4.2.4, and by considering a base resistivity of $0.5 \Omega\text{cm}$.

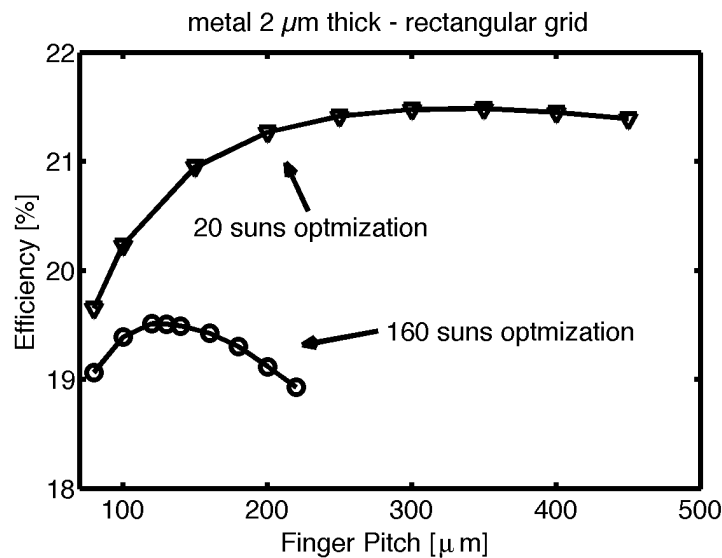


Figure 4.15: Results of the finger pitch optimization for a rectangular metal grid $2\mu\text{m}$ thick. At 20 suns the optimum finger spacing is $350 \mu\text{m}$, and at 160 suns the best value is $130 \mu\text{m}$ (Simulation performed in collaboration with ARCES, University of Bologna, Italy).

The results are presented in Fig. 4.15, where the predicted conversion efficiency is plotted as a function of the finger spacing. At 20 suns the optimum finger spacing is about $350 \mu\text{m}$, while at 160 suns the best value is $130 \mu\text{m}$ in good agreement with the values obtained with the quasi-analytical co-optimization method previously described. It should be noted that at large concentration factors the correct sizing of the metal fingers becomes more critical in order to preserve the cell conversion efficiency

In order to further minimize the resistance of the metal grid, also the influence of the metal thickness and the grid geometry on the conversion efficiency was investigated. In particular, metal $2 - 10 \mu\text{m}$ thick and square and rectangular metal grids (as shown in Fig. 3.4) have been analyzed. Fig. 4.16 shows the finger spacing

optimization at 160 suns of cells with different metal thickness and different grid geometry. These results show that conversion efficiency may be further increased when thicker metallization and square metal grid are used. The square metal grid has the effect of reducing the resistance losses in the metal grid. This is due to the fact that, with this geometry, the “effective” finger length experienced by current to reach the busbar is shorter than in the case of rectangular grid. It can be demonstrated that the resistance of a square metal grid is the half with respect to the rectangular grid [59]. The optimum finger spacings calculated at 20 and 160 suns for the two investigated grid geometry and metal thicknesses are listed in Table 4.5.

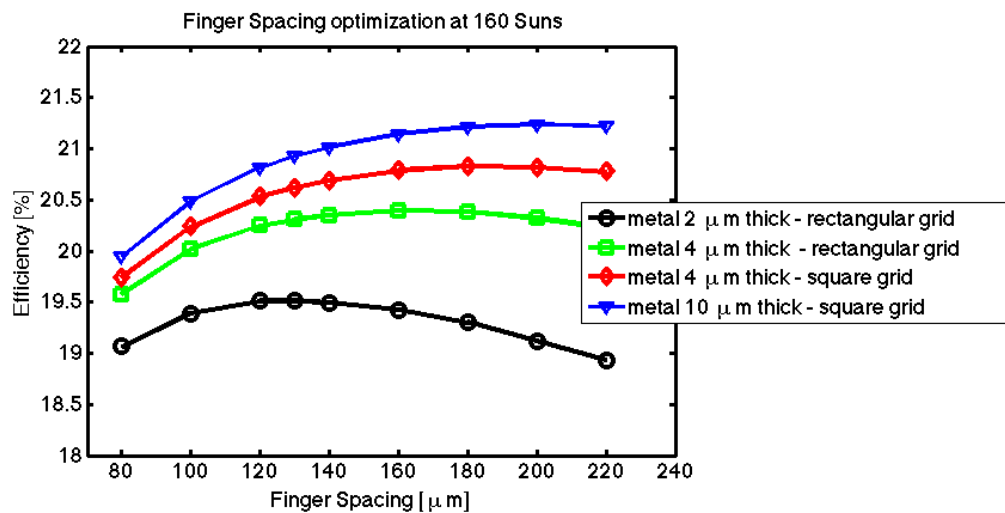


Figure 4.16: Simulated conversion efficiency under 160 suns as a function of the finger spacing. the simulations have been performed by varying the front grid designs and the metal thicknesses. The cell efficiency increases with the metal thickness, and best results are reached when the square grid is used (Simulation performed in collaboration with ARCES, University of Bologna, Italy)

4.4.2 Back surface field

Surface recombination could have a high impact both on the short circuit current and on the open circuit voltage. In order to reduce the surface recombination on the top surface, a passivating oxide layer was used. Since the oxide layer is an insulator, any region which has an ohmic metal contact cannot be passivated using silicon dioxide. This is the case of the rear cell surface, which in our case is constituted by an uniform contact between silicon and aluminum.

Under the contacts the effect of the surface recombination can be minimized by increasing the doping. A Back Surface Field (BSF) consists of a higher doped region

Table 4.5: Optimum finger spacings calculated at 20 and 160 suns for the two grid geometry and different metal thicknesses

metal thickness	160 suns	
	Rectangular grid	Square grid
2 μm	130 μm	160 μm
4 μm	160 μm	180 μm

metal thickness	20 suns	
	Rectangular grid	Square grid
2 μm	350 μm	360 μm
4 μm	360 μm	400 μm

at the rear surface of the solar cell. The interface between the high- and low-doped region behaves like a p - n junction and an electric field forms at the interface. The electric field introduces a barrier to minority carrier flow to the rear surface. The minority carrier concentration is thus maintained at higher levels in the undoped region and the BSF has a net effect of passivating the rear surface.

In order to investigate the role of the BSF on the front-contacted solar cells a set of cells with different BSF doping levels have been simulated. Cell with both 0.5 Ωcm and 10 Ωcm base resistivity have been considered.

Figure 4.17 reports the simulated efficiency (a) and V_{OC} (b) as a function of the concentration factor, for cells with and without BSF. The sheet resistance of the BSF region is here taken equal to 55 Ω/sq .

The BSF has the role to increase the V_{OC} and, as consequence, the conversion efficiency of both the cells. When the BSF is not present, the high-resistivity cell suffers from a reduction of V_{OC} much drastic than the low-resistivity one. On the other hand, the BSF has only a slight impact on the performance of the low-resistivity solar cell.

Fig. 4.18 shows the V_{OC} at 1 sun of both the low- and the high-resistivity cell as a function of the BSF sheet resistance. This figure confirms that the BSF doping concentration has a small impact on the performance of the low-resistivity cell, while the V_{OC} of the high-resistivity cell increases with the sheet resistance increasing. With a very high-doped BSF (32 Ω/sq), the V_{OC} of the 10 Ωcm cell reaches the value of the low-resistivity cell.

The difference between the behaviors of the two cell may be explained in terms of carrier diffusion length. The diffusion length in the base depends on the intrinsic dopant concentration. Therefore the diffusion length in 10 Ωcm silicon is expected

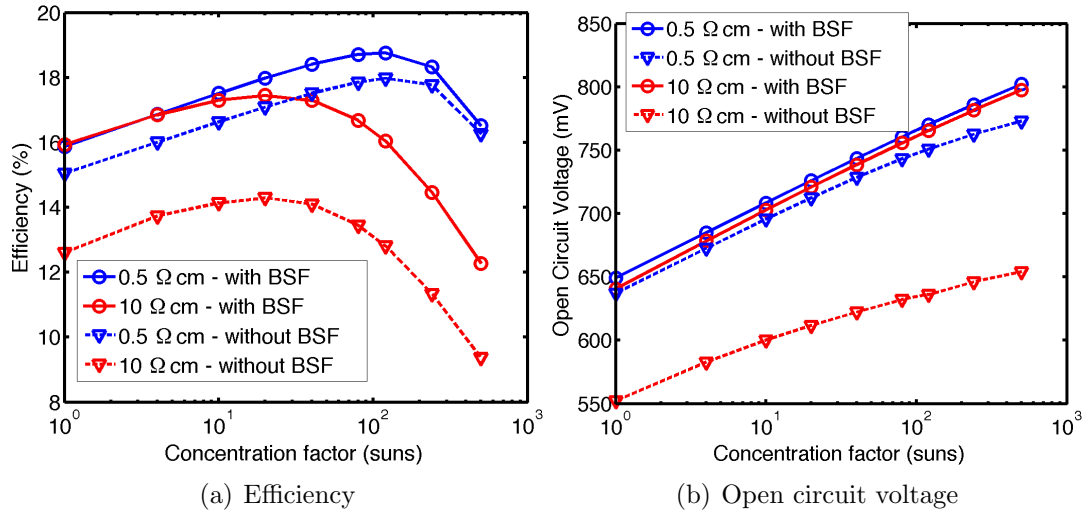


Figure 4.17: Efficiency (a) and V_{OC} (b) as a function of the concentration factor. Red symbols represents the 0.5 Ω cm cell while blue symbols represents the 10 Ω cm cell solar cell. Cell with (circles) and without (triangles) BSF have been simulated. The BSF increases the V_{OC} and the conversion efficiency of both the cells. However, the effect is higher on the high-resistivity cells.

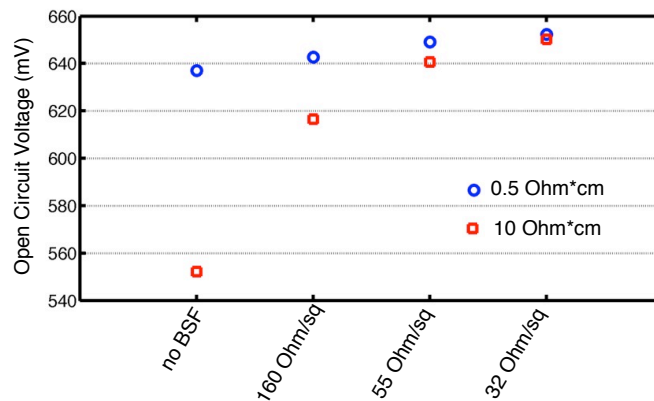


Figure 4.18: Open circuit voltage at 1 sun as a function of the sheet resistance of the BSF. Both the 0.5 Ω cm (blue circles) and the 10 Ω cm (red circles) cells have been simulated. In the case of the high-resistivity cell, a low-doped BSF causes a substantial drop in V_{OC} .

to be higher than the diffusion length in 0.5 Ωcm wafer. When the diffusion length is equal or longer than the cell thickness, the minority carrier density at the rear surface increases, and the recombination at the rear surface becomes a more important recombination mechanism. In this case the BSF has the effective role to reduce the recombination rate and to increase the cell V_{OC} .

4.4.3 Substrate thickness and doping

In Figure 4.12 the efficiency-concentration curve of the 0.5 Ωcm and of the 10 Ωcm solar cells are shown. The efficiency of the high-resistivity cell shows a drop under concentrated light ($C > 10$ suns). At 100 suns this drop is equal to 3% absolute points. At first look this drop could be explained with the resistance losses due to the higher base resistivity. However, the base resistivity may not totally explain the drop in efficiency. In fact, as demonstrated in Fig. 4.13b, when the concentration factor is higher than 10 suns, the 10 Ωcm cell can be considered in high-level injection. Under high-level injection the base resistivity is determined by the generated carriers densities, and it decreases with the light intensity increasing, as discussed in Section 6.4. Therefore, the resistance losses in the base may not be the cause of the efficiency drop experienced by the high-resistivity cell.

A more fundamental cause of the efficiency loss in high-resistivity solar cells was attributed to losses in the short circuit current under concentrated light. Figure 4.19a shows the J_{SC} of the high- and low-resistivity cells as a function of the incident power. In silicon solar cells, the J_{SC} is generally assumed to be linear with the incident power. In order to investigate the linearity of the J_{SC} , the *linearity coefficient* is plotted in Fig. 4.19. The linearity coefficient represents the deviation of the short circuit current from the linear growth, calculated as

$$\text{Linearity}(C) = \frac{J_{SC}(C)}{C} \frac{1}{J_{SC,1\text{-sun}}}$$

In both the cells, J_{SC} at low concentration is linear with the incident power, but for high concentration factors it shows non-linear behavior. The non-linearity behavior depends on the substrate resistivity: low-resistivity cells feature a super-linear excess reaching 5% at 200 suns, while high-resistivity cells feature a sub-linear current loss of about 15% at 200 suns.

In the following J_{SC} sub- and super-linearity effects are more deeply investigated, and it is shown that they are related to two different physical effects: the super-linearity is due to increased collection efficiency into the substrate, while the sub-linearity is due to the recombination current in the emitter region.

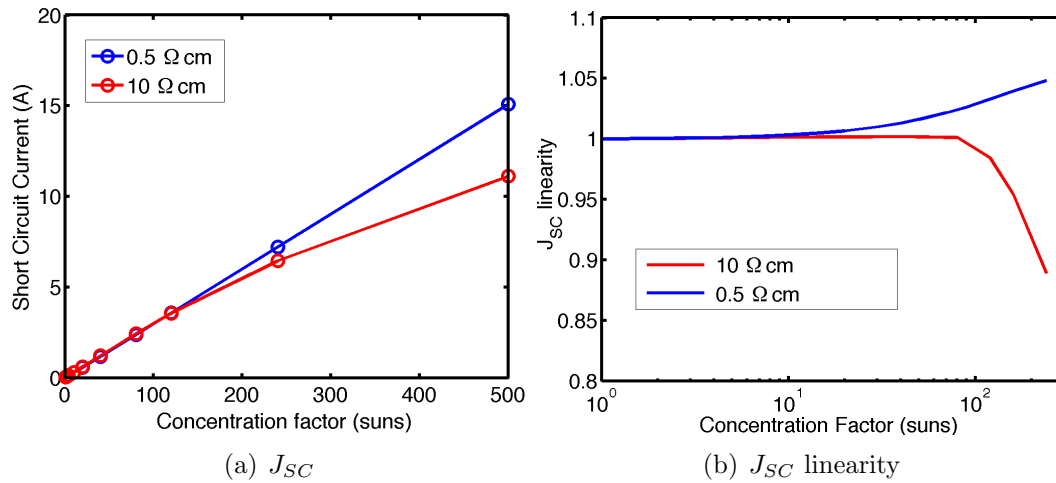


Figure 4.19: Simulated J_{SC} (a) and J_{SC} non-linear excess. The low-resistivity cell (blue circles) features a super-linear excess reaching 5% at 200 suns, while the high-resistivity cell (red circles) shows a more pronounced short circuit loss of 15% at 200 suns.

Short circuit current super-linearity in low-resistivity cells

Figure 4.19b shows that the low-resistivity solar cell responds superlinearly with the concentrate factor. Previous studies on concentrator solar cells have shown the importance of the base electric field in enhancing the collection efficiency of minority carriers generated in the base region[60].

In Figure 4.20 the simulated electric field in the solar cell under short circuit condition is simulated for three different concentration factors. The plot shows the electric field intensity in the first 5 μm from the cell front surface. The field in the emitter region is dominated by the n doping-level and it is almost independent of the illumination power, whereas in the base region it increases linearly with the illumination power. At high irradiation levels, concentrator solar cell produce a proportionately large current. Due to large current flow through the thick base material, an ohmic voltage drop is produced. The direction of the electric field, due to this ohmic voltage drop, aids in the collection of minority carriers for n^+p cell structure, by increasing the charge diffusion length in the bulk. In other words, the electric field redistributes the minority-carrier profile, shifting it toward the collecting junction. This enhancement is expected to involve only the carriers photogenerated in the base region (red and infra-red photons), since minority carriers generated by long-wavelength radiation, deep in the substrate far from the junction, are more efficiently collected by increased electric field.

The effect is clearly shown in Fig.4.21, reporting the cell IQE simulated for

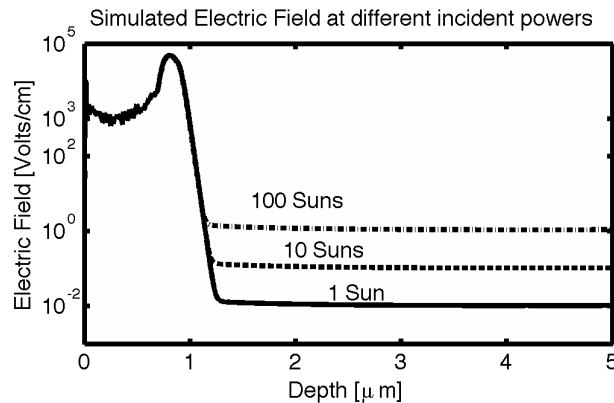


Figure 4.20: Simulated Electric Field at the short circuit condition for three different radiation powers. The plot shows the electric field intensity into the first 5 μm from the cell front surface. The junction depth is at about 0.8 μm from the surface (Simulation performed in collaboration with ARCES, University of Bologna, Italy).

different illumination power levels. For incident irradiance up to 0.1 W/cm^2 the IQE does not depend on power, whereas for higher irradiance level the IQE shows an enhancement in the long wavelength region. The IQE behavior confirms that the J_{SC} super-linear excess under concentrated light involves only those photons with wavelength larger than 600 nm, which are absorbed into the bulk far from the junction. On the other hand photons with wavelength shorter than 600 nm generate a short circuit current linear respect to the incident power. This explanation agrees with previous experiments reported in literature [60] [61] [62].

With the aim to analyze the effect of the electric field in increasing the carriers collection efficiency, the *effective diffusion length* L_{eff} , which includes the effect of the electric field, can be defined [63]:

$$\frac{1}{L_{eff}} = \frac{1}{2L_0} \left[\left(\frac{E}{E_c} \right)^2 + 4 \right]^{1/2} \pm \frac{1}{2L_0} \frac{E}{E_c} \quad (4.28)$$

where $E_c = kT/qL_0$ and L_0 is the low-field diffusion length. The Equation 4.28 indicates that the electric field splits the effective diffusion length into effective upstream (against the field) and effective downstream (with the field) diffusion lengths. The zero electric field diffusion length L_0 simulated in the 0.5 Ωcm substrate cells is equal to 340 μm . Figure 4.22 shows the effective downstream and upstream diffusion lengths as a function of the constant electric field E . Relatively low electric fields of only a few volts per centimeter increase the downstream diffusion length significantly. In fact, in our case, the effective downstream diffusion length increases from 340 μm at 1 sun to near 1000 at 200 suns. Collection increase of minority

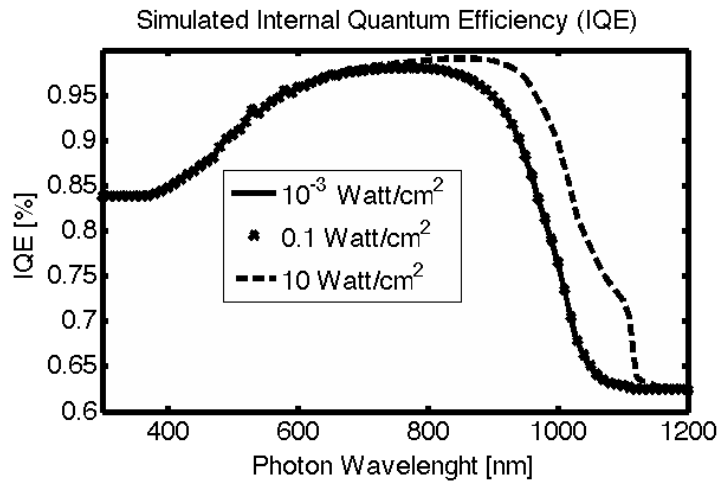


Figure 4.21: Simulated IQE for three different incident radiation powers. For incident powers up to 0.1 W/cm^2 the IQE does not depend on power, whereas for higher power density the IQE shows an enhancement in the long wavelength region (Simulation performed in collaboration with ARCES, University of Bologna, Italy).

carriers in the base due to the enhanced diffusion lengths is sufficient to explain the observed super-linearity.

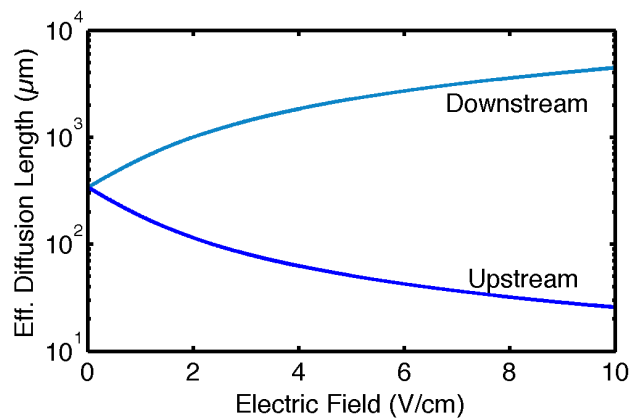


Figure 4.22: Effective upstream and downstream diffusion lengths in the presence of a constant electric field.

Short circuit current sub-linearity in high-resistivity cells

Differently from low-resistivity solar cells, which show super-linear response of the J_{SC} with the incident power, the high-resistivity cells, based on the $10 \text{ } \Omega\text{cm}$ silicon substrate, are affected by a pronounced J_{SC} sub-linearity. This effect was previously observed and reported in literature [60] [64], and the origin of the sub-linear behavior

of the high-resistivity cells was investigated by Green in Reference [65]. In this work the sub-linearity effect was explained in terms of increased recombination current in the emitter region J_{lost} under high illumination power.

Figure 4.13b shows that when the 10 Ωcm cell is in low-injection conditions the electron density profile in the bulk is almost constant in the whole cell thickness, but at the time that it approaches the high-injection condition, the electron density at the front becomes higher than the density at the rear side. Moreover, since the cell is in high-injection condition, $n \approx p$ can be considered in the bulk region.

Generally, in silicon solar cells based on thick substrates, the electron current density in the bulk region is usually negligible under short circuit, due to the low generation rate in the bulk. The hole current density must therefore equals the cell short circuit current density J_{SC} across most of the bulk region. Therefore, the hole diffusion current must be proportional to the J_{SC} :

$$[-qD_p(dp/dx)] \approx J_{SC}. \quad (4.29)$$

If a linear distribution of carriers is assumed in the bulk region (see Fig. 4.13b) the hole and electron density at the junction level (p_j and n_j) may be calculated as in the following:

$$n_j = p_j \approx \frac{J_{SC}W_c}{qD_p} \quad (4.30)$$

where W_c is the bulk thickness and D_p is the hole diffusion coefficient.

With reference to Eq. 2.56, the J_{SC} current density may be expressed as:

$$J_{SC} = CJ_{ph} - J_{lost} = J_{ph} - J_{0e} \left(\frac{n_j p_j}{n_i^2} \right) \quad (4.31)$$

where J_{0e} is the saturation current density associated to the emitter and the last relation follows by the definition of quasi-Fermi levels.

By substituting Eq. 4.30 into Eq. 4.31, the J_{SC} can be finally calculated:

$$J_{SC} = CJ_{ph} - J_{0e} \left(\frac{J_{SC}W_c}{qD_p n_i} \right)^2. \quad (4.32)$$

J_{ph} is the maximum possible current density which can be collected from the cell. The relation fairly describes the sub-linear behavior of the J_{SC} with the concentration factor C . The total J_{SC} in fact is reduced by a factor proportional to the square of its value.

This result suggests two ways of reducing the sub-linearity: one is by reducing the J_{0e} , a second would be decreasing the cell thickness.

Substrate thickness

Figure 4.23 shows the simulated J_{SC} linearity factor of the high-resistivity solar cell by considering different cell thicknesses. The linearity factor under high-concentration level approaches 1 by reducing the cell thickness, as indicated by Eq. 4.32. It can be noted that when the cell is $100\ \mu\text{m}$ thick, the J_{SC} becomes almost linear with the concentration factor.

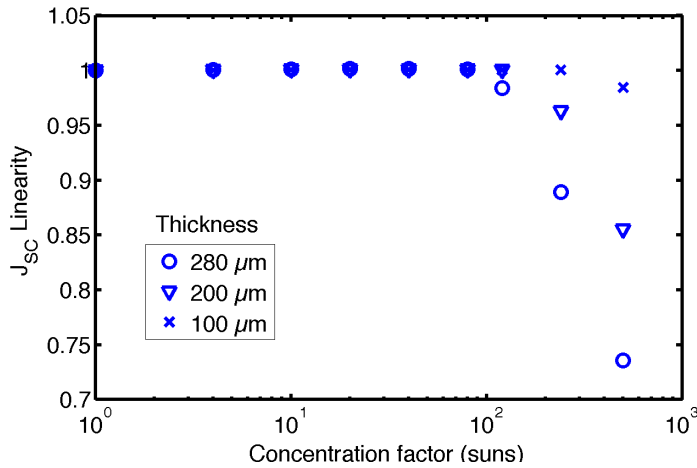


Figure 4.23: Linearity of the J_{SC} simulated on the $10\ \Omega\text{cm}$ silicon substrate for different cell thicknesses. Thick cells show a pronounced sub-linear response, while the J_{SC} of the $100\ \mu\text{m}$ thick cell is almost linear with the incident power.

Figure 4.24 shows the efficiency-concentration curves of both the high-resistivity and low-resistivity solar cells with different thicknesses. At 1 sun the thickest substrate maximizes the cell efficiency, due to the higher light absorption. On the other hand, under high-concentrated light the thinner substrates minimize the resistive losses and, in the case of the high-resistivity cell, avoid the limit due to J_{SC} sub-linearity effect.

In conclusion, these results shown that when solar cells work under high-concentrated sunlight, thin substrates are preferable with respect to thicker ones. A thin substrate is very important especially for high-resistivity cell, where the J_{sc} sub-linearity degrades the performance when thick substrate are used. On the other hand, it should be considered that reducing the cell thickness leads to degrade the optical characteristic of the cell, since silicon is only weakly absorbing the light.

4.4.4 DEPC solar cells

With the aim to overcome the J_{SC} sub-linear effect in the high-resistivity solar cell without degrade the optical characteristic, a new cell structure is proposed in this

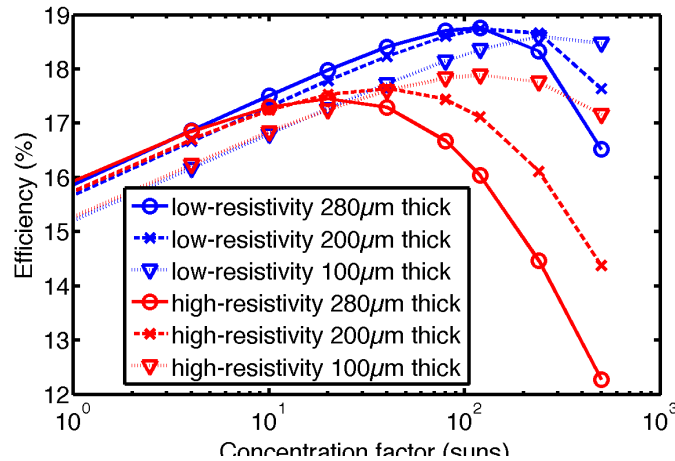


Figure 4.24: Efficiency-concentration curves simulated with different values of the resistivity and of the thickness of the silicon substrate.

work. The concept is based on the using of deep-grooved p -contacts on the rear side of the cell.

The proposed cell scheme is represented in Figure 4.25. Starting from the rear side of the cell a matrix of deep-grooved holes are designed. The grooved-holes go through the silicon substrate and they stop very close to the front surface. Such a cell design is named DEPC solar cell (Deep-Etched P -Contacts), even though the grooved holes are not real “contacts” because no metal is present inside the hole. On the other hand the internal side of the holes is high-doped with boron, as shown in Fig. 4.25. In this way, the degenerate internal hole surface acts as low resistance current paths to drain the p -carriers from the front surface, where have been generated, to the back surface. Therefore, the deeply-etched holes have the role of reducing of the “effective thickness” of the solar cell. In conclusion, with this technique it is possible to decouple the absorbing cell thickness from the effective distance between the BSF and the front junction.

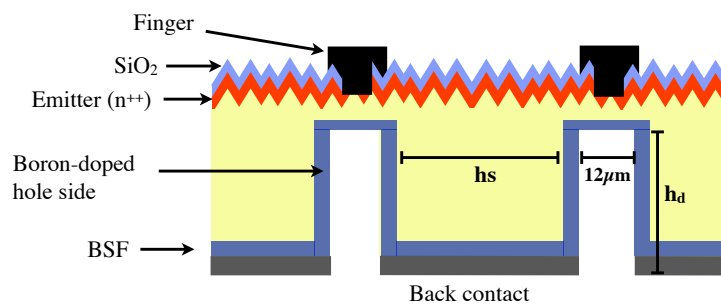


Figure 4.25: Section of the DEPC cell concept. The deep holes are etched into the silicon substrate and the internal side walls are boron-doped.

The holes depth in this structure is similar to the cell thickness ($\sim 260 \mu\text{m}$), while the diameter is considered equal to $12 \mu\text{m}$, since, as explained in Section 3.5.1, this is the lowest value achievable with the fabrication technology available at MTLab-FBK, without reducing the hole depth.

In order to investigate the performance of DEPC solar cells and to optimize the cell design, numerical simulations have been used to simulate the cell efficiency. Obviously the two-dimensional simulations used on this work can be useful only to investigate the expected trends of the conversion efficient with respect to the design parameters. With the aim to obtain a more realistic and accurate prediction of the cell performance a full three-dimensional simulation of the device should be performed.

The design of the front surface (metal thickness, finger spacing and emitter doping profiles) are taken equal to the best values resulted from the previous simulations and a substrate with $10 \Omega\text{cm}$ resistivity was considered. Two parameters have been varied in the simulated cell layout (see Fig. 4.25): the distance between the holes h_s , and the depth of the holes h_d . In particular, two different hole spacings have been tested: $180 \mu\text{m}$ (equal to the finger spacing) and $90 \mu\text{m}$. Cells with $200 \mu\text{m}$ and $260 \mu\text{m}$ deep holes have also been simulated.

In Figure 4.26 the efficiency-concentration curves of DEPC solar cells with design variations are outlined. In the figure, the efficiency of a standard solar based on the same $10 \Omega\text{cm}$ substrate, but without grooved-contacts is reported and named “Reference”.

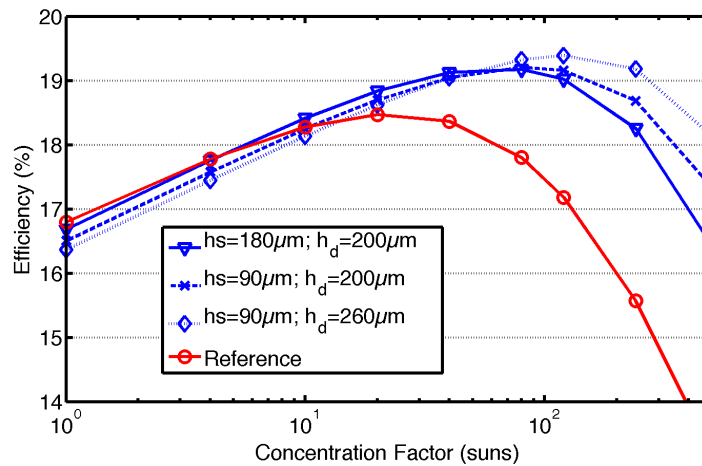


Figure 4.26: Efficiency of the DEPC solar cells as a function of the concentration factor. Cell with different hole spacing (h_s) and hole depth (h_d) have been simulated. The efficiency of a reference cell without grooved-holes is also reported (red line)

Although under 1 sun the reference cell is slightly more efficient than the DEPC cells, under concentrated light the efficiency of the DEPC cells is up to 20% higher than the reference one. The best performance are reached by the sample with the shortest hole spacing and the deepest holes. At 200 suns this sample shows conversion efficiency higher than 19%, while the efficiency of the reference cell is equal to 16%.

The reason of the higher efficiency shown by the DEPC cells with respect to the reference cell is related to the resistance losses in the base and to the J_{SC} losses due to sub-linearity. Figure 4.27 shows the fill factor (a) and the J_{SC} linearity coefficient (b) of the DEPC solar cells and of the reference cell. The DEPC cells show a fill factor higher than the reference cell under concentrated light. High fill factor indicates low series resistance losses. Moreover, it should be noted that the J_{SC} sub-linearity is strongly reduced for the DEPC cells, and for the sample with $hs = 90 \mu\text{m}$ and $h_d = 260 \mu\text{m}$, the J_{SC} respond linearly with the concentration factor up to 500 suns. These results show the effectiveness of the DEPC solar cell concept in the overcoming the J_{SC} sub-linearity effect and in minimizing the series resistance in solar cells based on thick and high-resistivity substrate.

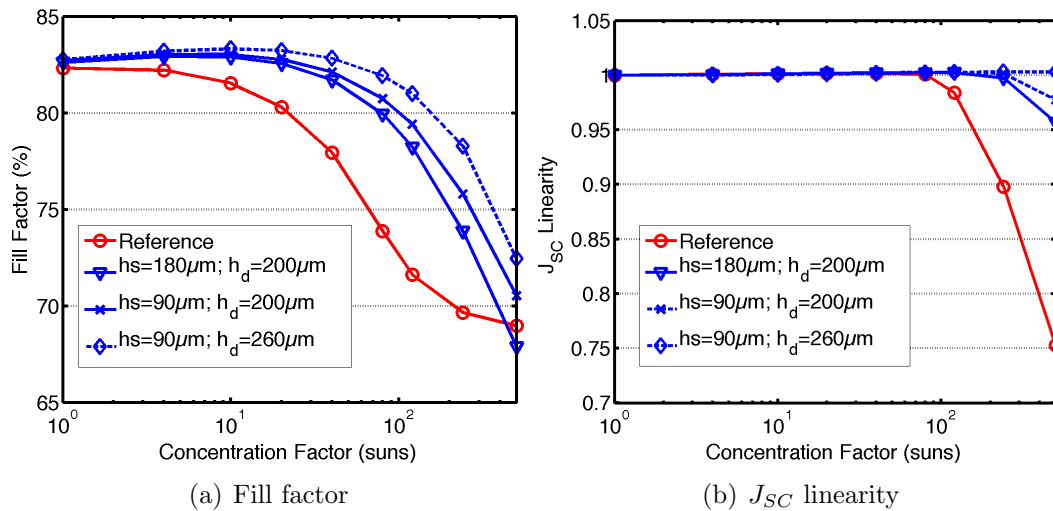


Figure 4.27: Simulated fill factor (a) and J_{SC} linearity coefficient (b) of DEPC solar cells with different design parameters (blue lines) and of the reference cell (red line).

CHAPTER 5

Cell testing methods

In this chapter the measurement methods for an exhaustive characterization of concentrator solar cells are described. First, a preliminary electrical characterization of the principal cell parameters is presented and the cell test packaging is described. The cell efficiency was measured as a function of the concentration factor by using a concentrator photovoltaic solar simulator developed by MTLab. A brief description of the testing system is reported with an analysis of the measurement errors. Moreover, the experimental techniques for measuring the quantum efficiency and the series resistance of the cell are analyzed.

5.1 Preliminary electrical characterization

In order to control the fabrication process and to measure some important electrical characteristics of the cell, a set of test structures has been fabricated onto the process wafer together with the cells. The structures are collected in two test strips as shown in Figure 5.1. Many copies of these test strips are uniformly displaced into the wafer. In such a way we can monitor the electrical characteristics in the whole wafer size and control doping, contacts and metal uniformity. The test strips are contacted with a test probe card and the measurements are collected in an automatic way. The fabricated test structures are described in the following.

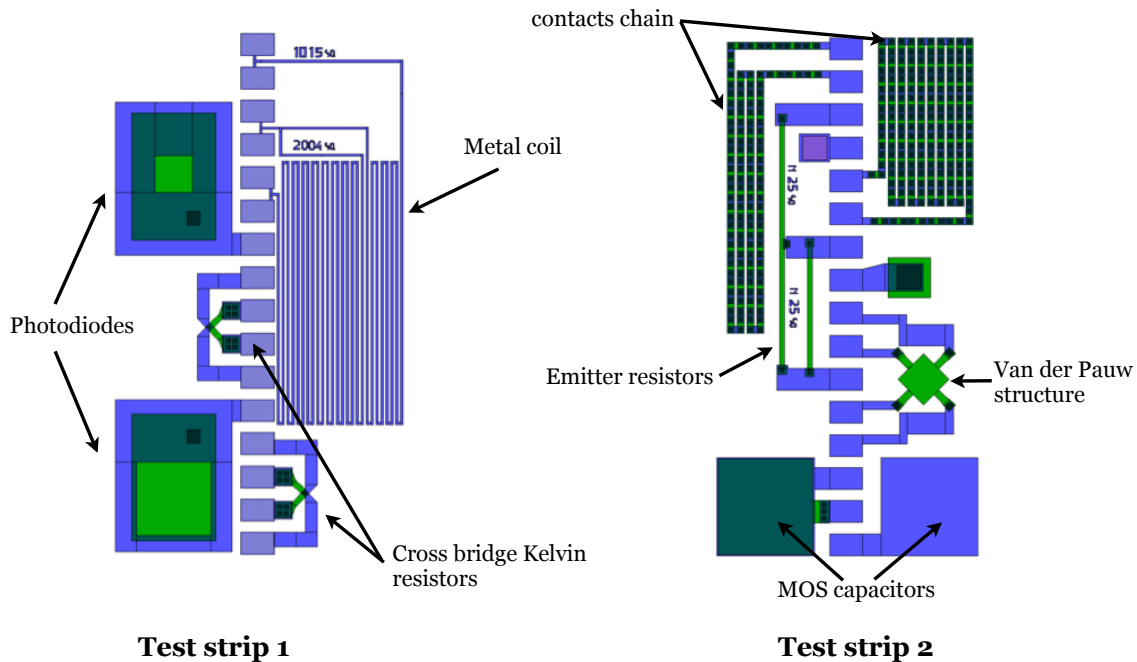


Figure 5.1: Scheme of the tests structures, which are displaced in the process wafer.

- **Metal coils.** Three aluminum coils with different lengths are used in order to determine the metal resistivity. In particular if R is the measured resistance of the coil and L and S are the coil length and section area respectively, the metal resistivity can be calculated as $\rho_m = \frac{RS}{L}$.
- **Photodiodes.** Two diodes n^+p of different areas are used in order to determine the inverse saturation current density J_0 and the breakdown voltage. These parameters are used to control and assess the emitter doping process.
- **Contact chain.** A chain of about 100 small contacts ($6 \times 6 \mu\text{m}^2$) connected two by two with metal, was produced in order to check the uniformity in the contacts opening process.
- **Emitter resistors.** Two linear regions of different lengths are n -doped. These structures are used to measure the sheet resistance of the n -doped region.
- **MOS capacitor.** A capacitance-voltage curve measured on the MOS capacitor is used to estimate the thickness of the SiO_2 on the top surface.
- **Cross bridge Kelvin resistor.** This structure allows to measure the contact resistance between emitter and metal by using a four-point measurement method. While generating a constant current between area 2 and 3 in Figure

5.2 (a), the voltage drop between area 1 and 4 is measured for determining the contact resistance. The contact resistance is then $R_{cont} = \frac{V_{1-4}}{I_{2-3}} A_{cont}$.

- **Van der Pauw structure** This technique is used to measure with high precision the sheet resistance of the emitter region. To perform the measurement, a current is made to flow along one edge of the sample (for instance, I_{12} in Fig. 5.2 b) so that the voltage across the opposite edge (in this case, V_{34}) can be measured. Starting from two distinct measurements, the emitter sheet resistance can be found by using the Van der Pauw formula.

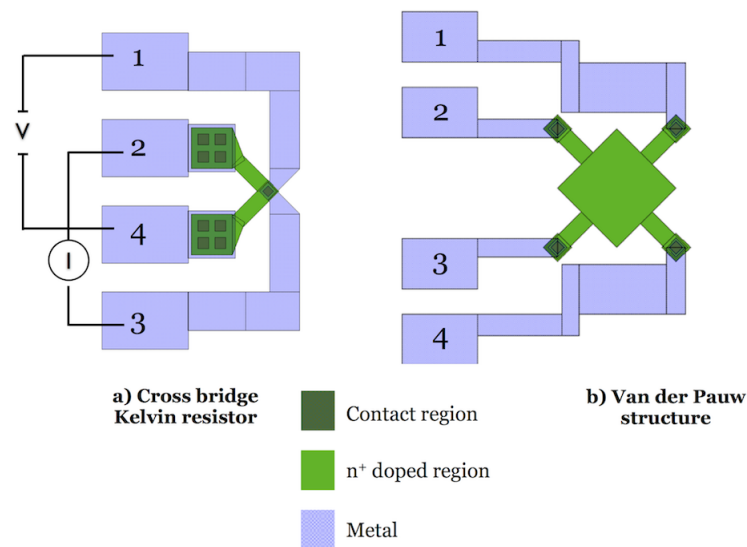


Figure 5.2: Cross bridge Kelvin resistor (a), used to measure the n⁺/metal contact resistance and the Van der Pauw structure, which is used to estimate the emitter sheet resistance.

The mean values measured on the test structures in our standard process are listed in Table 5.1.

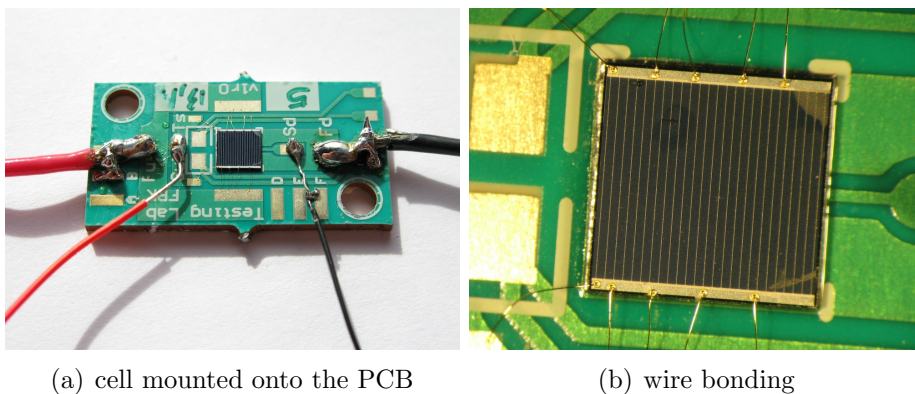
5.2 Packaging for testing

In order to measure the fabricated front *n*-contact solar cells under Standard Test Conditions the cells are diced out of the wafer for mounting them. For measuring the cells up to 350 suns, low electrical losses and a high heat exchange for the mounting system are necessary. The electrical contact resistance between the cell and the mounting system should be significantly smaller than the series resistance of the cell (generally $\ll 0.02\Omega \text{ cm}^2$).

Table 5.1: Test structures fabricated on the process wafer and characterization of some important electrical parameters.

Structure	Measured Quantity	Mean Value
Metal coil	Metal resistivity	$(3.6 \pm 0.3) \cdot 10^{-6} \Omega \text{ cm}$
CMOS capacitor	SiO ₂ thickness	$(112 \pm 2) \text{ nm}$
Emitter resistor	emitter sheet resistance	$(71 \pm 9) \Omega/\text{sq}$
Van der Pauw	emitter sheet resistance	$(72 \pm 8) \Omega/\text{sq}$
Contacts chain	contact opening yield	$> 99.9\%$
Kelvin resistor	front contact resistance	$(4 \pm 1) \cdot 10^{-5} \Omega \text{ cm}^2$
Photodiode	leakage current at -5V	$3 \cdot 10^{-9} \text{ A/cm}^2$
	Breakdown voltage	$23 \pm 1 \text{ Volt}$

The front busbars are contacted by means of wire-bonding by using gold wires with diameter of $10 \mu\text{m}$. The wires are about 2 mm long. Each wire introduces an electrical resistance of about 0.5Ω . Therefore more than 100 wires are necessary to take low the metal resistance. In order to test the cells we developed a dedicated printed circuit board (PCB) specifically designed to perform *4-wires measurements*. In this way a single wire is used to sense the voltage on the busbar, while the others carry out the current, therefore the measurement is not affected by the resistance of metal wires. As a result of the 4-wires measurement the number of wires can be reduced without affecting the measurement, and so we bonded our cells with only 10 wires equally spaced, 2 of them are used for sensing. Pictures of the cell mounted onto the testing PCB are shown in Figure 5.3.

**Figure 5.3:** The cell mounted onto the PCB (a) and a particular of wire bonding which connect the front busbars to the PCB contacts (b).

The back contact does not present particular connecting problem because it is as large as the whole device. The back of the cell is connected to the PCB by means

of a epoxy silver loaded adhesive. This component shows excellent properties in terms of electrical and thermal conductivity. The electrical conductivity is lower than $5 \cdot 10^{-3} \Omega\text{cm}$. A layer of epoxy adhesive was applied to solder the cell onto the PCB by means of a thermal treatment. The electrical resistance of the back contact is lower than $5 \cdot 10^{-4} \Omega$. Also the back was contacted with 2 electrodes to perform the measurement in 4-wires mode.

Thermal effects

In order to perform the cell characterization in Standard Test Conditions, the cell should be kept at constant temperature of 25°C . Due to the huge incident power under concentrated light, the cell tends to increase quickly its temperature, therefore the temperature of the measuring chuck is controlled by a cooling system. However, the heat exchange between the cell and the testing chuck system should be optimized in order to minimize the temperature gradient. For an estimation of the latter, the heat transport equation is used:

$$G = -\kappa \frac{\partial T}{\partial x} \quad (5.1)$$

where G is the incident irradiance, κ is the thermally conductive coefficient, T is the absolute temperature and x is the thickness of the material. In our mounting system, there are two layers between the cell and the testing chuck: the epoxy adhesive, which connects the cell to the PCB and PCB itself. The PCB was fabricated on aluminum substrate to maximize the thermal coefficient. Afterwards the PCB is connected to the testing chuck by means of thermally conductive adhesive. Table 5.2 reports the thermal coefficients together with the estimation of the temperature gap ΔT introduced by each layer as a function of the concentrator factor and calculated by Eq. 5.1. In this estimation, the epoxy adhesive layer was considered $100 \mu\text{m}$ thick and electrical efficiency of the cell was considered equal to 20%.

Table 5.2: Thermal coefficient, thickness and ΔT of the layers between the cell and the testing chuck

Layer	Thermal coeff. (κ)	Thickness	$\Delta T \cdot C$
Epoxy adhesive	$1.6 \cdot 10^{-2} [\text{W}/\text{cm}/^\circ\text{K}]$	0.01 cm	$0.037 \cdot C [^\circ\text{K} \cdot \text{suns}]$
Al PCB	2 $[\text{W}/\text{cm}/^\circ\text{K}]$	0.2 cm	$0.008 \cdot C [^\circ\text{K} \cdot \text{suns}]$

At 100 suns the thermal gap introduced by the PCB is negligible, while the epoxy adhesive introduces a ΔT of about 3.7 degrees. Moreover the temperature gap is hardly controllable due to the high variability in the thickness and uniformity

of the epoxy adhesive. Therefore, in this mounting system the thermal connection is not sufficient and it leads to cooling down problems above 50 suns in measuring the cells versus the concentration.

In order to overcome these cooling down problem we developed a new technique which substitute the epoxy adhesive with a metal solder. In the last cell prototypes, the back metal was substituted with a metal stack composed by Al/Pd/Ag. In this way the last metal layer on the back is silver, which can be easily paid in full with the PCB by means of tin solder. In this way no cooling down problems have been observed up to 100 suns light concentration.

5.3 Cell characterization methods under 1 sun

The cell performances are usually described in terms of some important quality parameters: J_{SC} , V_{OC} , FF and η . All the characteristic parameters may be extracted by measuring a current voltage characteristic under standard illumination conditions.

For measuring the current voltage characteristic, a voltage ramp is applied to the cell by using a power supply. While switching the external voltage, the current and voltage of the cell are measured continuously by using a four-probe measurement. During the current voltage measurement the cell is illuminated by a sun simulator and measured under the standard testing conditions (STC). The standard testing conditions define the measurement conditions e.g. temperature, spectrum, irradiation density, allowing a comparison between different solar cells. To characterize the solar cells under 1 sun standard conditions, a standard solar simulator (ABET Technologies SUN 2000 Solar Simulator) was used. The simulator is calibrated with a certificated *reference solar cell* (SRC-1000-TC-QZ) from VLSI Standards Inc., in accordance to the AM1.5G spectrum.

For terrestrial concentrator cells, there are no official international standard testing conditions. Three important testing laboratories (NREL, National Renewable Energy Laboratory, Colorado, USA; Sandia National Laboratories, New Mexico, USA and the Fraunhofer ISE, Germany) define the standard testing conditions for terrestrial concentrator cells as following:

- Cell temperature: 25 °C
- Total irradiance: 1000 W/m²
- Direct spectral irradiance: AM1.5D

5.3.1 Spectral mismatch

Although the standard testing conditions of concentrator solar cells suggest usage of the AM1.5D direct to characterize the concentrator cells, we used the AM1.5G global solar spectrum. This choice is principally due to the difficulty of finding commercial reference cells for the direct solar spectrum. Commonly the technique of the *spectral mismatch correction* can be used to overcome this problem [66]. In this technique, the spectral responsivity of the reference cell must be measured in order to calculate the spectral correction factor. However, the experimental determination of the spectral responsivity is obviously affected by the measurement uncertainty, which in our case is about 5%. As demonstrated in the following equations, the uncertainty in the spectral correction factor estimation is greater than the systematic error introduced by using the global spectrum instead of the direct one.

In order to estimate the systematic error on the J_{SC} introduced by using the global instead of the direct solar spectrum, the expected J_{SC} under the two spectra have been calculated. The experimental EQE of a standard front-side contacted solar cell was used to estimate the short circuit currents, under both the direct S_{SC}^{direct} and global S_{SC}^{global} spectrum:

$$J_{SC}^{global} = \int S^{global}(\lambda) \frac{\lambda q}{hc} EQE(\lambda) d\lambda \quad (5.2)$$

$$J_{SC}^{direct} = \int S^{direct}(\lambda) \frac{\lambda q}{hc} EQE(\lambda) d\lambda \quad (5.3)$$

$$(5.4)$$

The difference between the calculated short circuit currents is equal to 0.7%. The value is much lower than the error introduced by applying the spectral mismatch correction. This result validates the using of the global spectrum for the characterization of the developed concentrator cells.

5.3.2 Measurement errors at 1 sun

The total measurement uncertainty on the conversion efficiency can be estimated by considering the measurement errors on the current, voltage and incident irradiance. Using the equation for the efficiency η of the cell:

$$\eta = \frac{J_{mp} V_{mp}}{P_{inc} A_c}$$

the relative measurement error for the absolute efficiency can be estimated. This relative error is not avoidable in calibrating the solar cell at one sun. It can be

estimated as following:

$$\Delta V_{mp}/V_{mp} \approx 0.5\%$$

$$\Delta J_{mp}/J_{mp} \approx 2\%$$

$$\Delta P_{inc}/P_{inc} \approx 3\%$$

The error of the voltage is principally generated by the uncertainty in the determination of the cell temperature. The voltage uncertainty introduces also an error in the determination of the J_{mp} , which, in the maximum power point region, strongly depends on the voltage. However, the most important uncertainty is introduced by the incident irradiance estimation. The error of 3% in the incident irradiance value is due to the time constancy and the spatial uniformity of the beam intensity. The exposed area of the reference solar cell (4 cm²) is wider than the test cells (0.16 cm²), therefore high uncertainty is experienced in the irradiance determination for small-area devices.

Taking all above into account, if the spectral mismatch is neglected, the relative error in measuring the absolute efficiency at one sun is 3.6%.

5.4 Characterization methods under concentrated light

The IV curves under concentration are measured in the same way as the IV curve at 1 sun. The only difference is the light irradiance which is delivered onto the cell. In order to produce high incident irradiance with indoor solar simulator systems, there are two main techniques which can be used: flash pulsed solar simulator or continuous solar simulator. The last technique uses optics to concentrate the light produced by a continuous Xenon lamp on the solar cell under testing.

The concentrator solar simulator used in this work was developed by the Testing Lab of the Microtechnology Unit of the Bruno Kessler Foundation, and optimized during this work. The measurement setup allows for a concentration of the light from 1 sun up to 400 suns.

5.4.1 Measurement setup

With reference to the diagram in Figure 5.4, the proposed concentrator system is composed of a motorized diaphragm (1), a parabolic off-axis mirror (2), a biconvex

lens (3), a XYZ micropositioner (4) and a thermal cell holder (5) which holds the packed Cell (6).

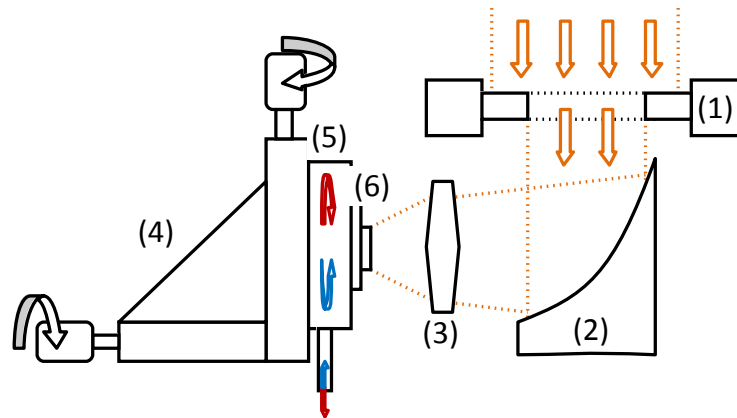


Figure 5.4: Synoptic Diagram of the Concentrator composed of a motorized diaphragm (1), a parabolic off-axis mirror (2), a biconvex lens (3), a micropositioner (4) and a thermal cell holder (5) which holds the packed Cell (6).

By combining the parabolic off-axis mirror with the biconvex lens, a fixed concentration ratio of more than 100 is obtained, and afterwards, working with the solar simulator at full power, irradiance equivalent to more than 400 suns over the $6 \times 6 \text{ mm}^2$ working area is achievable. In order to change the irradiance on the cell working plane, a diaphragm has been placed between the solar simulator and the optical system: by varying the diaphragm aperture, the final irradiance can be directly controlled. An advantage of using the diaphragm is that some beam parameters like uniformity, divergence and spectrum do not change with respect to the concentration factor. Moreover, the cell and optics remain at a fixed position during the whole efficiency-concentration curve acquisition. Only the diaphragm is moved by means of a stepper motor handled by a PC. It allows to automatically acquire the efficiency-concentration curve in only few minutes.

In general, the main problem while concentrating the beam of a conventional solar simulator is to obtain a uniform irradiance of the concentrated light. Fig 5.5 shows the beam irradiance map measured on the cell plane. The Abet solar simulator is equipped with a homogenizer filter constituted by an array of 4 by 4 lenses to uniform the irradiance for 1 sun measurements. The optical coupling between the homogenizer filter and the concentrating optics affects the beam uniformity. The measured max/min ratio in the irradiance map is 2 over the central $4 \times 4 \text{ mm}^2$ area.

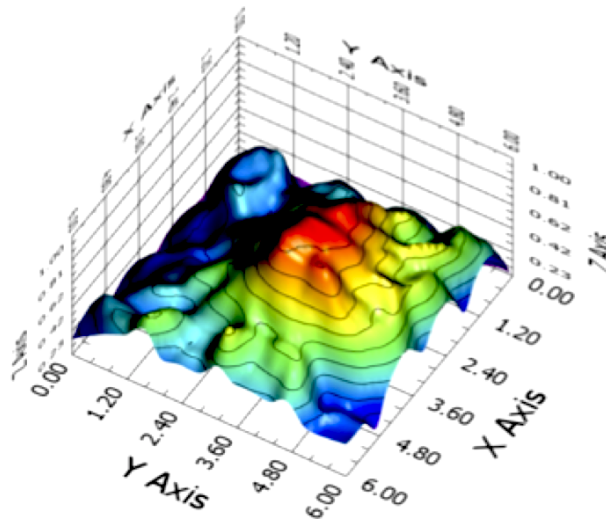


Figure 5.5: Irradiance Map in the focus plane of the biconvex lens.

5.4.2 Temperature control

Under high-concentrated light, the cell temperature increases very rapidly, since part of the radiation power is converted into heat. In order to maintain the cell temperature at the standard value of 25°C, a combination of two systems was used: a copper radiator with forced refrigerated fluid and a *Peltier cell* with temperature controller. Peltier cell is placed between the solar cell holder and the copper radiator. The controller, with a short feedback loop closed with the temperature probe in the back of the cell, allows controlling the temperature with fast response transient and high accuracy, while the copper radiator lets dissipate excessive heating.

As explained in Section 5.2, although the back of the PCB is kept at 25°C, the temperature of cell itself is commonly higher due to the thermal resistance of the package.

In order to correct this temperature gap, the so called *Voc-method* was used to measure the cell under concentrated light. The open circuit voltage is very sensitive to the variation of the temperature. Therefore, if the V_{OC} at 25°C is known, the cell exposed to concentrated light may be cooled down, until to its V_{OC} reaches the value measured at 25°. This assures a very precise control of the effective temperature of the cell.

5.4.3 Efficiency-concentration curves

In order to measure the IV curves under different concentration levels, the following steps are performed:

- Choosing the light intensity power (concentration factor) by setting the diaphragm aperture.
- Cooling down the cell to 25°C by means of the Peltier cell.
- Fast opening of the simulator shutter to illuminate the cell and measuring the V_{OC} as a function of the time by means of an oscilloscope. As the shutter is opened, the temperature of the cell (equal to 25°C at the moment of the shutter opening) increases and the open circuit voltage decreases very fast in the first milliseconds (see Fig. 5.6). The maximum value of the curve shown in the figure represents the V_{OC} of the cell at 25°C.
- Cooling down the test cell until the actual V_{OC} equals the value measured initially just after opening the shutter.
- Measuring the I-V curve of the test cell at 25°C.

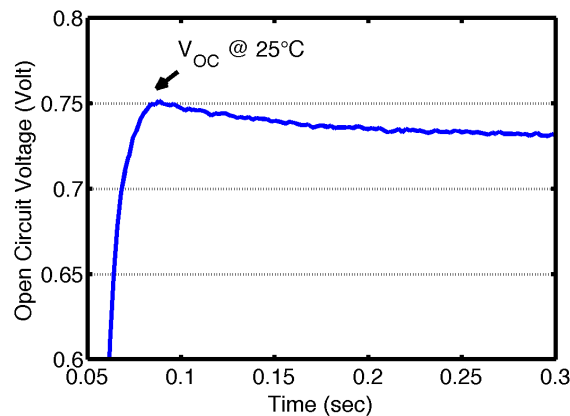


Figure 5.6: Dynamics of the open circuit voltage. The maximum point is the V_{OC} at 25°C, then the voltage decreases due to the cell heating.

The light concentration C can be calculated using the ratio of the measured J_{SC} under concentrated light and the calibrated one sun current $J_{SC,1-sun}$ of the test cell. Therefore, a linear dependence of the light intensity and the short-circuit current is assumed.

$$C = \frac{J_{SC}}{J_{SC,1-sun}} \quad (5.5)$$

5.4.4 Correction for the sub- and super-linear short circuit current effect

In Eq. 5.5 the concentration factor is estimated by assuming the linearity of the J_{SC} with respect to the concentration. However, numerical simulations in Section

4.4.3 predict a super-linear growth of the J_{SC} with the concentration factor for the cells based on low-resistivity substrate, and a sub-linearity of the J_{SC} for the cells based on high-resistivity substrates. The expected non-linear behavior of the J_{SC} introduces a bias in the concentration factor estimation.

In order to take into account the non-linearity effects in the efficiency-concentrator curves, a new and original technique has been developed. The simulated IQE of low-resistivity cells (shown in Fig. 4.21) indicates that the J_{SC} super-linear excess under concentrated light involves only red photons with wavelength larger than 600 nm. On the other hand, the short circuit current generated by photons with the wavelength shorter than 600 nm is perfectly linear with the incident power. The simulation results has been exploited to develop a new and simple method to measure the concentration factor without introducing any bias due to the non-linearity.

An optical low-pass filter is added in the solar concentrator system to eliminate the spectrum portion above 600 nm, so that the concentration factor C may be determined with the $J_{SC}^{filter} / J_{SC,1-sun}^{filter}$ ratio. After the concentration factor is measured, the filter is removed and the I-V curve is acquired. Figure 5.7 shows the measure spectral responsivity of the used low-pass filter.

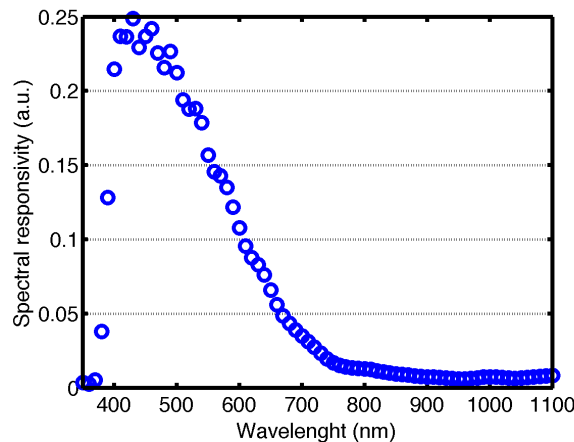


Figure 5.7: Experimental spectral responsivity of the low-pass filter used to eliminate the super-linearity effect on the concentration factor estimation.

In the high-resistivity solar cells, due to the simulated J_{SC} sub-linearity (see Fig. 4.19), a similar bias on the estimation of the concentration factor is also expected. The method described previously may also be used in this case. In fact, the filter reduces the beam total irradiance by 80% of its original value. Therefore, under filtered beam, the cell has a linear J_{SC} response with respect to the concentration, and the real concentration factor may be estimated as in the previous case. The method works well up to the concentration factor of 200 suns.

5.4.5 Measurement error

The relative error of the concentration factor is dominated by the $J_{SC,1-sun}$ uncertainty, equal to 3%. Using the equation for the efficiency η under concentrated light:

$$\eta = \frac{J_{mp} V_{mp}}{0.1C A_c}$$

and considering the uncertainty of the cell temperature due to the V_{OC} method equal to $\pm 3^\circ\text{C}$, the total relative measurement error for the absolute efficiency is estimated to be equal to 5%.

5.5 Determination of the series resistance

In Section 4.1 the series resistance R_s of a front-contacted solar cell was estimated by using analytical expressions for the series resistance components. In Section 4.2 the constant lumped series resistance R_s was added in the equivalent diode-model circuit of the solar cell (see Fig. 2.6) in order to predict the resistance losses of the cell under concentration. This model assumes that the series resistance is constant and does not depend by the light bias.

However, in general, the value of R_s depends on the operating condition of the cell, i.e. the external current density, external voltage and illumination intensity. Therefore, the series resistance of a solar cell should be determined with the cell working under real operating conditions. In the case of concentrator solar cells, this means that for an exhaustive characterization, the series resistance should be determined as a function of the concentration factor.

The illumination intensity may influence the series resistance of a solar cell in two principal ways:

- The maximum power point voltage V_{mp} increases with the illumination intensity. This effect causes the band bending across the p - n junction to be smaller at high illumination intensity than under low intensity. Thus, there is increased forward injection of electrons into the p -base when the cell is under high illumination intensity. As the electrons flow by diffusion in the base they do not suffer resistive losses and causes the total lumped series resistance (R_s) of the illuminated cell to decline [67].
- The photogenerated carrier densities Δp and Δn depend on the incident light power. When the cell base approaches the high-level injection condition ($\Delta n, \Delta p > N_A$) the generated carriers contribute to the carrier transport

and they have the effect to reduce the effective base resistivity. Also in this case the increased carrier density cause the resistance in the base to decline.

In conclusion, in order to correctly describe the parasitic resistance losses in concentrator solar cells, the total lumped series resistance must be described as a function of the concentrator factor $R_s(C)$.

5.5.1 Experimental methods

In the past years several experimental methods to determine the lumped resistance of a solar cell have been developed, and reviewed in [68]. Among these, a simple and reliable method that can be used to measure the total series resistance of a solar cell under different light intensities was proposed by Wolf in [69].

This method is based on the comparison of two IV-curves measured at different illumination intensities. This measure results in two shifts between the curves. The first shift is in current density, because the photogenerated current is proportional to the incident illumination power. The second shift is in voltage which is caused by the smaller series resistance loss, at a lower light intensity (see Fig. 5.8). Two points P_1 and P_2 , that lie at a fixed distance δI from the respective short circuit current are marked on the IV-curves (see Fig. 5.8). δI is chosen in such a way that the point P_1 is close to the maximum power point of its IV curve. By considering ΔV , the voltage difference between the two points P_1 and P_2 , the magnitude of the series resistance may be determined as:

$$R_s = \left| \frac{\Delta V}{\Delta J_{SC}} \right| \quad (5.6)$$

The Eq. 5.6 is derived on the basis of the multi-diode model. However the only assumption is that, the lumped series resistance R_s , the saturation currents J_{0k} , and the ideality factors n_k in the diode-model are the same at points P_1 and P_2 . This assumption is justified as long as ΔJ_{SC} is small. However, in order to minimize the measurement error, since the magnitude of ΔV depends on ΔJ_{SC} , the latter should not be too small. In this work a compromise is reached by choosing ΔJ_{SC} of the order of magnitude of J_{SC} . With this choice the uncertainty of the R_s measure is of about the 20% relative.

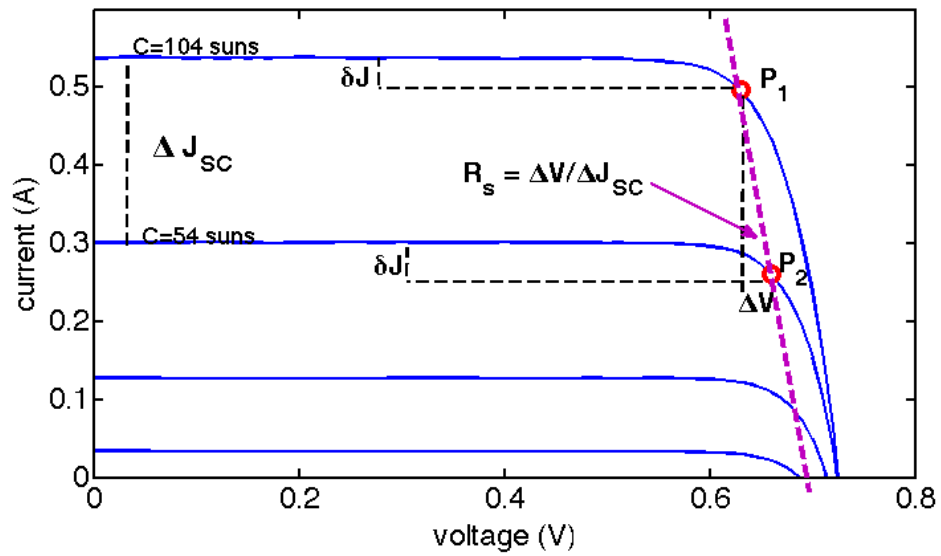


Figure 5.8: Determination of the series resistance as a function of the concentration level.

CHAPTER 6

Experimental characterization

In order to find an optimal design of the conventional front-side contacted cell structure, the experimental characterization of cells with different designs and fabrication splits is here reported. In particular, the role of the metal grid, finger pitch, texturing, substrate resistivity and BSF doping method, is here investigated, and the results are discussed. The cells performances are evaluated in terms of Conversion Efficiency (η), Open Circuit Voltage (V_{OC}), Short Circuit Current Density (J_{SC}) and Fill Factor (FF), measured under both 1 sun and concentrated light. As a result of this parameter optimization, a front-side contacted cell 23% efficient at 100 suns could be realized. Finally, the DEPC solar cells, introduced in Chapter 4, are characterized and discussed.

6.1 Cell characterization under concentrated light

In order to measure the cell conversion efficiency versus concentration, the cells have been packaged as described in Section 5.2. After mounting the cells, the light IV curves in standard test conditions are measured under both 1 sun and concentrated light. The IV curves under concentration are determined by using the measurement setup described in Section 5.4.

Figure 6.1 shows the efficiency-concentration curve measured on a typical cell (sample with code PVT160m4H). This cell, based on the 0.5 Ωcm silicon substrate,

has rectangular front metal grid $4 \mu\text{m}$ thick, finger spacing equal to $180 \mu\text{m}$ and planar (non-textured) surface.

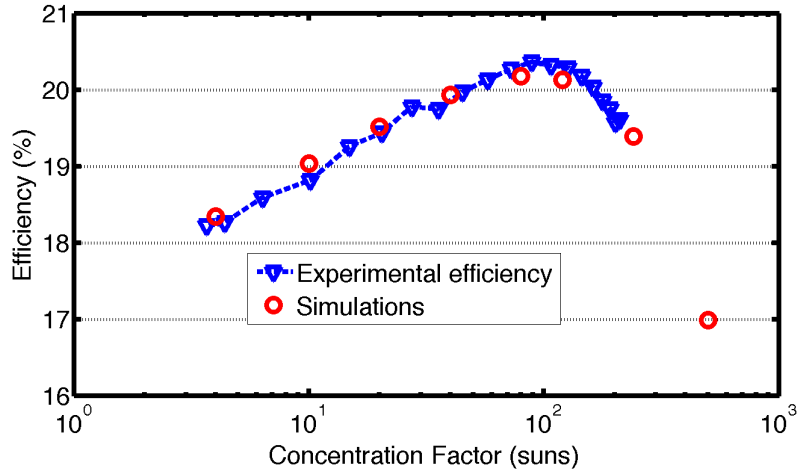


Figure 6.1: Efficiency as a function of the Concentration level. Experimental data (blue open triangles) and simulations (red open circles).

Numerical simulations, calibrated on the specific cell design, are represented in Fig. 6.1 with red circles. The experimental efficiency and the simulated one are in line in all the concentration range. It should be noted that there was no parameters fitting done to match experimental data with simulations. In fact, all the parameters used in the simulation have been measured independently of the solar cell characterization results. Only the finger width and the total weighted reflectance have been tuned, within the experimental uncertainty range, in order to reproduce the J_{SC} at 1 sun. In this simulation the finger width and the WR of the SiO_2 ARC were set to $7 \mu\text{m}$ and 16.5% respectively.

The efficiency of the cell peaks at concentrations between 80 suns and 120 suns before decreasing. The drop at higher concentrations is due to FF losses. Figure 6.2a shows the FF as a function of the concentration factor. The FF drops at concentration factors higher than 80 suns due to the series resistance of the solar cells. For analyzing this effect, the normalized J-V curves, measured under concentrated light are plotted in Figure 6.2b. The current drop in the right part of the I-V curves is strictly correlated to the parasitic series resistance losses.

In order to estimate the total series resistance of the solar cell the method described in Section 5.5 was used. The I-V curves, measured at different concentration factors, are used to estimate the series resistance under concentrated light. The results are shown in Fig. 6.3. The series resistance results almost independent of the concentration factor and the mean value is $0.019 \pm 0.002 \Omega \cdot \text{cm}^2$. The expected

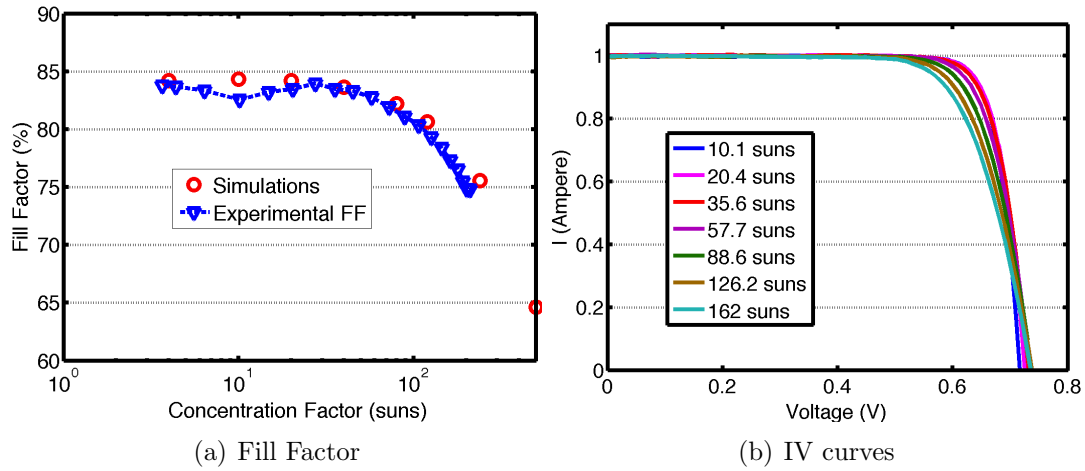


Figure 6.2: The experimental Fill Factor (blue triangles in fig. a) decreases for concentration factors above 80 suns, as predicted by simulations (red circles) due to the series resistance losses in the cell, as inferred from the behavior of the normalized I-V curves measured at different concentration factors (fig. 2)

series resistance value, calculated in Section 4.1 by means of the *lumped resistance approximation* is of $0.023 \Omega \cdot \text{cm}^2$, very close to the measured value.

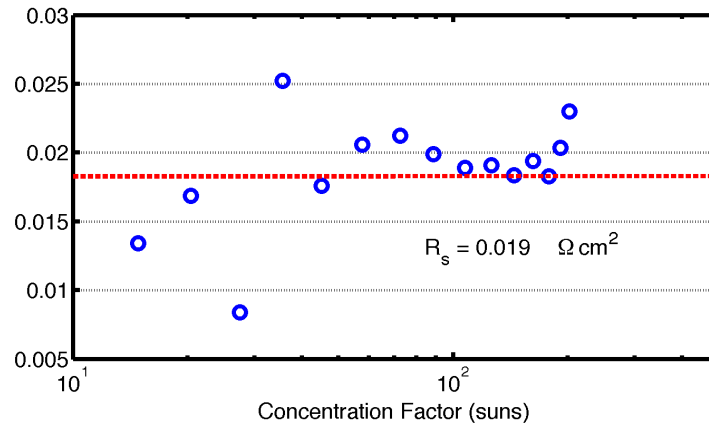


Figure 6.3: Series resistance of the PVT160m4H cell, measured at different concentration factors.

6.2 Front metal grid and surface texturing

Some of the cell parameters were varied in the design of the fabricated cells: geometry of the front metal grid, finger spacing, metal thickness and the surface texturing. Moreover, cells with both planar and textured surface have been fabri-

cated for testing. In the following, efficiency trends with respect to these parameters are discussed.

6.2.1 Metal grid and finger spacing

In Section 4.4.1 two different metal grid designs have been investigated to be used in our front-contacted solar cells: the rectangular and the square grid (see Fig. 3.4). Both the designs have been optimized in terms of finger spacing and metal thickness to operate under 20 and 160 suns. The results, listed in Tab. 4.5, show that the maximum efficiency under 160 suns is reached by using a 4 μm thick square metal grid with 180 μm wide finger spacing.

Cell with different finger spacings, metal thickness and metal grid geometries have been fabricated. More detail about the layouts parameters are listed in Table 6.1. Numerical simulations (Section 4.4.1) indicate that the layout PVT160m4+ is the best solution for 160 suns concentrated light, while the sample PVT20m4+ represents the layout maximizing the efficiency at 20 suns (see Fig. 4.16). All these samples have been fabricated on FZ silicon substrate with 0.5 Ωcm resistivity.

Table 6.1: Fabricated layout split

layout code	Grid design	Metal Thickness	Finger spacing
PVT20m4H	rectangular	4 μm	360 μm
PVT160m4H	rectangular	4 μm	180 μm
PVT160m4+	square	4 μm	180 μm
PVT160m2+	square	2 μm	180 μm

Table 6.2: 1 sun characterization

sample code	J_{SC} (mA/cm ²)	V_{OC} (mV)	FF (%)	Efficiency (%)
PVT20m4H	33.8	641	83.1%	18.2%
PVT160m4H	33.0	640	82.8%	17.9%
PVT160m4+	32.9	641	82.9%	17.8%
PVT160m2+	33.1	641	82.9%	17.8%

The cells characterization under 1 sun is reported in Table 6.2. All the cells have very high FF and V_{OC} , and they have comparable efficiency values, within the measurement confidential bounds. However, the PVT20m4H cell, shows a significantly higher short circuit current under 1 sun. This difference in J_{SC} is doubtless due to the lower front metal shadowing. In fact, this cell layout was optimized to work

under 20 suns and it has larger finger spacing than the other layouts. Therefore, the shadow losses in this cell are reduced.

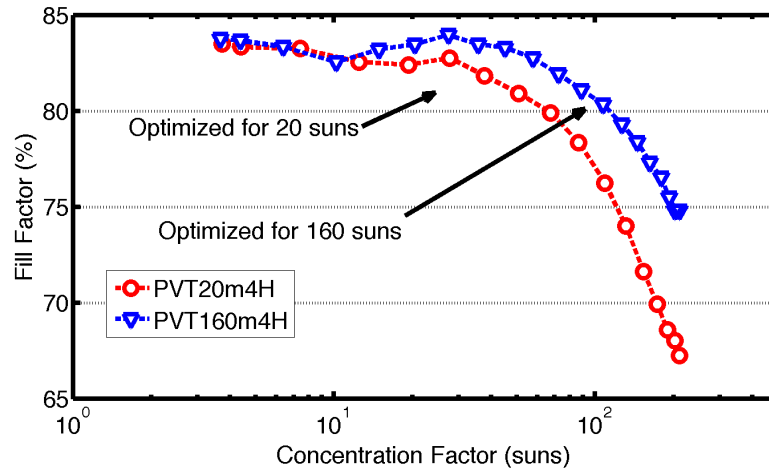


Figure 6.4: Fill factor of cells with different finger spacings. The two samples were optimized to maximize the conversion efficiency under 20 suns (red circles) and 160 suns (blue triangles) respectively.

Although under 1 sun all the cell have almost the same efficiency, under concentrated light the differences in terms of conversion efficiency among the different cells are shown to be significant. In Figure 6.4 the fill factor of solar cells with different finger spacing is reported. It can be noted that the smaller the grid finger distance is, the higher the FF at high incident irradiation is. The effect is due to the series resistance: a shorter finger spacing results in lower series resistance losses in the metal grid, leading to higher FF under high concentration levels.

The plot of the efficiency versus the concentration is shown in Figure 6.5. It can be seen that the cell with smaller grid finger distances peaks at higher concentration levels. This is exactly what expected, since the PVT20H4m and the PVT160m4H are designed to maximize the efficiency at 20 suns and 160 suns respectively.

In addition to the finger spacing, the effects of the metal grid geometry and of the metal thickness were investigated. Fig. 6.6 shows the efficiency versus the concentration for cells with both rectangular and square grid geometry and with 4 and 2 μm thick metal. The best result is obtained by the PVT160m4+ sample, which uses square metal grid and 4 μm thick metal, as well predicted by the simulations (see Section 4.4.1). The obtained improvement consists in an increase of 0.6 absolute percentage points in the conversion efficiency. Also in this case, the improvement is due to the less resistance losses into the metal grid, due to thicker metal fingers and to the shorter resistive path length experienced by the current in the square

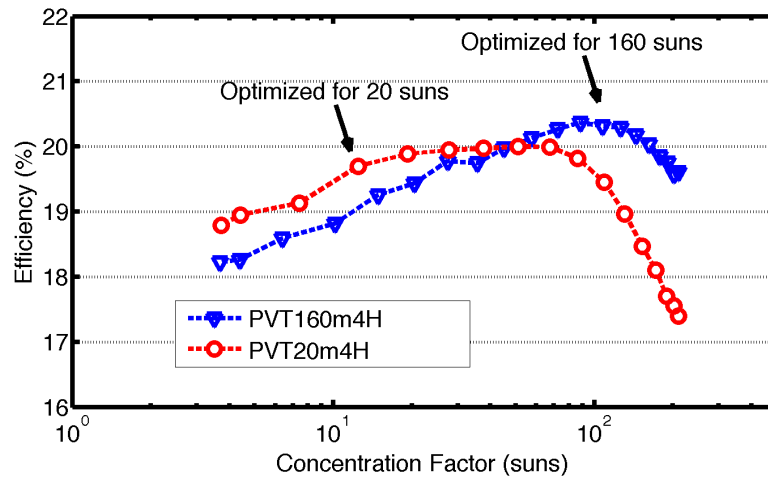


Figure 6.5: Conversion efficiency cells with different finger spacings: $160 \mu\text{m}$ (blue triangles), and $350 \mu\text{m}$ (red circles). The two cells are optimized to maximize the conversion efficiency under 160 suns and 20 suns respectively.

metal grid.

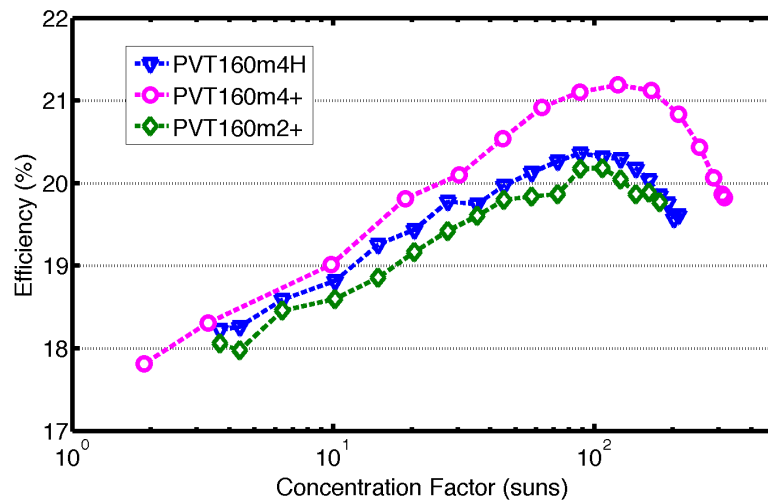


Figure 6.6: Efficiency of solar cells with rectangular and square metal grids and with two different thicknesses of the metal fingers.

In conclusion, it has been shown that thick metal and square geometry of the front metal grid are effective solutions to increase the conversion efficiency under concentrated light. While, as regard the finger pitch, it has been shown that it has the role to control the concentration level in which the efficiency peaks. Therefore it must be tuned (as discussed in Section 4.2) by considering the concentration factor under which the solar cell will work.

6.2.2 Surface texturing

In Section 3.4, it has been demonstrated that the surface texturing is very effective for achieving a reduction of the front reflectance. In particular, the weighted reflectance of our optimized textured surface coupled with the SiO₂ ARC, was measured equal to 6.8%, the 10% lower with respect to cells with planar surface. On the other hand to fabricate textured cells one more lithographic mask is required. In the following, the characterization results of two cells, fabricated on a 0.5 Ωcm *p*-doped wafer with rectangular metal grid 4 μm thick and with both planar and textured surface are reported. In Table 6.3 the characterization results, under 1 sun, are listed, while in Figure 6.7 the efficiency-concentration curves are plotted.

Table 6.3: 1 sun characterization of cell with both planar and textured surface

Sample code	Surface	J_{SC} (mA/cm ²)	V_{OC} (mV)	FF (%)	η (%)
PVT160m4H	Planar	33.0	640	82.8%	17.9%
PVT160m4HT	Textured	35.6	638	83.4%	18.9%

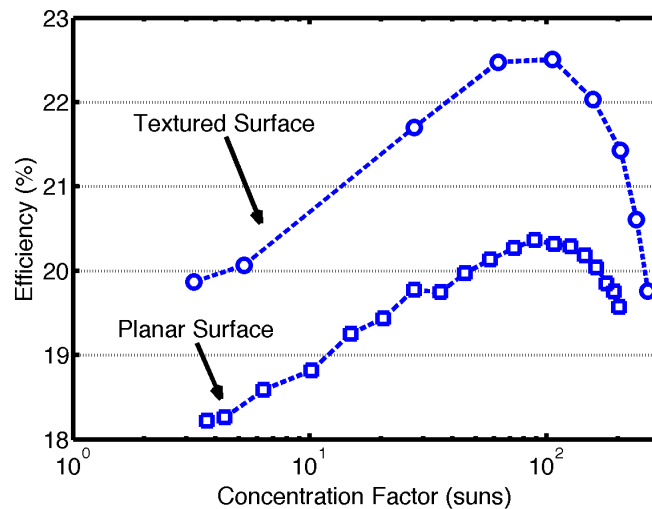


Figure 6.7: Efficiency as a function of the concentration of solar cells with planar and textured surface.

The efficiency of textured cell is higher than the planar one under both one sun and concentrated light. It reaches the maximum value of 22.5 % at 100 suns. The efficiency increase is due to an equivalent increase of the J_{SC} (see Tab. 6.3). The latter can be completely explained in terms of the front surface reflectance reduction. In Section 3.4 the weighted reflectance of textured and planar surfaces

was measured equal to 6.8% and 16.8% respectively. It can be noted that the texturized cells do not show any drop in V_{OC} and FF under one sun or under concentration. Such a result confirms that the texturing does not affect neither the cell series resistance nor the recombination rate and the surface passivation. This was also demonstrated in Section 3.4.2, where, the measured J_{0e} results comparable for both textured and planar silicon n^+ -doped surfaces.

6.3 BSF boron doping

In order to obtain an effective Back Surface Field (BSF), two different doping techniques have been tested: solid source doping and ion implantation. The sheet resistance of BSF obtained with both techniques is about 150 Ω/sq .

As described in section 3.2, the solid source doping technique requires two more thermal treatments in order to form the BSF. The first one is required for the boron-deposition, while the second drives-in the dopant and grows a protective SiO_2 layer. On the other hand the ion implantation avoids these two thermal treatment, because the implantation step is performed at low temperature through an oxide layer and the boron dopant is activated at a later stage, together with the emitter diffusion.

Even though the sheet resistivity of the boron doped layer reached with both techniques is very similar, the performances of the final solar cells are considerably different. Table 6.4 reports the 1 sun characterization, while in Figure 6.8 the efficiency-concentration curves are plotted. Both the cells characterized in this section are fabricated on 0.5 Ωcm substrate and they have square metal grid 4 μm thick and textured surface.

Table 6.4: 1 sun characterization of cells doped with solid-source and ion implantation

Boron doping	J_{SC} (mA/cm ²)	V_{OC} (mV)	FF (%)	η (%)
Solid-source	33.0	632	82.9%	17.3%
Implanted	35.6	640	83.2%	18.9%

The conversion efficiency of the sample doped by means of solid source is significantly lower than the one of the implanted cell. This difference is due to a drop in the short circuit current J_{SC} and in V_{OC} , as inferred by Tab. 6.4. The reasons of this drop are more deeply investigated in the next section.

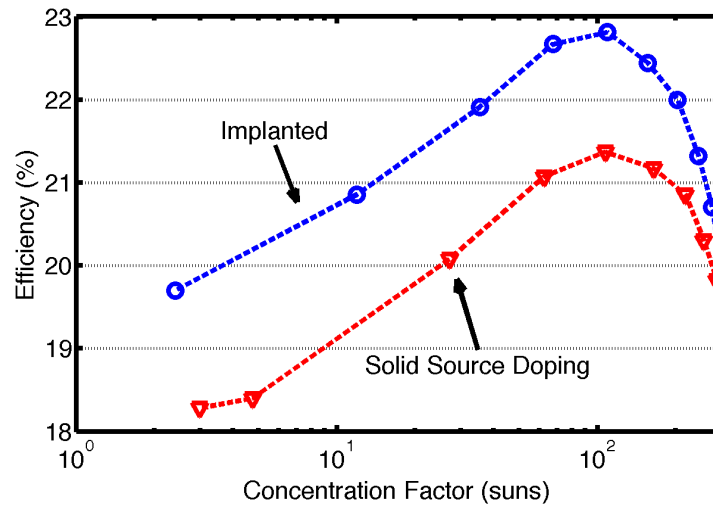


Figure 6.8: Efficiency as a function of the concentration of solar cells with BSF obtained by means of boron solid-source doping (red curve) or ion implantation (blue curve).

6.3.1 Light induced decay

In order to further investigate the J_{SC} drop in solid-source boron doped solar cells, the short circuit current under light bias was continuously sampled during the exposition time. The results are shown in Figure 6.9. The normalized J_{SC} of both the implanted and the source-doped cells was sampled for several minutes. Figure 6.9 shows that the J_{SC} of the solid source-doped cell decays with the exposure time (power of 0.1 W/cm^2), and after 60 seconds it is decreased of about 6%. After this initial drop, the output remains stable. The effect is completely reversible and the cell performance recovers under 12 hours in the dark at room temperature. A similar decay was observed also for V_{OC} . As shown in Tab. 6.4, the efficiency loss is due to a decrease in the short-circuit current density, and to a smaller decrease in open-circuit voltage. The two effects completely explain the efficiency gap between the implanted and the solid-source doped solar cells.

This degradation effect also occurs in the dark, when minority carriers are injected (e.g., by a forward-biased solar cell), leading to the important consideration that the degradation is caused by excess charge carriers and not directly by photons. [5,6]

From a physical point of view the observed light induced decay (LID) may be correlated to a carrier lifetime degradation into the silicon bulk. To investigate this effect, during the fabrication process, the lifetime of the process wafers was monitored after each thermal or doping step. The effective carrier recombination

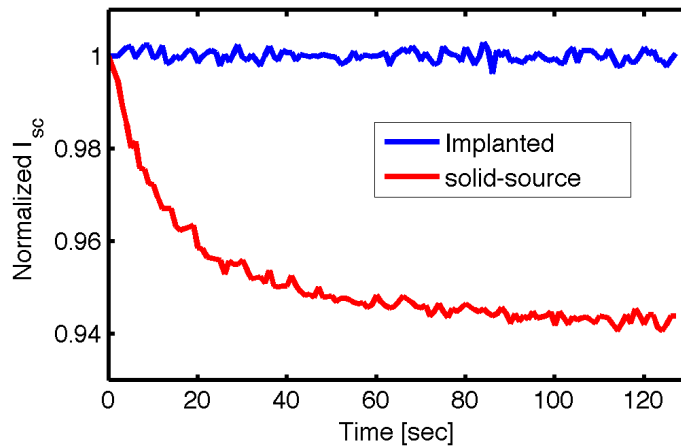


Figure 6.9: Short circuit current sampled during the exposure time. The solar AM1.5G spectrum with 0.1 W/cm^2 total irradiance was used.

lifetime of the process wafers was measured by means of the contactless quasi-steady-state photoconductance method, as described in Section 3.3. With reference to the fabrication process flow shown in Fig. 3.5, the effective lifetime of both solid-source doped and implanted wafers was measured after the main steps in the fabrication process. The results are shown in Fig. 6.10. The effective lifetime here reported is calculated at a minority carrier concentration of 10^{15} cm^{-3} .

After the boron doping step, the minority lifetime of both implanted and solid-source doped wafers decays. However, after the surface passivation, the effective lifetime of the implanted wafer is recovered and it equals its original value, while the lifetime of solid-source doped wafer is no more recovered in the following process steps. This result confirms that the low performance of solid-source doped cells may be related to lifetime degradation.

It should be noted that during the lifetime measurement by means of the photoconductance method, the cell is illuminated with a high-power flash lamp (equivalent to hundreds of suns). Therefore the measured lifetime corresponds to the cell under illumination conditions, i.e. when the LID effect occurs. Very high correlation was found among the effective lifetime and the final performance of the cells. Figure 6.11 shows the final V_{OC} and J_{SC} of many wafers, measured after light exposure, as a function of the lifetime value measured just after the emitter passivation. The solid-source doped cells show lower performance in terms of V_{OC} , J_{SC} and lifetime. This result indicates that the LID effect is related to the degradation of the lifetime under illumination.

The LID effect was observed only in solid-source doped low-resistivity ($0.5 \text{ } \Omega\text{cm}$)

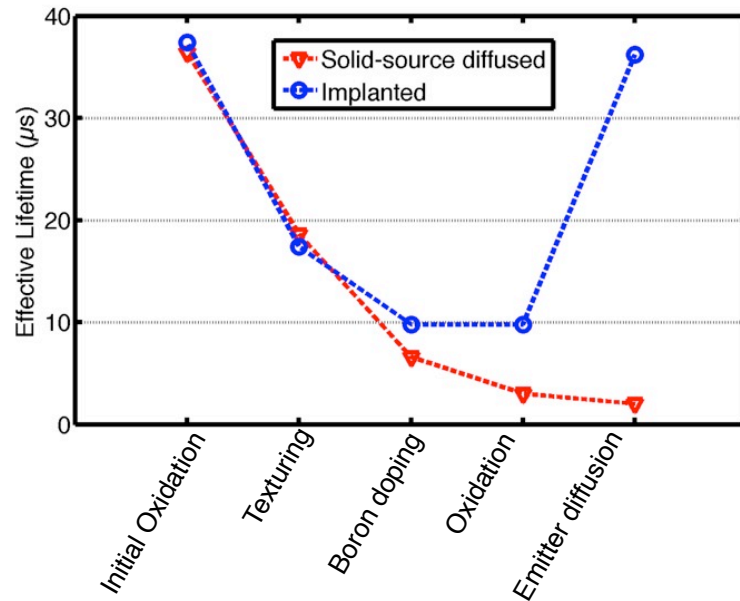


Figure 6.10: Effective minority carrier lifetime at 10^{15} cm^{-3} carrier density, measured after the principal steps in the fabrication process. The wafer doped by means of solid-source diffusion suffers from lifetime degradation.

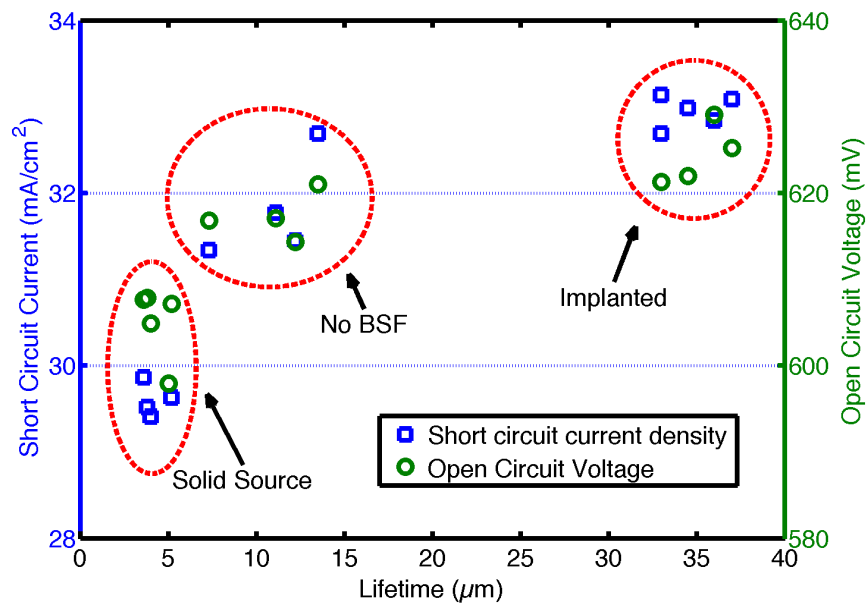


Figure 6.11: Open circuit voltage and short circuit current of boron-doped cells (implanted and solid-source doped) and undoped cells, as a function of the effective lifetime measured just after emitter doping and surface passivation.

FZ wafers. The same experiment performed on 10 Ωcm Cz silicon wafers, did not result in any LID effect. This result can be due to the different boron concentration content as explained in the following.

Analysis of the LID effect

Carrier lifetime instabilities in boron-doped silicon solar cells under illumination have been extensively investigated in the past and several distinct phenomena have been reported. One of the effects most frequently investigated is the degradation of the carrier lifetime as a consequence of illumination in boron-doped Cz silicon [70]. This effect was explained with presence under light exposition of boron-oxygen defects: lifetime reducing recombination centers, made up of one interstitial boron and one interstitial oxygen atom, are created under illumination. The effect was observed only in Cz silicon and never in FZ silicon, because large concentrations of oxygen are practically unavoidable in Cz silicon due to the partial dissolution of the silica crucible during the growth process. In fact, the experiments showed that gallium-doped and phosphorus-doped Cz silicon as well as oxygen-free FZ silicon samples did not present any lifetime degradation effect, which is thus exclusively linked to the simultaneous presence of boron and oxygen in the material [71]. Many experiments show that the light-induced lifetime degradation effect due to the boron-oxygen defects is fully reversible only by means of thermal annealing above 200°C [70][72][73].

Another effect, which shows similar light-induced carrier lifetime degradation in boron-doped silicon, is due to the dissociation of iron-boron pairs and is, therefore, linked to the degree of iron contamination in the material [74]. Since interstitial Fe in Si acts as an efficient recombination center, Iron is one of the most important contaminants in silicon-based integrated circuit and solar cell technology. The presence of interstitial iron Fe_i in silicon can dramatically reduce the n -carrier lifetime, even at very low concentrations.

In boron-doped silicon, at room temperature in thermal equilibrium all Fe_i is present as FeB pairs. FeB pair dissociation can be accomplished by illumination at room temperature or by minority carrier injection, or by increasing temperature which shifts the equilibrium state of Fe_i and B to isolated ions. The isolated and paired form of interstitial iron have markedly different recombination properties. This leads to significant changes in carrier lifetime and diffusion length after dissociating the FeB pairs [75].

The effects of the light induced decay due to the iron-boron pairs dissociation was observed in Cz silicon solar cells. In Ref. [30] is reported that Cz silicon solar

cells can lose 3% – 4% relative of their initial efficiency after exposure to light, after minority-carrier injection during dark forward bias, or after thermal treatment at 100 – 400°C. A rapid decreasing in efficiency (30 min at 1 sun) was also reported. The decreasing time is more rapid with respect to the decay time due to boron-oxygen defects, which requires several ours to reach stability. Moreover, in contrast to the boron-oxygen correlated lifetime degradation, which can be recovered only with thermal annealing above 200°C, the lifetime degradation due to iron-boron dissociation is completely reversible in few hours in the dark at ambient temperature.

Although LID effect on FZ silicon solar cells has never been reported in literature, the iron-boron pairs can also be observed in iron-contaminated boron-doped FZ silicon and is not restricted to Cz silicon, like in the case of boron-oxygen defects.

In conclusion, the LID effect observed in our 0.5 Ωcm FZ silicon solar is consistent with the presence of iron contaminations. In fact, the observed decay time of the J_{SC} , the amount of the J_{SC} reduction and finally the fact that J_{SC} recovers after few our in the dark without requiring any thermal annealing, are in perfect accord with this hypothesis.

However, due to the high-quality of our FZ silicon wafers, no Iron contamination is expected. Moreover in our experiments the LID effect was observed only in solid-source doped wafers and not in implanted ones. This leads to the conclusion that iron contamination is not contained in the bulk wafers, but the contamination could occur during the doping step, due to the contamination of the furnace or of the solid boron sources. Very low Fe concentrations in the 10^{10} cm^{-3} range are sufficient to degrade the cells, as reported in [76].

In our experiments the LID effect was observed only in 0.5 Ωcm FZ silicon wafers and not in the 10 Ωcm Cz ones. This effect could be due to two reasons: the first one is related to the boron density content into the substrate. In fact, 10 Ωcm Cz wafers contain much less boron dopant atoms than 0.5 Ωcm wafers (10^{15} versus $3 \cdot 10^{16} \text{ cm}^{-3}$), consequently the expected FeB concentration is reduced [77]. A second reason may be that while the recombination in the high-quality FZ wafers is dominated by FeB and Fe_i recombination rate, Cz wafers could present other dominant recombination channels: defects, other impurities, surface recombination. Therefore the recombination per FeB and Fe_i center would be reduced and a lower effect of the dissociation on the effective lifetime is expected.

The hypotheses of iron contaminations in our FZ solar cells, and the consequently LID effect should be further investigated. The detection of iron in Si at a level of 10^{12} cm^{-3} or less is not possible by secondary-ion-mass spectroscopy

(SIMS). However, another possible method to obtain an overall measure of defect concentration is to measure the minority-carrier lifetime or the minority-carrier diffusion length. The difference of the inverse lifetimes measured after and before light degradation may be evaluated to calculate the effective concentration of defects. Moreover a detailed analysis of the injection level dependence of the carrier lifetime change using the Shockley–Read–Hall theory may be used to estimate the energy level of the recombination centers [78].

6.4 Substrate resistivity

In order to investigate the effect of the substrate resistivity on the cell performance, different silicon wafers were used in the fabrication process: 10 Ωcm Cz silicon and 0.5 Ωcm FZ silicon. The cells characterization under 1 sun illumination is reported in Table 6.5.

Table 6.5: 1 sun characterization of cells with different base resistivity

Base resistivity	J_{SC} (mA/cm ²)	V_{OC} (mV)	FF (%)	η (%)
0.5 Ωcm FZ	35.6	640	83.2%	18.9%
10 Ωcm Cz	36.7	576	76.6%	16.2%

It can be noted that the V_{OC} of the 10 Ωcm solar cell is much lower than the one of the cell based on 0.5 Ωcm substrate. The drop in the V_{OC} of the lightly doped cell may be related to the doping of the BSF, as explained in the following. Unfortunately, the sheet resistance of the BSF doped region, measured on both the cells, is much higher than the expected. The obtained sheet resistance is ~ 150 Ω/sq while, as demonstrated in Section 4.4.2, the best results can be obtained when sheet resistance less than 50 Ω/sq is used.

The effect of high sheet resistance on the final cell performance is to reduce the V_{OC} . The V_{OC} reduction is expected to be much more pronounced in the 10 Ωcm base materials than in 0.5 Ωcm (see Fig. 4.18), and it is clearly visible in the experimental V_{OC} difference between the two samples shown in Table 6.5.

Due to the low dopant concentration, the diffusion length of 10 Ωcm silicon is expected to be higher than the diffusion length of 0.5 Ωcm wafer. In fact, the experimental IQE of the cell on the lightly doped substrate results higher than the IQE of the highly doped substrate as shown in Fig. 6.12. The enhancement in the IQE comports also an enhancement in the J_{SC} . In fact, the short circuit current density under 1 sun is 36.7 mA/cm² for the 10 Ωcm cell and 35.6 mA/cm² for the

0.5 Ωcm cell. In spite of the higher J_{SC} under 1 sun illumination, the total efficiency of the lightly doped cell is lower than the efficiency of the highly doped substrate. This is mainly due to the drop in the open circuit voltage.

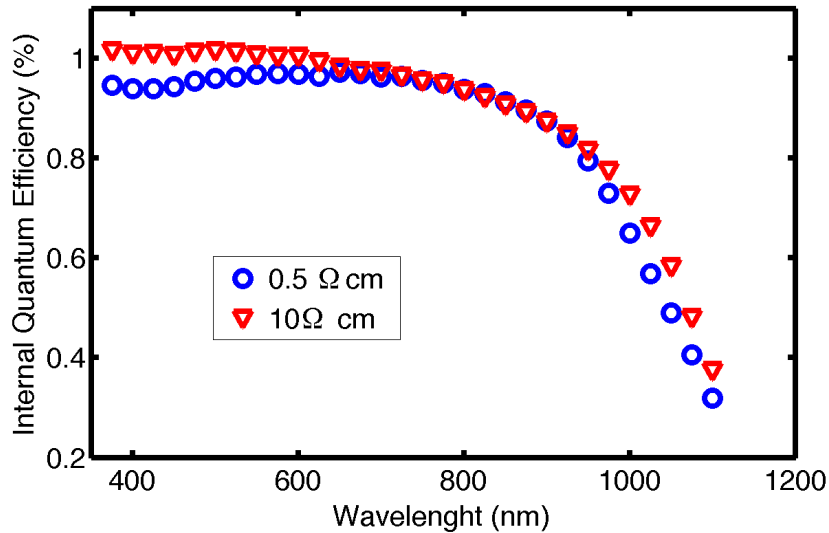


Figure 6.12: IQE of cells fabricated on 0.5 Ωcm and 10 Ωcm substrates. The IQE of the cell fabricated on the lightly doped substrate is higher than the IQE of the cell fabricated on highly doped substrate. This is due to the longer diffusion length of the first cell.

In Figure 6.13 the fill factors (a) and the total series resistances R_s (b) of both the cells versus the concentration are presented. The fill factor of the 10 Ωcm cell is much lower than the fill factor of the 0.5 Ωcm cell, because series resistance of the lightly doped substrate is higher than the resistivity of the highly doped substrate. It can also be noted that the FF of the lightly doped cell reach a minimum at about 60 suns, then it increases at higher concentration levels in contrast with the behavior of the 0.5 Ωcm cell. The behavior of the FF of the lightly doped cell can be explained by the dependence of the base resistance on carrier-injection. As explained in Section 4.3.4, the 10 Ωcm cell is in high-level injection for concentration levels over 10 suns. Under high-level injection the base resistivity is determined not by the material resistivity, but by the generated carrier densities. Therefore the base resistivity decrease with light intensity increasing. The series resistance decrease in lightly doped materials is showed in Figure 6.13b, in which the total series resistance of the two cells is plotted as a function of the concentration factor. The series resistance of the highly doped cell is almost constant with the concentration, while the one of the lightly doped cell rapidly decreases with the concentration and both cells converge at about 200 suns. The series resistance drop of the 10 Ωcm cell

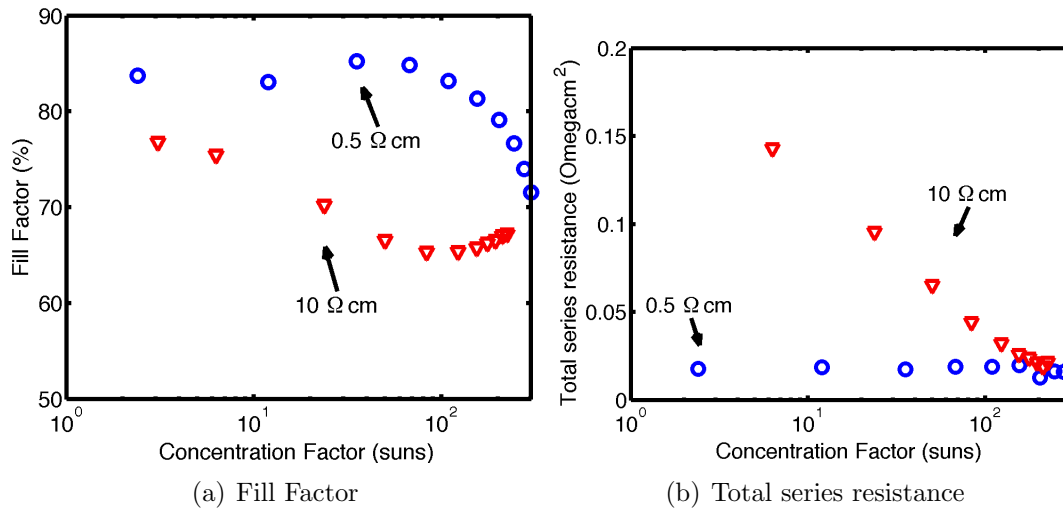


Figure 6.13: Fill factor (a) and total series resistance (b) versus the incident irradiation density for lightly and highly doped substrates.

under high illumination power is the reason of the FF growing in the range 60-200 suns, shown in Fig. 6.13a (red triangles).

Figure 6.14 shows the efficiency-concentration curves of both the 10 Ωcm cell and the 0.5 Ωcm cell. The first cell shows lower efficiency in the whole concentration range. The efficiency peaks at a concentration factor (about 20 suns) much lower with respect to the highly doped cell. The different shapes of the efficiency-concentration curves between the 10 Ωcm and the 0.5 Ωcm cells can not be justified with the series resistance of the substrate, because, as shown before, at 200 suns the two cell have almost the same total series resistivity (see Fig. 6.13b). In the following this behavior is explained in terms of J_{SC} reduction under concentrated light.

Short circuit current non-linearity

In Section 4.4.3 , numerical simulations show that, under concentrated light, the performance of the 280 μm thick 10 Ωcm substrate based solar cell is mainly limited by a strong J_{SC} sub-linear response with the concentration factor. At 200 suns in fact, the short circuit current of the cell is expected $\sim 9\%$ lower than the value predicted assuming a linear relationship between J_{SC} and concentration factor. On the other hand a non-linear response was predicted by numerical simulations also for 0.5 Ωcm cells, but in this case a super-linear response is expected. In fact, in the case of low resistivity cells, simulations shown at 200 suns a J_{SC} super-linear excess of about 5%.

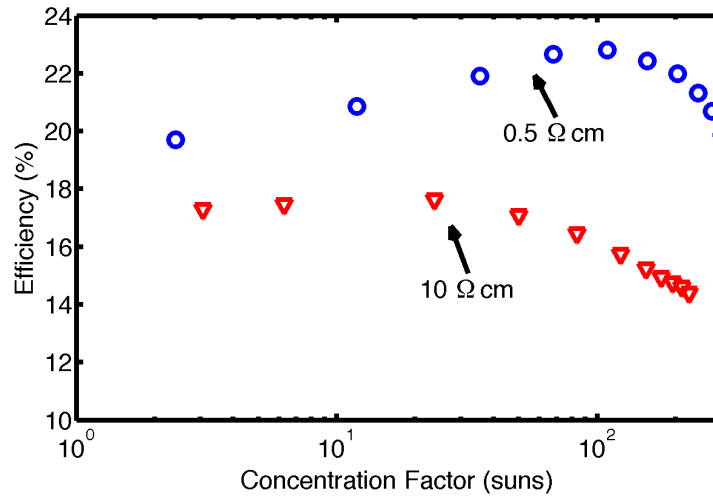


Figure 6.14: Comparison of the conversion efficiency between the cell fabricated on 0.5 Ωcm and the one based on 10 Ωcm substrate.

Figure 6.15 shows simulated and experimentally measured J_{SC} non-linearity for both the highly and the lightly doped cells. In both the cells, the J_{SC} at low concentrations grows linearly with the incident power, but for high concentration factors the J_{SC} of the highly doped cell features a super-linear excess reaching 5%, while the cell with the lightly doped base features a sub-linear current loss of about 15%. This effect is fairly described by simulations. However, in the case of lightly doped cell, a mismatch among the experimental and simulated J_{SC} can be observed at high concentration levels. This disagreement may be due in part to the measurement method used to calculate the concentration factor (see Section 5.4.4). When the J_{SC} of a solar cell is strongly sub-linear, this method may introduce a bias in the measurements, underestimating the concentration factor.

In conclusion, the worse performance of solar cells fabricated on 10 Ωcm silicon substrate with respect to the cell fabricated on the 0.5 Ωcm substrate, may be only in part attributed to the series resistance losses due to the high-resistivity of the bulk. In particular, the series resistance losses in the bulk limit the conversion efficiency in low concentration range (up to 100 suns), whereas under high concentration, a more fundamental limit of the efficiency is due to the J_{SC} sub-linearity effect.

6.5 Characterization of DEPC solar cells

Solar cells based on Cz 10 Ωcm substrate show a substantial drop in the conversion efficiency. This effect is mainly due to series resistance losses and J_{SC} sub-linearity effect. In order to overcome these limits, in Section 4.4.4 a new cell structure was

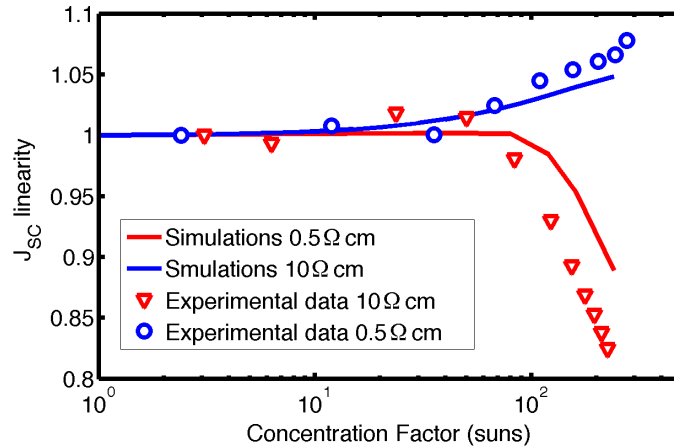


Figure 6.15: The simulated (solid lines) and the experimental (symbols) non-linear excess short circuit current. The highly doped cell features a super-linear excess reaching 5% at 200 suns, while the lightly doped cell shows a more pronounced short circuit loss of 15% at 200 suns.

proposed, based on Deep Etched P-Contacts (named DEPC solar cells). In order to test this design, a set of DEPC cells with different layouts have been fabricated on 10 Ωcm, 280 μm thick Cz silicon substrate. The best metal grid and finger spacing, as determined in previous sections were used (square metal grid 4 μm thick, 180 μm finger spacing, textured surface).

The deep-grooved contacts consist of a hole matrix, which is deeply-etched in the silicon substrate starting from the back surface. The holes are etched by means of a deep reactive-ion etching process (DRIE). Figure 6.16 shows the back surface of the wafer after the holes etching. The grooved-holes have diameter of 12 μm and they go through the silicon substrate before they stop very close to the front surface. The internal side of the holes is doped by means of solid-source diffusion, therefore they act as low resistance current paths to drain the *p*-carriers from the front surface, where are generated, to the back surface. As a final result, the deeply-etched holes have the effect of reducing the “effective thickness” of the solar cell.

Two parameters have been varied in the cell layout: the spacing between the holes h_s , and the depth of the holes h_d . In particular two different hole spacings have been tested: 180 μm (equal to the finger spacing) and 90 μm. The holes depth can be controlled simply by tuning the etching time. Cells with 200 μm and 260 μm deep holes have been fabricated for testing.

The efficiency of the DEPC solar cells were measured as a function of the concentration factor. The results are shown in Fig. 6.17. The efficiency of a standard cell (without deep grooved-contacts but fabricated on the same 10 Ωcm and with

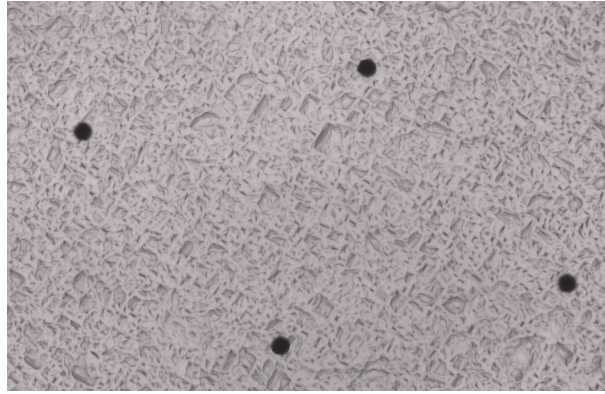


Figure 6.16: Deep etched holes obtained by means of DRIE etching on the rough back surface of the solar cell.

the same front design parameters) is also plotted for reference and indicated as “REF”.

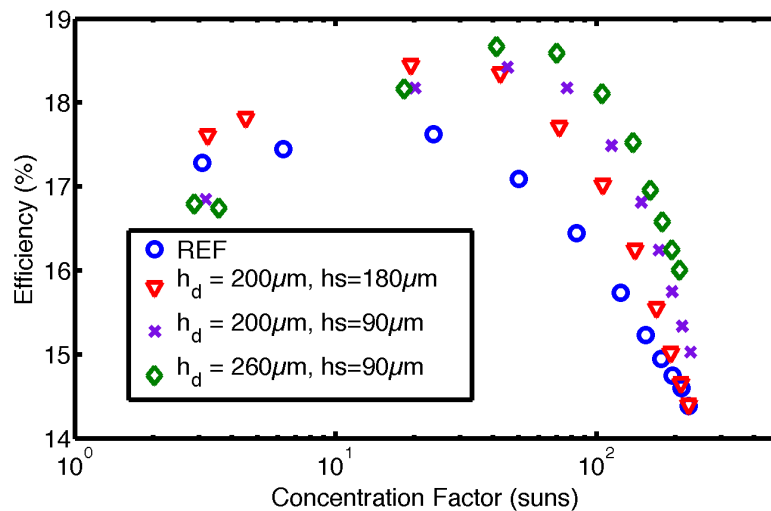


Figure 6.17: DEPC cells with different holes distances and holes depths versus incident intensity.

Under 1-sun illumination, the efficiency of the DEPC cells is comparable with the “REF” cell, but at higher concentration factors (> 20 suns), the DEPC cells show efficiency improvements up to 20% relative with respect to the “REF” cell. The best sample is the one with the lowest hole spacing ($90 \mu\text{m}$) and deepest holes ($260 \mu\text{m}$), as well predicted by numerical simulations (see Section 4.4.4). The improvement of the conversion efficiency is doubtless due to the fact that the DEPC cells do not experience any sub-linear response of the J_{SC} and they have low series resistance also at low concentration factors. This is shown in Figure 6.18, where the total

series resistance (a) and the J_{SC} linearity of the DEPC cells are plotted. It can be noted that the cells with lower hole spacing do not experience any J_{SC} sub-linear response, and they have a low series resistance constant with the concentration factor. On the other hand the cell with longer hole spacing still show a sub-linear J_{SC} response, although this effect is less pronounced with respect to the “REF” cell. This result indicate that the correct design of the back grooved contacts is absolutely necessary to reduce the efficiency losses in the high-resistivity solar cells.

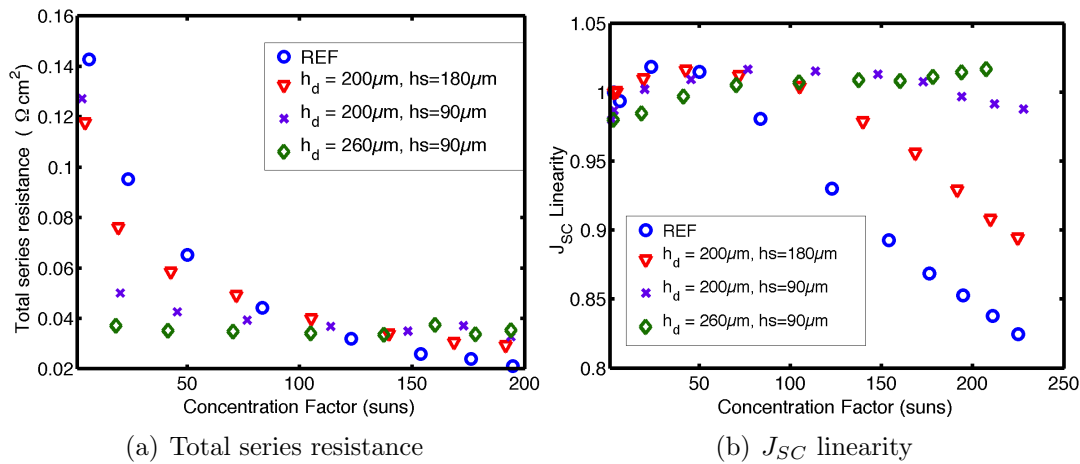


Figure 6.18: Total series resistance (a) and J_{SC} linearity factor as a function of the incident power, measured on DEPC solar cells and on a reference cell (without deep etched contacts).

Although it has been demonstrated that the DEPC concept is able to increase the conversion efficiency of solar cells fabricated on high-resistivity and thick Cz silicon substrate, the conversion efficiency of these cells remains lower than the one of solar cells fabricated on low-resistivity silicon substrate. This is due principally to the fact that also in this case the obtained sheet resistance of the boron doped region is higher than the optimum value (see Section 6.4). The effect of the high sheet resistance on the final cell performance is to reduce the V_{OC} . In fact, also the DEPC cells show V_{OC} lower than 600 mV under 1-sun.

Numerical simulations show that if boron-doped region with sheet resistance lower than 50 Ω /sq is used, the cell performance of the DEPC cells fabricated on high-resistivity Cz silicon, becomes comparable to the one of solar cells fabricated on low-resistivity FZ substrate.

6.6 23% efficient concentrator solar cells

The best front-side contacted solar cell, fabricated in this work, reaches a maximum efficiency of 23% at around 100 suns. The cell was processed on a 280 μm thick 0.5 Ωcm substrate. The front metal grid is 4 μm thick and square geometry. The finger distance of this cell is 180 μm . The optimized grid finger structure guarantees high fill factors, low series resistance and low surface shadowing also at high concentration levels. The front surface of this cell provides selective texturing (it means that only the area between the fingers is textured, while the finger itself lays on a planar sustain). This technique allows to reach very low reflectance and at the same time it preserves the integrity of the metal fingers, also when very narrow fingers (7 μm wide) with high aspect-ratio are used. The textured front side of these cells seems to be nearly perfect leading to very low reflection losses, very high light trapping and to very high short-circuit densities.

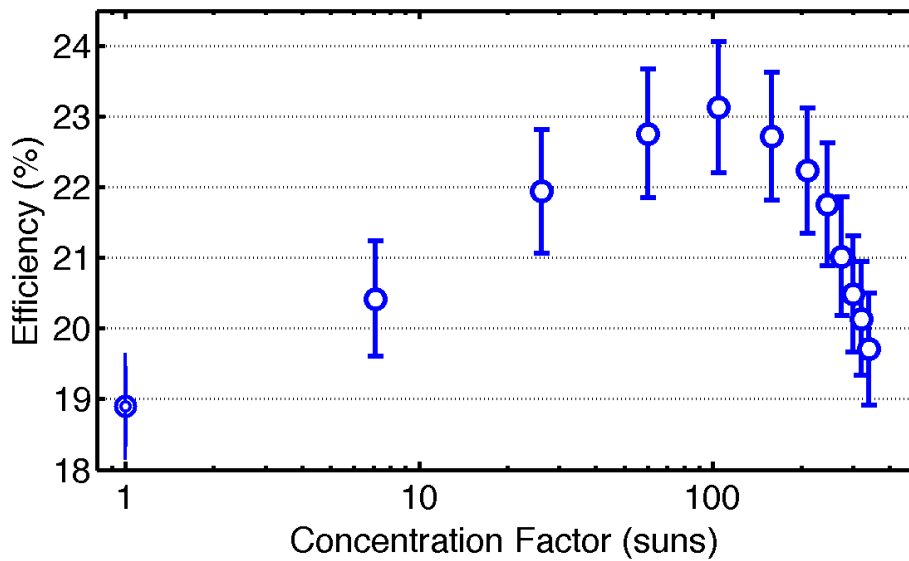


Figure 6.19: The best cell fabricated in this work. Optimized grid finger distances and a textured front side lead to the very high cell performance.

CHAPTER 7

Back-contact vertical junction Si solar cells for concentrating photovoltaics

In this chapter an innovative cell concept, based on back-contacted vertical junctions is introduced. The proposed cell design is conceived to overcome some intrinsic limitations of the conventional front-contacted cells, such as the resistances losses into the base and the front metal-grid shadowing. Numerical simulations and the fabrication process of these devices are briefly described, then the preliminary cell characterization under 1 sun and under concentrated light is reported. Despite the fact that the cells are still at a preliminary stage of development, the first prototypes show conversion efficiency of 22% at 80 suns and higher than 19% up to 200 Suns. The cell performances are compared with the one of a conventional front n-contact solar cell with n^+pp^+ horizontal junction, which is fabricated on the same silicon substrate by means of a similar process. The back-contact vertical-junction cell (or BCVJ cell) shows an increment of 18% in the J_{SC} with respect to the conventional cell. The very promising results suggest that this structure is effective and worthwhile for CPV applications.

7.1 Purpose and scientific relevance

As discussed in the previous chapters, in order to assure high performance under concentrated light, silicon concentrator solar cells should provide both high current generation and low series resistance. As explained in Chapter 4, in conventional bulk crystalline silicon solar cell, the emitter and the metal grid are located on the front surface, while the designed metal grid is the result of a trade-off between low metal coverage to limit optical losses and high coverage to limit resistive losses.

Back-contact solar cells overcome this problem, since the junction and the metal contacts are moved on the rear side of the device [79]. Therefore, there is no metallization pattern on the front surface to shadow the incident photon flux. At the same time, since nearly one half of the back surface can be covered with the metallization pattern of each type, the series resistance of the metal pattern can be very low. On the other hand this structure commonly requires high-quality materials with long bulk lifetime of about 1 ms and very thin substrates or even epitaxially grown layers [21]. However, since silicon is only weakly absorbing the light, the reduction of the cell thickness degrades its optical characteristics.

In this work we propose a new back-contact cell design with vertical junctions. In order to obtain effective vertical junctions, a hole matrix, arranged in two alternating doping type (p and n) is fabricated by means of *deep reactive-ion etching* technique, as explained in Section 3.5.1, and doped by means of solid sources diffusion. Both the contacts and the metallization grid are placed on the cell back surface, therefore the front surface is completely shadow-free. Since the distance between the n - and p -doped holes is only 50 μm , the cell has high collection efficiency in the whole solar spectral range (280 – 1100 nm), also when thick and low-lifetime silicon substrate are used. Moreover, also the resistive losses into the cell substrates are minimized in this structure. In fact, the vertical junctions force the current to flow in a lateral way with respect the cell, in such a way to minimize the resistive path in the base.

7.2 Fabrication process

The fabrication process is based on a FZ p -type mono-crystalline 280 μm thick silicon wafer with 0.5 Ωcm resistivity. The cell area is $4 \times 4 \text{ mm}^2$. The BCJVJ cell scheme is shown in Fig. 7.1, where the details of the back surface (a) and of the cell vertical section are reported.

The front surface is texturized with random pyramids and n -doped to form a

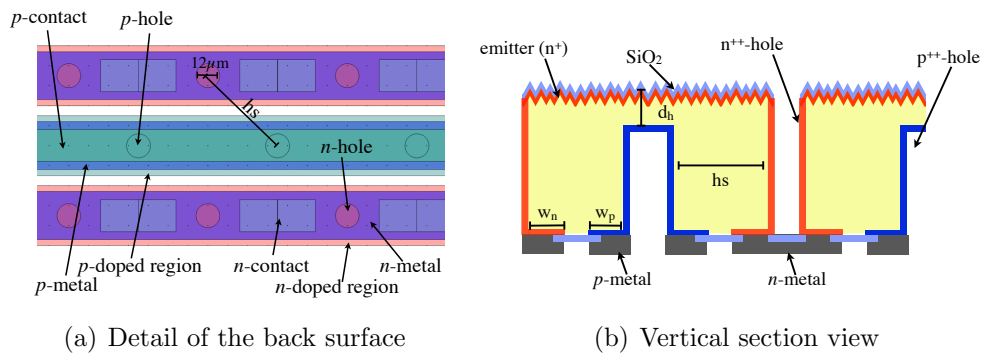


Figure 7.1: Scheme (not in scale) of the back cell surface (a) and the cell vertical section of the BCVJ cell.

shallow emitter region ($80 \Omega/\text{sq}$), while on the back surface there are two separated p^{++} and n^{++} doped regions. A hole matrix is obtained by means of a DRIE process as discussed in Section 3.5.1. The holes (with diameter of $12 \mu\text{m}$) are alternatively doped with phosphorus and boron, following a chessboard scheme. In this way, radial vertical junctions are formed between the p -hole and the neighbors n -holes. The n -holes pass through the cell substrate and wrap the emitter on the front surface to n -doped region on the back surface. The high-doped internal side of the holes act as low resistance current paths to drain the carriers from the front surface, where are generated, to the back surface. The p -doped holes stop $20 \mu\text{m}$ from the cell top surface and are contacted to the back p -doped region. An interdigitated metal grid contacts the p - and n -doped regions on the back to two lateral busbars, which are used to contact the cell to its package. In this prototype the busbars are placed out from the active region of the cell as shown in Fig. 7.2a. Since the area of the whole device is larger than the active area of the cell, a metal shield is placed on the front surface. The shield masks the borders of the device and therefore only the cell active area is illuminated (see Fig. 7.2b).

In order to minimize the parasitic resistance in the base, the spacing between the holes has been kept as low as possible. The minimum hole-spacing achievable with this technology is $50 \mu\text{m}$. However, in order to investigate the role of the distance between the p - and the n -holes, two hole-spacing have been tested: 50 and $80 \mu\text{m}$.

The whole fabrication process consist of 9 lithographic steps. The principal steps of the process are shown in Figure 7.3. At first a thermal oxide was grown to protect front surface in the following steps (1), then the p -holes were defined by lithography and etched by means of DRIE process starting from the rear surface. The latter step, differently by laser-grooving, does not introduce any revealable defects into

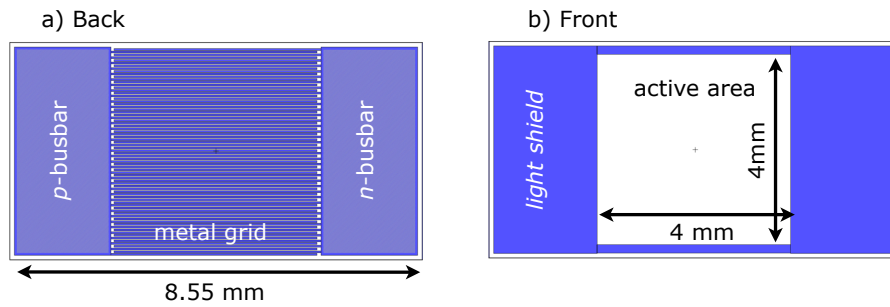


Figure 7.2: Metal layers on the back (a) and on the front (b) surfaces of the the BCVJ cell.

the crystal. This was confirmed performing lifetime measurements. In fact, the effective lifetime was measured (by means of a contactless photoconductance decay system) both before and after the DRIE process, and no significant changes were detected.

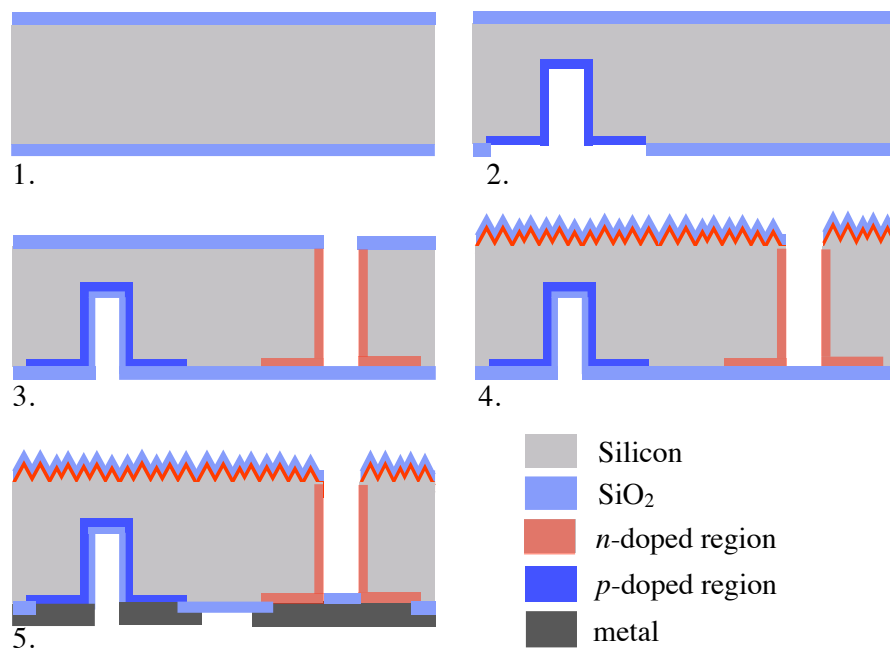


Figure 7.3: Principal steps of the BCVJ cell fabrication process.

After the DRIE process, a region of the back surface around the holes was open in the passivating layer. This region and the holes were exposed to boron doping (2). A second oxidation was performed to seal the backside and at the same the internal sidewall of the p -holes. A second DRIE process was used to fabricate

another matrix of pass-through holes, which were n -doped by means of phosphorus solid source diffusion (3). The second DRIE etching starts from the front surface. Although the n -holes pass-through the whole cell thickness, they are capped on the back surface by a SiO_2 layer. The cover layer preserves the mechanical integrity of the wafer.

At this point the front emitter area was opened, textured to obtain the random pyramids, and lightly n -doped. A following oxidation activates the emitter and at the same time grows a 105 nm thick thermal silicon dioxide layer which passivates the surface and completes the cell anti-reflecting coating (4). Finally, the back contact areas were opened, and the back metal was sputtered and patterned with the last lithography level. Figures 7.4 shows SEM images of the front (a) and back (b) cell surface respectively, at the end of the fabrication process.

7.3 Cell modeling and Simulations

A comprehensive 2D numerical analysis of the device has been performed, over a wide range of design parameters and concentration levels in order to find the optimal cell design, then the optimized cell was fabricated and characterized under concentrated light. Numerical analysis of the BCVJ cell design have been performed by using a 2D drift-diffusion device simulator accounting for the doping and carrier density dependence of mobility, Auger and SRH recombination, as described in Section 4.3.2. Planar (non-textured) surface has been considered in simulations.

A set of simulations were performed over a wide range of design parameters and concentration levels. The investigated design parameters are indicated in Fig. 7.1. In particular, the hole-spacing (hs), the back p - and n -doped regions width (w_p and w_n) and the p -hole distance from the front surface (d_h) are varied in the simulations. Fig. 7.5 shows the efficiency-concentration curves for different values of the design parameters, together with the efficiency of a front-side contacted cell, used as reference. The cell used as reference is the one optimized for 160 suns with square grid, discussed in Section 4.4.1. The considered reference cell is based on the same $0.5 \Omega\text{cm}$ $280 \mu\text{m}$ thick substrate used for the BCVJ cell.

Obviously these two-dimensional simulations can be used only to investigate the expected trends of the conversion efficient with respect to the design parameters. To obtain a more realistic and accurate prediction of the cell performance, a full three-dimensional simulation of the cell must be performed. However, from Fig. 7.5 it can be noted that the best performance under high concentrated light are obtained when the hole-spacing (hs) and the p -hole distance from the front surface

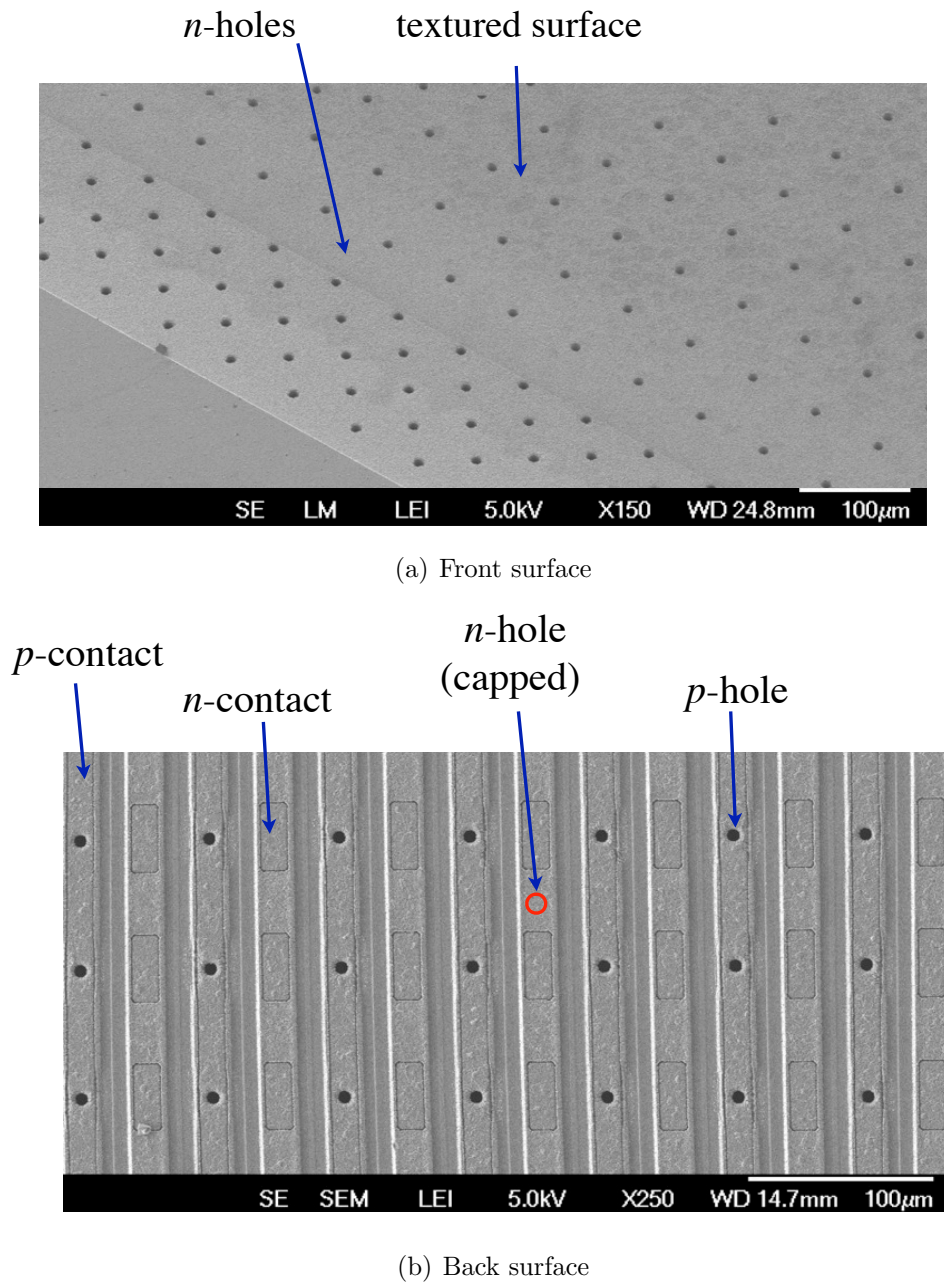


Figure 7.4: SEM images of the front (a) and back (b) cell surface at the end of the fabrication process.

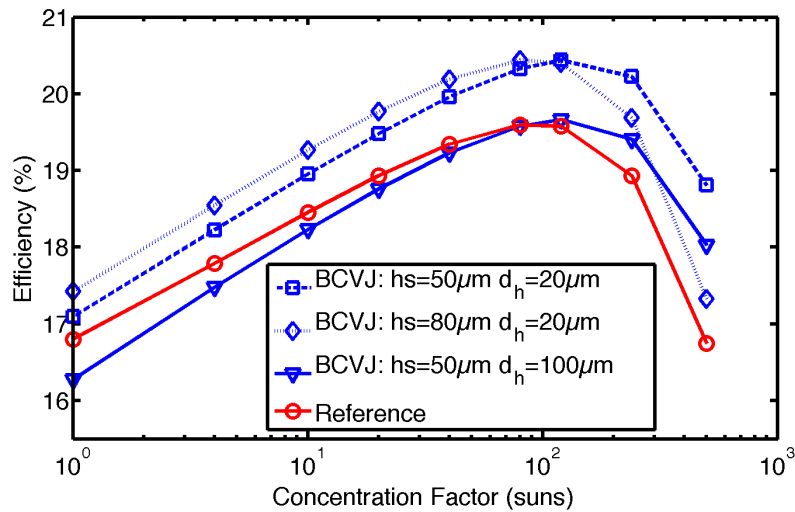


Figure 7.5: Simulated efficiency-concentration curves of the BCVJ cell, obtained with different values of d_h and h_s .

(h_d) are kept as low as possible. The numerical simulations show outstanding performance potential under concentrated light, with efficiencies above 20.5% without considering texturing. The efficiency remains high also under high-concentrated solar light (500 suns and more) and it is higher than the efficiency of the front-side contacted cell “REF” in the whole concentration range from 1 to 500 suns.

This result may be attributed to the lack of any metal shadowing and to the low cell’s series resistance obtained with the vertical junction structure. In order to further investigate this effect, numerical simulations have been used to simulate the current density distribution in the cell. Figure 7.6 shows a contour plot of the total current density in the cell. In this figure is also shown the hole current vector \vec{J}_h near the p -hole top corner. It can be noted that the current flows in a lateral way through the vertical junction. This involves that the resistive path is reduced, because the distance between the n - and p -hole ($50 \mu\text{m}$) is shorter than the cell thickness ($280 \mu\text{m}$).

7.4 Experimental results

Cells with two different hole-spacing have been fabricated: $50 \mu\text{m}$ (BCVJ – hd) and $80 \mu\text{m}$ (BCVJ – ld) respectively. The cells characterization under 1 sun is reported in Tab 7.1. The performances of the BCVJ cells are compared with the one of the conventional front-side contacted cell used as *reference*. Since the BCVJ cells

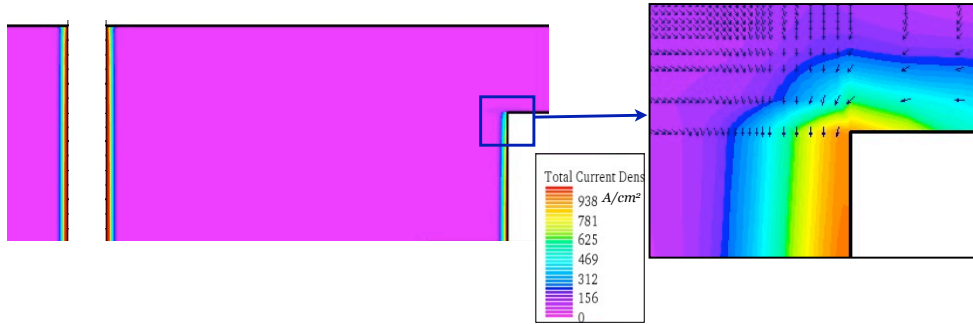


Figure 7.6: Simulated current density in the device working at the maximum power point. In the box on the right, the vector field indicating the hole current J_h is represented. The vectors point from the substrate to the doped p -hole sidewall.

use the solid-source diffusion to perform the boron-doping, also the cell considered for reference is doped by means of the same technique. In particular, the sample characterized in Section 6.3 was used.

Table 7.1: Cells characterization under 1 sun

Measured parameter	BCVJ – hd $hs = 50 \mu\text{m}$	BCVJ – 1d $hs = 80 \mu\text{m}$	REF
J_{OC}	38.9 mA/cm ²	38.6 mA/cm ²	33.0 mA/cm ²
V_{OC}	585 mV	594 mV	632 mV
FF	81.4%	78.2%	82.9%
η	18.4%	17.8%	17.3%

The BCVJ – hd cell has efficiency equal to 18.4% and a very high J_{SC} equal to 38.9 mA, which is 18% higher than the J_{SC} produced by the reference cell. This difference may be attributed to three effects: the absence of any light shadow on the front surface, a better charge collection efficiency due to the vertical junction, and the absence of any LID effect. In Section 6.3 it was demonstrated that the front-side contacted cells, boron-doped by means of solid-source diffusion, suffers from LID effect, which causes a short circuit current decrease.

The BCVJ cells are not affected by LID effect. As discussed in Section 6.3, the LID effect is due to a decrease of the minority carrier lifetime and diffusion length in the base. The lack of the LID effect in the BCVJ cells could be related to the higher collection capability of this structure, which allows to produce high current also when a substrate with low-lifetime is used.

On the other hand, the V_{OC} of the BCVJ cells is 8% lower than the reference one. The V_{OC} drop is probably due to the recombination at the back surface and

at the high doped internal side walls of the holes.

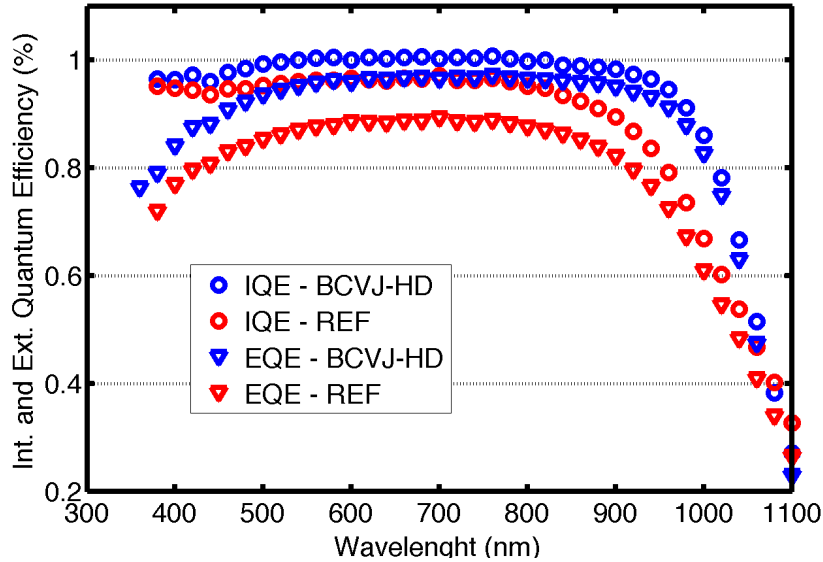


Figure 7.7: The internal (blue symbols) and external (red symbols) quantum efficiency measured on the BCVJ – hd cell (open circles) and on the REF cell (triangles) respectively.

In Figure 7.7 the measured Internal and External Quantum Efficiency (IQE and EQE) of both the BCVJ – hd cell and the reference one are reported. The IQE and EQE of the BCVJ cell are considerably higher than the ones of the REF cell. In particular, the BCVJ internal quantum efficiency is very close to 1 in the whole wavelength range 350 – 1000 nm. The difference in terms of IQE between the BCVJ cell and the reference one is due to the different charge collection efficiency of the two cells. This difference is more pronounced in the red portion of the spectrum, confirming the higher performance of the vertical junction in collecting red and infra-red photons with respect to the conventional horizontal junction. Moreover, the metal-free front surface of the BCJC cells leads to an increase of the EQE in the total investigated spectral range.

The cell efficiency was measured as a function of the concentration factor by using the solar simulator described in Section 5.4. The experimental efficiency of the best BCVJ cell is reported as a function of the concentration factor in Fig. 7.8 and compared with the efficiency of the reference cell. The efficiency of the BCVJ – hd cell reaches the maximum value of 22% at about 80 suns, then it decreases to 19% when the concentration factor becomes greater than 200 suns. Up to 120 suns, the BCVJ cell is more efficient than the reference one, but it rapidly decreases

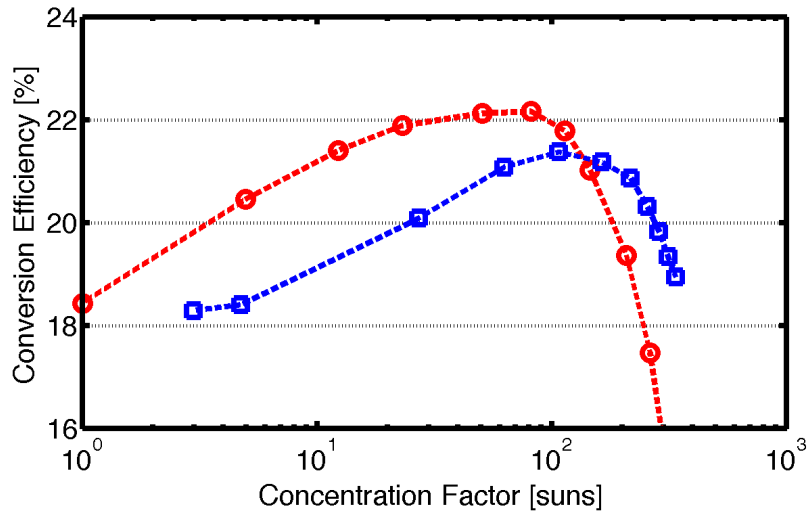


Figure 7.8: The experimental efficiency of the BCVJ – hd cell (red symbols) compared with a reference cell (blue symbols). The reference cell is a conventional front-side contacted cell fabricated by means of a similar process.

in the high concentration range. This behavior differs from the one predicted by the numerical simulations (see Fig. 7.5).

The efficiency drop under high concentrated light may be attributed to the cell series resistance which is higher than the expected one. The cell series resistance was experimentally measured and it resulted $25 \text{ m}\Omega\text{cm}^2$, higher than the one expected from numerical simulations, and higher than the series resistance measured on the reference cell ($19 \text{ m}\Omega\text{cm}^2$).

The reason of the increased series resistance should be further investigated. It may be due to two reasons: some problems in the back metal grid or high-resistivity of the doped sidewalls of the holes. The back metal grid appears to be irregular in the areas where the fingers covers the *p*-holes (see Fig. 7.4b). Such a problem could increase the resistance of the metal grid. The second problem can arise during the doping diffusion, where, due to the high aspect-ratio of the holes, the internal sidewalls are less doped than the surface.

In conclusion we demonstrated that the proposed back-contact vertical junction solar cell is a very promising design for CPV applications. The cell shows high conversion efficiency under concentrated light over 22% also if thick and low-lifetime substrates are used. Although numerical simulations show outstanding performance potential under concentrated light due to the low parasitic series resistance, the real cells show a series resistance higher than the expected one.

In order to further improve the cell conversion efficiency, two parameters should

be further investigated and optimized: the passivation quality of the back surface and of the internal walls of the holes, which lead to V_{OC} losses, and the total series resistance of the cell which comports parasitic losses under concentrated light above 80 suns.

Conclusions

The results presented in this thesis show the successful design and development of innovative and high performing Si concentrator PV cells. The good cell performances obtained and discussed are worthwhile for a deep understanding on the phenomena governing these devices as well as for addressing potential use of the solar cells in future real applications. Besides the major result, i.e. the high efficiency of the cells and the promising “three-dimensional” innovative design, several others have been achieved thanks to the deepening in the SiPV theory and physics. Among them it can be outlined the definition of multi-variable optimization algorithms, with analytical and numerical declinations, which allowed to guide a fast and successful prototype realization as well as an accurate optimization; the improvement in the understanding of the correlation between the concentration factor C and the main PV parameters V_{oc} and J_{sc} ; the interpretation of the unexpected LID effect experienced in the FZ substrates; the interpretation of non-linear response of the short circuit current with respect to the concentration factor and the good agreement between the hypothesis and the experimental results. As a general conclusion, it can be said that this work set the basis for innovative SiPV which can compete with the best worldwide results available today.

Publications

P. Bellutti, A. Collini, L. Ferrario, F. Ficorella, F. Mattedi, G. Paternoster, “*A recent experiment in cSiPV*”. Proceedings of the 3rd International Workshop on CPV - Bremerhaven, Germany (2010).

G. Paternoster, P. Bellutti, L. Ferrario, F. Mattedi, E. Serra, “*Optimization of the Emitter and the Metal-Grid Design for Concentrating Silicon Photovoltaics*”. Proceedings of the 26th European Photovoltaic Solar Energy Conference - Hamburg, Germany (2011).

F. Sgrignuoli, G. Paternoster, A. Marconi, et al. “*Modeling of silicon nanocrystals based down-shifter for enhanced silicon solar cell performance*”. Journal of Applied Physics, 111(3), February (2012).

G. Paternoster, P. Magnone, P. Bellutti, A. Collini, R. De Rose, L. Ferrario, F. Ficorella, C. Fiegna, F. Mattedi, E. Sangiorgi, M. Zanucoli. “*Silicon Concentrator Solar Cells: Fabrication, Characterization and Modeling for Future Improvements*”. Proceedings of the 27th European Photovoltaic Solar Energy Conference and Exhibition - Frankfurt, Germany (2012), pp. 181-184.

G. Paternoster, P. Bellutti, A. Collini, L. Ferrario, F. Ficorella, F. Mattedi. “*Back-contact vertical junction Si solar cells for concentrating photovoltaics*”. Submitted to the 28th European Photovoltaic Solar Energy Conference and Exhibition.

Bibliography

- [1] Richard M Swanson. “The promise of concentrators”. *Progress in Photovoltaics Research and Applications*, 8(1):93–111, 2000.
- [2] Antonio Luque, Gabriel Sala, and Ignacio Luque-Heredia. “Photovoltaic concentration at the onset of its commercial deployment. *Progress in Photovoltaics: Research and Applications*, 14(5):413–428, 2006.
- [3] A. W. Blakers and M. A. Green. “20% efficiency silicon solar cells”. *Applied Physics Letters*, 48(3):215–217, 1986.
- [4] M. A. Green. “Silicon solar cells: evolution, high-efficiency design and efficiency enhancements. *Semicond. Sci. Technol.* 1 8 11993) 1-12 Printed in the UK, 8:1–12, 1993.
- [5] RD Nasby, CM Garner, FW Sexton, JL Rodriguez, BH Rose, and HT Weaver. “High efficiency p⁺⁺nn⁺⁺ silicon concentrator solar cells”. *Solar Cells*, 6(1):49–58, 1982.
- [6] PG Borden, R Walsh, and RD Nasby. “The V-groove silicon solar cell”. In *16th Photovoltaic Specialists Conference*, volume 1, pages 574–577, 1982.
- [7] R.A. Sinton, Y. Kwark, J. Y. Gan, and R.M. Swanson. “27.5-percent silicon concentrator solar cells”. *Electron Device Letters, IEEE*, 7(10):567–569, 1986.
- [8] J. Nelson. “*The Physics of Solar Cells*”. Imperial College Press, London, UK, 2003.

- [9] M.A. Green. “*Solar cells: operating principles, technology, and system applications*”. Prentice-Hall series in solid state physical electronics. Prentice-Hall, 1982.
- [10] ASTM G173 - 03 Standard Tables for Reference Solar Spectral Irradiances: Direct Normal and Hemispherical on 37° Tilted Surface. Technical report, ASTM International, 2012.
- [11] RR King, NH Karam, JH Ermer, N Haddad, P Colter, T Isshiki, H Yoon, HL Cotal, DE Joslin, DD Krut, et al. “Next-generation, high-efficiency III-V multijunction solar cells”. In *Photovoltaic Specialists Conference, 2000. Conference Record of the Twenty-Eighth IEEE*, pages 998–1001. IEEE, 2000.
- [12] Frank Dimroth and Sarah Kurtz. “High-efficiency multijunction solar cells”. *MRS bulletin*, 32(03):230–235, 2007.
- [13] P Faine, Sarah R Kurtz, C Riordan, and JM Olson. “The influence of spectral solar irradiance variations on the performance of selected single-junction and multijunction solar cells”. *Solar cells*, 31(3):259–278, 1991.
- [14] Sze S. “*Physics of Semiconductor Devices, 2nd Edition*”. John Wiley and Sons,, New York, NY, 1981.
- [15] William Shockley and Hans J. Queisser. “Detailed Balance Limit of Efficiency of p-n Junction Solar Cells”. *Journal of Applied Physics*, 32(3):510–519, 1961.
- [16] M. J. Kerr, J. Schmidt, A. Cuevas, and J. H. Bultman. “Surface recombination velocity of phosphorus-diffused silicon solar cell emitters passivated with plasma enhanced chemical vapor deposited silicon nitride and thermal silicon oxide”. *Journal of Applied Physics*, 89(7):3821–3826, 2001.
- [17] R.M. Swanson and R. A. Sinton. “*Advances in solar energy*”. Plenum Publishing Corporation, 1991.
- [18] M. A. Green. “*Silicon solar cells: advanced principles and practice*”. Bridge printery, Sydney, NSW, 1995.
- [19] Pietro P. Altermatt, Jurgen O. Schumacher, Andres Cuevas, Mark J. Kerr, Stefan W. Glunz, Richard R. King, Gernot Heiser, and Andreas Schenk. “Numerical modeling of highly doped Si:P emitters based on Fermi-Dirac statistics and self-consistent material parameters”. *Journal of Applied Physics*, 92(6):3187–3197, sep 2002.

- [20] R.A. Sinton and R.M. Swanson. “Recombination in highly injected silicon”. *Electron Devices, IEEE Transactions on*, 34(6):1380–1389, 1987.
- [21] Andreas Mohr. “*SILICON CONCENTRATOR CELLS IN A TWO-STAGE PHOTOVOLTAIC SYSTEM WITH A CONCENTRATION FACTOR OF 300x*”. PhD thesis, Albert-Ludwigs-Universität Freiburg im Breisgau, 2005.
- [22] Pietro P Altermatt, Ronald A Sinton, and Gernot Heiser. “Improvements in numerical modelling of highly injected crystalline silicon solar cells”. *Solar energy materials and solar cells*, 65(1):149–155, 2001.
- [23] G. Giroult-Matlakowski A. Cuevas, P. A. Basore and C. Dubois. “Surface recombination velocity and energy bandgap narrowing of highly doped n-type silicon”. In *Proceedings of the 13th European Photovoltaic Solar Energy Conference*, pages 337–42, 1995.
- [24] Guido Masetti, Maurizio Severi, and Sandro Solmi. “Modeling of carrier mobility against carrier concentration in arsenic-, phosphorus-, and boron-doped silicon”. *Electron Devices, IEEE Transactions on*, 30(7):764–769, 1983.
- [25] D. E. Kane and R. M. Swanson. “Effect of electron-hole scattering on the current flow in semiconductors”. *Journal of Applied Physics*, 72(11):5294–5304, 1992.
- [26] D.B.M. Klaassen. “A unified mobility model for device simulation” I. Model equations and concentration dependence”. *Solid-State Electronics*, 35(7):953–959, 1992.
- [27] M. A. Green. “Silicon solar cells: evolution, high-efficiency design and efficiency enhancements”. *Semiconductor Science and Technology*, 8(1):1, 1993.
- [28] M.A. Green, Jianhua Zhao, A. Wang, and S.R. Wenham. “Very high efficiency silicon solar cells-science and technology”. *Electron Devices, IEEE Transactions on*, 46(10):1940–1947, 1999.
- [29] P. Bellutti, A. Collini, L. Ferrario, F. Ficorella, F. Mattedi, and G. Paternoster. “A recent experiment in cSiPV”. In *3rd International Workshop on CPV: Optics - Materials - Modules - Bankability - Grids, Bremerhaven, Germany, Online Proceedings*, 2010.

- [30] JH Reiss, RR King, and KW Mitchell. “Characterization of diffusion length degradation in Czochralski silicon solar cells”. *Applied physics letters*, 68(23):3302–3304, 1996.
- [31] NB Mason, TM Bruton, S Gledhill, KC Heasman, O Hartley, C Morilla, and S Roberts. “The selection and performance of monocrystalline silicon substrates for commercially viable 20% efficient lid-free solar cells”. In *Proceedings of the 19th European Photovoltaic Solar Energy Conference*, page 620, 2004.
- [32] A. Cuevas. “The effect of emitter recombination on the effective lifetime of silicon wafers”. *Solar Energy Materials and Solar Cells*, 57(3):277–290, 1999.
- [33] D. E. Kane and R. M. Swanson. “Measurement of the emitter saturation current by a contactless photoconductivity decay method”. In *IEEE Photovoltaic Specialists Conference*, 1985.
- [34] Sinton-consulting-inc., <http://www.sintonconsulting.com>.
- [35] R.A. Sinton, A. Cuevas, and M. Stuckings. “Quasi-steady-state photoconductance, a new method for solar cell material and device characterization. In *Photovoltaic Specialists Conference, 1996., Conference Record of the Twenty Fifth IEEE*, pages 457–460. IEEE, 1996.
- [36] R.R. King, R.A. Sinton, and R.M. Swanson. “Studies of diffused phosphorus emitters: saturation current, surface recombination velocity, and quantum efficiency. *Electron Devices, IEEE Transactions on*, 37(2):365–371, feb 1990.
- [37] Gaelle Giroult-Matlakowski Andres Cuevas, Paul A. Basore and Christiane Dubois. “Surface recombination velocity of highly doped n-type silicon”. *Journal of Applied Physics*, 80(6):3370–3375, 1996.
- [38] D. Iencinella, E. Centurioni, R. Rizzoli, and F. Zignani. “An optimized texturing process for silicon solar cell substrates using TMAH. *Solar Energy Materials and Solar Cells*, 87:725–732, 2005.
- [39] J.T.L. Thong, W.K. Choi, and C.W. Chong. “TMAH etching of silicon and the interaction of etching parameters”. *Sensors and Actuators A: Physical*, 63(3):243–249, 1997.
- [40] Jae Sung You, Donghwan Kim, Joo Youl Huh, Ho Joon Park, James Jungho Pak, and Choon Sik Kang. “Experiments on anisotropic etching of Si in TMAH”. *Solar Energy Materials and Solar Cells*, 66:37–44, 2001.

- [41] P. Papet, O. Nichiporuk, A. Kaminski, Y. Rozier, J. Kraiem, J.-F. Lelievre, A. Chaumartin, A. Fave, and M. Lemiti. “Pyramidal texturing of silicon solar cell with TMAH chemical anisotropic etching”. *Solar Energy Materials and Solar Cells*, 90(15):2319–2328, 2006.
- [42] Michel Puech, Jean-Marc Thevenoud, JM Gruffat, N Launay, N Arnal, and P Godinat. “Fabrication of 3D Packaging TSV using DRIE”. In *Symposium on Design, Test, Integration and Packaging of MEMS*, pages 109–114, 2008.
- [43] Franz Laermer and Andrea Schilp. “Method of anisotropically etching silicon”. Technical report, Patent num. 5501893, 1996.
- [44] W.M. Loh, S.E. Swirhun, T.A. Schreyer, R.M. Swanson, and K.C. Saraswat. “Modeling and measurement of contact resistances”. *Electron Devices, IEEE Transactions on*, 34(3):512–524, 1987.
- [45] Andres Cuevas and David A Russell. “Co-optimisation of the emitter region and the metal grid of silicon solar cells”. *Progress in Photovoltaics: Research and Applications*, 8(6):603–616, 2000.
- [46] A. Cuevas, R. Merchan, J.C. Ramos, and R.R. King. “Updated contour plots for the design of p+ emitters of silicon solar cells”. In *Conference Record of the Twenty Third IEEE Photovoltaic Specialists Conference*, pages 309–314, may 1993.
- [47] Basore P.A. Clugston D.A. “PC1D version 5: 32-bit solar cell modeling on personal computers”. In *Conference Record of the Twenty Sixth IEEE Photovoltaic Specialists Conference*, 1997.
- [48] J. del Alamo, S. Swirhun, and R.M. Swanson. “Simultaneous measurement of hole lifetime, hole mobility and bandgap narrowing in heavily doped n-type silicon”. In *International Electron Devices Meeting*, volume 31, pages 290 – 293, 1985.
- [49] Martin A. Green. “Intrinsic concentration, effective densities of states, and effective mass in silicon”. *Journal of Applied Physics*, 67(6):2944–2954, mar 1990.
- [50] D.B.M. Klaassen, J.W. Slotboom, and H.C. de Graaff. “Unified apparent bandgap narrowing in n- and p-type silicon”. *Solid-State Electronics*, 35(2):125–129, 1992.

- [51] Manuel Cid Sanchez and Nair Stem. “Phosphorus emitter and metal - grid optimization for homogeneous (n+p) and double-diffused (n++n+p) emitter silicon solar cells”. *Materials Research*, 12:57–62, 2009.
- [52] Synopsys Co., Mountainview, CA. “*User’s MAnnual for Sentaurus Device*”, 2008.
- [53] Silvaco co., Japan. “*ATLAS Device Simulation, User’s Manual*”, 2010.
- [54] R. De Rose et al. “2-D Numerical Analysis of the Impact of the Highly-Doped Profile on Selective Emitter Solar Cell Performance”. In *37th IEEE PVSC*, 2011.
- [55] David J Roulston, Narain D Arora, and Savvas G Chamberlain. “Modeling and measurement of minority-carrier lifetime versus doping in diffused layers of n+-p silicon diodes”. *Electron Devices IEEE Transactions on*, 29(2):284–291, 1982.
- [56] J. G. Fossum and D. S. Lee. “Physical Model for the Dependence of Carrier Lifetime on Doping Density in Nondegenerate Silicon”. *Solid-State Electronics*, 25(8):741–747, 1982.
- [57] J. G. Fossum et al. “Carrier Recombination and Lifetime in Highly Doped Silicon”. *Solid-State Electronics*, 26(6):569–576, 1983.
- [58] Andreas Schenk. “Finite-temperature full random-phase approximation model of band gap narrowing for silicon device simulation”. *Journal of Applied Physics*, 84(7):3684–3695, 1998.
- [59] A. R. Moore. “An optimized grid design for a sun-concentrator solar cell”. *RCA Review*, 40, 1979.
- [60] TE Zirkle, DK Schroder, and CE Backus. “The superlinearity of the short-circuit current of low-resistivity-concentration solar cells”. *Electron Devices, IEEE Transactions on*, 36(7):1286–1294, 1989.
- [61] RC Dondero, TE Zirkle, and CE Backus. “Superlinear behavior of short circuit current in silicon n+/p/p+ solar cells. In *IEEE photovoltaic specialists conference. 18*, pages 1754–1755, 1985.
- [62] RW Sanderson, CE Backus, and J Birkeland. “Measurement of concentrator solar cell short-circuit current linearity”. In *16th Photovoltaic Specialists Conference*, volume 1, pages 454–458, 1982.

- [63] A. L. Fahrenbruch and R. H. Bube. “*Foundamentals of Solar Cells*”. Academic Press, New York, 1983.
- [64] J. M. Gee. in “Conference Records, 19th IEEE photovoltaic Specialist Conference. page 1390, New York, 1987.
- [65] Martin A Green, Jianhua Zhao, and David L King. “Sublinear current response in high-efficiency, high-resistivity silicon solar cells: Theory and experiment”. *Applied physics letters*, 52(16):1361–1363, 1988.
- [66] D.L. King and B.R. Hansen. “A sensitivity analysis of the spectral mismatch correction procedure using wavelength-dependent error sources [solar cell testing]”. In *Photovoltaic Specialists Conference, 1991., Conference Record of the Twenty Second IEEE*, volume 1, pages 459–465, oct 1991.
- [67] Pietro P Altermatt, Gernot Heiser, Armin G Aberle, Aihua Wang, Jianhua Zhao, Stephen J Robinson, Stuart Bowden, and Martin A Green. “Spatially resolved analysis and minimization of resistive losses in high-efficiency Si solar cells”. *Progress in Photovoltaics: Research and Applications*, 4(6):399–414, 1998.
- [68] D Pysch, A Mette, and SW Glunz. “A review and comparison of different methods to determine the series resistance of solar cells”. *Solar Energy Materials and Solar Cells*, 91(18):1698–1706, 2007.
- [69] Martin Wolf and Hans Rauschenbach. “Series resistance effects on solar cell measurements”. *Advanced Energy Conversion*, 3(2):455–479, 1963.
- [70] H Fischer and W Pschunder. in Proceedings of the 10th IEEE Photovoltaic Specialists Conference. 1973.
- [71] Jan Schmidt and Karsten Bothe. “Structure and transformation of the metastable boron- and oxygen-related defect center in crystalline silicon”. *Phys. Rev. B*, 69:024107, 2004.
- [72] Stefan W Glunz, S Rein, W Warta, J Knobloch, and W Wettling. “Degradation of carrier lifetime in Cz silicon solar cells”. *Solar energy materials and solar cells*, 65(1):219–229, 2001.
- [73] Jan Schmidt, Armin G Aberle, and Rudolf Hezel. “Investigation of carrier lifetime instabilities in Cz-grown silicon”. In *Conference Record of the 26th IEEE Photovoltaic Specialists Conference*, pages 13–18. IEEE, 1997.

- [74] G Zoth and W Bergholz. “A fast, preparation-free method to detect iron in silicon”. *Journal of Applied Physics*, 67(11):6764–6771, 1990.
- [75] L. J. Geerligs and Daniel Macdonald. “Dynamics of light-induced FeB pair dissociation in crystalline silicon”. *Applied Physics Letters*, 85(22):5227–5229, 2004.
- [76] R. R. King H. Reiss and K. W. Mitchell. Extended abstracts of the 5th workshop on the role of impurities and defects in silicon device processing. page 120, 1995.
- [77] J. Lagowski, P. Edelman, A. M. Kontkiewicz, O. Milic, W. Henley, M. Dexter, L. Jastrzebski, and A. M. Hoff. “Iron detection in the part per quadrillion range in silicon using surface photovoltage and photodissociation of iron-boron pairs”. *Applied Physics Letters*, 63(22):3043–3045, 1993.
- [78] Jan Schmidt and Andres Cuevas. “Electronic properties of light-induced recombination centers in boron-doped Czochralski silicon”. *Journal of Applied Physics*, 86(6):3175–3180, 1999.
- [79] Emmanuel Van Kerschaver and Guy Beaucarne. “Back-contact solar cells: a review”. *Progress in Photovoltaics: Research and Applications*, 14(2):107–123, 2006.